

bradscholars

Investigating mechanical properties of ordinary portland cement. Investigating improvements to the mechanical properties of Ordinary Portland Cement (OPC) bodies by utilizing the phase transformation properties of a ceramic (Zirconia).

Item Type	Thesis
Authors	Almadi, Alaa
Rights	<p>
The University of Bradford theses are licenced under a Creative Commons Licence.</p>
Download date	2026-06-14 01:08:16
Link to Item	http://hdl.handle.net/10454/7315



University of Bradford eThesis

This thesis is hosted in [Bradford Scholars](#) – The University of Bradford Open Access repository. Visit the repository for full metadata or to contact the repository team



© University of Bradford. This work is licenced for reuse under a [Creative Commons Licence](#).

INVESTIGATING MECHANICAL PROPERTIES OF
ORDINARY PORTLAND CEMENT

Investigating improvements to the mechanical properties of
Ordinary Portland Cement (OPC) bodies by utilizing
the phase transformation properties
of a ceramic (Zirconia)

ALAA ALMADI

submitted for the degree
of Doctor of Philosophy

School of Engineering, Design and Technology
University of Bradford

2012

Abstract

The effects of metastable tetragonal zirconia on the properties of Ordinary Portland Cement were observed during which the effect of crystallite size pH on the preparation solution, precursor salt, and the presence of co-precipitates, $\text{Fe}(\text{OH})_3$, SnO_2 and SiO_2 on the crystallization temperature, enthalpy and crystal structure, immediately following the crystallization exothermic burst phenomenon in ZrO_2 were measured. Thermal analysis and x-ray methods were used to determine crystallite sizes and structures immediately following the exothermic burst. Comparisons were made for zirconias prepared from oxychloride, chloride and nitrate solutions. The existence of tetrameric hydroxide-containing ions in oxychloride precursor is used to rationalise low values of crystallization enthalpy.

The position of the crystallization temperature, T_{max} was not dependent on crystallite size alone but also on the pH at which the gel was made, the surface pH after washing, and the presence of diluent oxides. Enthalpy $\propto r^{1/2}$ and $T_{\text{max}} \propto (\text{diluent vol})^{1/3}$ relationships indicate that surface coverage effects dominate a surface nucleated phenomenon. The data established for ZrO_2 systems was used to develop tetragonal- ZrO_2 - SnO_2 powders capable of improving the mechanical properties of Ordinary Portland Cement discs.

The ZrO_2 -OPC discs were prepared by powder mixing, water hydration and uniaxial pressing. Vicat needle tests showed that tetragonal- ZrO_2 increases the initial setting rate. Microscopy indicated that porosity distribution changes near to ZrO_2 particles. Zirconia has also been introduced into OPC discs by vacuum infiltration methods developed for solutions and colloidal suspensions. Comparisons between OPC discs and the OPC-tetragonal ZrO_2 composites have been made on the basis of diametral compression

strength, Young's modulus, hardness and toughness (K_{1c}), as estimated by the cracked indentation method. Bell-shaped curves are found for the way the mechanical properties are changed as a function of Zirconia content.

KEYWORDS: Mechanical properties, Ordinary Portland Cement (OPC), Zirconia, phase transformation properties, Thermal analysis and X-ray, porosity distribution, vacuum infiltration methods, Bell-shaped curves, Young's modulus of OPC composites, crystallite sizes and structures.

Acknowledgement

I would like to first of all thank the almighty God in giving me the ability to complete this work despite the many challenges I encountered during the course of the research. I am heartily thankful to my supervisor, Prof Ian McColm whose encouragements, guidance and support from the conception right through to the end enabled me to develop a thorough understanding of the subject. I am particularly fortunate to have the privilege of sharing some of his immense knowledge and experiences.

I also wish to thank Prof Simon Tait for his assistance, encouragement and support.

Special thanks to my father and mother for their lifelong support and continuous prayers appreciating them tremendously from the bottom of my heart. I would equally wish to express my gratitude and appreciation; too numerous to mention individually, but all those who in one way or another supported the realisation and completion of this work in the School of Engineering, Design and Technology and the University as a whole.

Contents

Abstract	i
Acknowledgement	iii
CHAPTER ONE	1
INTRODUCTION	1
1.1 General Introduction	1
1.2 Aims and scope of this work	2
1.3 Outline of thesis chapters	4
CHAPTER TWO	5
DOCUMENTATION FROM PUBLISHED LITERATURE	5
2.1 Ordinary Portland cement	7
2.1.1 Tricalcium silicate (C_3S)	10
2.1.2 Dicalcium silicate (C_2S)	11
2.1.3 Tricalcium aluminate (C_3A)	13
2.1.4 Tetracalcium aluminoferrite (C_4AF)	14
2.1.5 Minor constituents of OPC	15
2.2 Hydration of OPC	19
2.2.1 Hydration of C_3S	19
2.2.2. Hydration of C_2S	21
2.2.3. Tricalcium aluminate (C_3A) hydration	22
2.2.4. Hydration of Tetracalciumaluminoferrite (C_4AF)	24
2.2.5 Hydration of the composite OPC	25
2.3 Setting of cement	29

2.4 Strength of Portland cement Bodies	31
2.4.1 Factors influencing strength	32
2.4.2 Fracture Testing	46
Material system	51
Test geometry	51
K1c	51
MNm ^{-3/2}	51
Flexural strength.....	51
MPa.....	51
E.....	51
GPa	51
Ref.....	51
2.5 Zirconia (ZrO ₂).....	61
CHAPTER THREE	78
EXPERIMENTAL TECHNIQUES.....	78
3.1 Materials used in this study	78
3.2 Preparation of zirconia powders	79
3.3 Cement disc preparation.....	81
3.3.1 Fabrication of OPC-ZrO ₂ composites.....	82
3.4 Characterisation.....	84
3.4.1 Combined thermogravimetry differential thermal analysis (TG/DTA).....	84
3.4.2 Thermogravimetry alone.....	87

3.4.3 X-ray powder diffraction.....	89
3.4.4. Porosity measurement.....	92
3.5 Mechanical Properties	94
3.5.1 Microhardness measurement	94
3.5.2 Fracture toughness measured by indentation technique	95
3.5.3 Young's modulus measurement by the Knoop hardness method	96
3.5.4 Tensile strength measurement	96
CHAPTER FOUR	98
STUDY OF THE AMORPHOUS TO CRYSTALLINE PHASE	
TRANSITION OF ZIRCONIA.....	98
4.1 Introduction.....	98
4.2 Results.....	103
4.2.1 Zirconia made from solutions containing zirconium cations only	103
4.2.2. Zirconia from solutions containing tin and iron cations	115
4.2.3. Activation Energy of Zirconia Crystallisation as Evaluated	
from DTA Experiments	122
CHAPTER FIVE.....	134
DETERMINATION OF THE PROPERTIES OF THE PORTLAND CEMENT	
PASTE USED IN THIS RESEARH.....	134
5.1 Introduction.....	134
5.2 Development of a Fracture Strength Procedure	136
5.2.1 Flexural Test.....	136
5.2.2 The Indirect tension method: The Brazil test	139

5.2.2.1 Results of the effect of water cement ratio	141
5.2.2.2 Results on the effect of porosity	143
5.2.2.3 The effect of time on measured strength	144
5.2.2.4 Determination of the Weibull modulus of OPC	146
5.3 Determination of Young's Modulus	146
5.3.1. Results from the resonance frequency method	147
5.3.2 Results from Knoop indentation hardness tests	148
5.4 Micro hardness and large-load hardness.....	149
5.4.1 Microhardness.....	149
5.4.2. High Load Hardness.....	152
5.5 Toughness and Hardness-Fracture Studies	154
5.5.1. Notched Beam Method.....	154
5.5.2 Cracked Indentation Method	155
5.6 Thermal analysis and hydration.....	157
5.6.1 Hydration Microbalance Thermogravimetry.....	157
5.6.2. DTA-TG of OPC paste w/c = 0.24 and 28 days set.	158
5.6.3 Time to initial set	159
5.7 Summary results.....	160
CHAPTER SIX.....	161
PROPERTIES AND CHARACTERISATION OF OPC-TETRAGONAL	
ZIRCONIA COMPOSITES	161
6.1 Introduction.....	161
6.2 Dry-mixing of OPC and tetragonal zirconia prior to hydration.....	162
6.2.1. Observation on setting enthalpy, setting rate and porosity	163

6.2.2 The effect of zirconia on strength and Young's modulus	169
6.3 OPC-zirconia gel composites	192
6.4 Composite made by the vacuum infiltration method	194
6.4.1 Dry OPC + ZrO ₂ discs infiltrated by water.....	194
CHAPTER SEVEN	197
Conclusions and Future Work.....	197
7.1 General Discussion.....	197
7.2 Conclusions	224
References.....	228

LIST OF TABLES

Table 2.1:	Cement Nomenclature	9
Table 2.2:	Different presentations of the phases found in OPC	10
Table 2.3:	Some collected mechanical properties data for cements and concrete	51
Table 3.1:	Analysis of the cement used for all this work	78
Table 4.1:	Peak temperature, weight losses, and particles sizes of ZrO ₂ Precipitated from ZrOCl ₂ solution	104
Table 4.2:	Peak temperature, weight losses, and particles sizes of ZrO ₂ Precipitated from Zr(NO ₃) ₄ solution	106
Table 4.3:	Thermal analysis data	108
Table 4.4:	Data on the products arising from fired sol made from acidic zirconium silicate	113
Table 4.5:	Data on preparations made from pH 10.4 solutions	114
Table 4.6:	Effect of Fe ³⁺ concentration on the crystallisation of ZrO ₂ gel made at pH 8.5 from ZrOCl ₂ solution	116
Table 4.7:	DTA results for crystallisation peak maximum temperature obtained at 10 ⁰ C min ⁻¹ heating rate for powders obtained from Zr(NO ₃) ₄ solutions containing 7% Fe(NO ₃) ₃	118
Table 4.8:	Effect of Fe ³⁺ ions on the crystallite size of ZrO ₂	118
Table 4.9:	Effect of Sn ²⁺ concentration on the crystallite size of ZrO ₂	121

Table 4.10:	Thermal analysis and x-ray data for mixed zirconia-tin oxide gels	121
Table 4.11	Crystallisation peak maximum temperature and mass loss data for a heating rate of 100C min^{-1} for gel made from $\text{Zr}(\text{NO}_3)_4$ solution containing 7 mol % SnO_2 at made at different pH values	121
Table 4.12:	Activation Energies for the decomposition-crystallisation process for different samples of zirconia as found using different model equations	126
Table 4.13:	Activation energies for gel crystallisation calculated from the Ozawa equation	130
Table 4.14:	Activation energies calculated for crystallisation of pure ZrO_2 gel using the Matusita equation (4.12)	130
Table 4.15:	Ranges of activation energies using different analyses	132
Table 5.1:	A batch of Six OPC beams tested in 3-point bend	138
Table 5.2:	Relationship between flexural strength of hcp and water to cement ratio	138
Table 5.3:	Brazil Fracture strength of OPC pastes aged for 28 days. Pressed at 3 kN m^{-2} (w/c of 0.23)	139
Table 5.4:	The effect of failure mode and sample ageing time on Brazil strength of nominal w/c 0.25 pastes pressed at 0.3 tonnes (triplicate samples)	140

Table 5.5:	Manufacturer's data for compressive strength of OPC prisms made from material supplied for this research	141
Table 5.6:	w/c effect on Brazil strength at different ageing times (Data: Mean \pm S.D.)	143
Table 5.7:	Beam dimensions, porosity and Young's Modulus of OPC bars w/c of 0.23	147
Table 5.8:	Knoop indentation hardness and values of Young's modulus calculated from them compared to porosity for OPC at w/c = 0.23 (triplicates)	148
Table 5.9:	Vickers Hardness and Fracture Toughness* for 28-day OPC at w/c = 0.23-0.25 using a 4.9N load	151
Table 5.10:	Vickers Hardness of OPC with w/c = 0.25, load 4.9N. Data from uncracked indents	151
Table 5.11:	The effect of load and hydration time on the Vickers hardness of OPC w/c =0.25	152
Table 5.12:	Toughness parameters for OPC beams with	154
Table 5.13:	Rates of water absorption for OPC	158
Table 5.14:	Setting times for OPC at different w/c ratios	160
Table 5.15:	Summary of OPC properties at w/c ratio of 0.25	160
Table 6.1:	X-ray crystallographic data for the product of OPC + tetragonal ZrO ₂ heated to 1150 ⁰ C	165
Table 6.2:	The effect of zirconia content on the initial setting time Of OPC	166

Table 6.3:	The effect of zirconia on the total porosity of OPC	167
Table 6.4:	Rates of water absorption for OPC and OPC + 10wt% ZrO ₂	169
Table 6.5:	Data showing the effect of time and w/c ratio on the strength of OPC and OPC-10wt% ZrO ₂ composites	170
Table 6.6:	The effect of time and Zirconia content on strength for composites: w/c =0.25171	
Table 6.7:	A five sample batch of OPC + 5% ZrO ₂ with w/c ratio of 0.25 after 21 days setting time	172
Table 6.8:	The effect of different amounts of tetragonal zirconia on the strength of OPC discs at a w/c ratio of 0.15 at 28 days setting time	173
Table 6.9:	The effect of zirconia content on the Young's modulus of OPC for samples aged for 28 days and w/c = 0.15	174
Table 6.10:	Macrohardness and toughness of 5 and 10 wt% zirconia - OPC disks, w/c=0.15, tested after 6-12 months hydration	176
Table 6.11:	Improvement in mechanical property of versus OPC alone	190
Table 6.12:	Mechanical properties of OPC-zirconia gel composites made by dry mixing and heating prior to hydration	193

Table 7.1:	Crucean and Rand's Data (117) for Gel Transformations	198
Table 7.2:	Calculated critical flaw size present in OPC-ZrO ₂ composites	212

LIST OF FIGURES

Figure 2.1:	Development of Compressive strength of OPC major constituents with time. (Source: Design and Control of Concrete Mixtures, PCA Engineering Bulletin, 13 th Edition, 1992)	13
Figure 2.2:	Evolution of heat from a cement-water paste	27
Figure 2.3:	Flexural strength plotted against the notch length of MDF cement	39
Figure 2.4:	Schematic figure showing different cracks patterns	42
Figure 3.1:	Apparatus used for solvent evaporation from cement discs	83
Figure 3.2:	(DTA/TG) Block diagram of a typical XRD system	86
Figure 3.3	Curve for correcting line width of Debye-Scherrer lines for instrumental broadening	92
Figure 3.4:	BSE micrograph of the surface of a hydrated OPC disc...	97
Figure 4.1:	Projection on (001) plane of $\{\text{Zr}_4(\text{OH})_8(\text{H}_2\text{O})_{16}\}$ tetramer	102
Figure 4.2:	DTA traces of typical ZrO_2 gels	103
Figure 4.3:	Peak max temp v particle size	107
Figure 4.4:	SEM micrographs of zirconia powders	109
Figure 4.5:	X-ray films for the product from ZrSiO_4	111

Figure 4.6:	SEM micrographs of zirconia	112
Figure 4.7:	Relationship between crystallisation temperature of zirconia and % of (a) Fe_2O_3 and (b) SnO_2 present	117
Figure 5.1:	Flexural strength testing arrangement	136
Figure 5.2:	Relationship between Young's modulus and the porosity of these OPC bars	148
Figure 6.1:	Correlation between measured and estimated E, w/c ratio and zirconia percent	175
Figure 6.2:	(a) BSE micrograph of OPC + 5 wt% tet. ZrO_2 , (b) BSE micrograph of OPC + 10 wt% tet. ZrO_2 , (c) SE micrograph of OPC + 10 wt% tet. ZrO_2	178
Figure 6.3:	Plot showing fracture toughness versus $[\text{ZrO}_2]$	191
Figure 6.4:	SEM micrographs of Dry OPC + 10% ZrO_2 vacuum-filled with H_2O	196

CHAPTER ONE

INTRODUCTION

1.1 General Introduction

This thesis is concerned with investigating the possibilities of making improvements to the mechanical properties of ordinary Portland cement (OPC) bodies by utilizing the phase transformation properties of a modern ceramic, zirconia. The traditional terminology OPC, currently replaced by CEM I Portland cement, refers to cement containing clinker and gypsum. In order to do this the effect of tetragonal zirconia and zirconia gel on the hydraulic behaviour of OPC and ways of introducing them into the cement pastes need to be established and these were the overall objectives of this research project.

Portland cement concrete, despite its limitations, is presently the most widely used manufactured material. This is because it is made from ordinary Portland cement, sand and gravel, all of which have low energy contents, around 5.6, 8, and 0.1 GJ per tonne respectively and are therefore inexpensive. Secondly, it is a hydraulic cement, developing its strength and form on site, from a series of hydration reactions which allow shaping to be done at the early plastic stage. The future of concrete looks even brighter, because for most purposes, it offers suitable engineering properties at low cost, when used in compression, combined with energy-saving and ecological benefits. It is continuing to receive even more intensive, detailed, scientific study ⁽¹⁾ which suggests that substantial improvements in properties

are potentially accessible.

Hydraulic cements such as OPC are interesting, not just because of their familiar use in construction, but because they may form the basis of novel materials for a future in which energy is expensive and undesirable if it increases the carbon dioxide burden in the atmosphere. Hence materials of high energy content are undesirable on two counts and cement and concrete afford increased carbon and financial savings compared to other construction materials. They are made from readily available raw materials e.g. limestone and clay, with little energy being required to convert these into the final ceramic cement phase, for example, 17 GJm⁻³, which compares to 100 GJm⁻³ for porcelain and 30 GJm⁻³ for alumina.

1.2 Aims and scope of this work

The work done for this submission is relevant because cement and concrete are a subset of the materials used by the construction industry.

The aims and scope for this research were formulated as follows:

1. To develop a satisfactory method of producing metastable tetragonal zirconia powders for use in OPC-tetragonal-ZrO₂ composite disc manufacture. The conventional stabilising oxides were not thought to be satisfactory because the tetragonal phase is usually too stable to be transformed to monoclinic by crack-tip stresses likely to be encountered in cement-mortar artefacts.
2. To examine the effect of the presence of OPC phases on the in-situ preparation of tetragonal -ZrO₂.

3. To quantify the effect of zirconia on the setting process of OPC cement.
4. To make quantitative assessments of strength and fracture toughness, hardness and Young's modulus of OPC-tetragonal-ZrO₂ composites.
5. To study the possibility of developing a vacuum infiltration technique to make OPC-tetragonal-ZrO₂ artefacts.

With respect to each of these aims, some success has been achieved, as the following chapters will attempt to show. In particular, thermal and x-ray analysis have revealed important features of the crystallisation process from amorphous ZrO₂ to the crystalline modifications. The process has been shown to be surface nucleated and so the roles of iron and tin oxides in controlling the crystalline modification of zirconia have been explained. It is also suggested in this thesis that the effect suspended silicates in OPC-H₂O gels have on the zirconia is to enhance the retention of tetragonal-ZrO₂ in OPC-zirconia composites.

Considerable strength and toughness improvements have been found here for the OPC-ZrO₂ composites with maximum effect at 5–8 wt% tet-ZrO₂. As the volume of zirconia is increased above 8wt%, the mechanical properties decrease again. Some evidence is gathered to show that this deterioration is due to a zirconia related porosity effect. Vacuum infiltration methods were, unlike earlier work with β -Al₂O₃ ⁽¹¹⁸⁾, not particularly successful because of chemical reactions between OPC and the solutions.

1.3 Outline of thesis chapters

This thesis follows a specific pattern with different components segregated into different chapters such as: Chapter 2 describes the documentation available from published literature, chapter 3 details the experimental techniques used in the current study, chapter 4 on transition phases of zirconia, chapter 5 describing properties of OPC, chapter 6 discussing OPC-tetragonal zirconia and the final chapter 6 listing conclusions and future work.

CHAPTER TWO

DOCUMENTATION FROM PUBLISHED LITERATURE

The UK building materials market is estimated to be worth approximately £82bn in 2002 and contributes about 10% of the UK's GDP, whilst the construction industry employs 2.2 million people at the end of 2009.¹

Cement and concrete are popular because of their ease of use, adequate strength at low cost⁽²⁾. The low cost aspect results in very little cement being exported or imported due to the cost of transport soon overtaking the intrinsic value of the material.

Therefore, cement production markets are nationalistic with nearly all countries having their own cement production facilities⁽³⁾. Although there is scope for exporting cement where very low manufacturing prices make it viable, such as from China to the United States⁽⁴⁾, it is not common practice of exporting the product from low cost economies. To a large extent, this dominates the nature of the research that is done on OPC by concentrating activity on low cost modifications. The work described in this thesis is contrary to this direction because we will be considering the addition of a high cost, high technology additive, that to be successful, will have to make significant improvements to mechanical properties without seriously interfering with its ease of manufacture and application.

¹ Sanchez, F., Sobolev, K., 2010. Nanotechnology in concrete – A review. *Construction and Building Materials* 24, 2060–2071.

The strength of cement products such as OPC arises from hydration during setting and is generally quite low. This is particularly the case for the tensile strength, which is as low as 5 to 10 MPa. Poor microstructure is responsible for this situation⁽²⁾, for example, the presence of large pores⁽⁵⁾, the presence of un-hydrated cement particles and often the presence of entrapped excess water at some sites, have all been identified as failure sources⁽²⁾.

Artefacts made from OPC are in fact highly porous and since porosity allows movement of potentially aggressive species this can affect their durability. However, polymer impregnation, and high-pressure compaction have been used to limit porosity^{(5),(6)}. For example, pressing cement mortar shapes in dies to several hundred MPa can reduce porosity to 2 vol%, raising the bend strength to 60 MPa and compressive strength to 655 MPa⁽⁷⁾. This has moved the attention of the research community on to further considerations of porosity control. A more economical way of reducing cement porosity is to use less water in the mix, i.e., low water to cement ratio (w/c). The reasons for this will be discussed more fully below. This strategy, however, runs the risk of having insufficient water to fully hydrate all the OPC.

There are advanced ceramic materials, such as zirconia, that are also made by hydrolysis methods in order to control the polymorphic form (monoclinic, tetragonal and cubic) and considerable research has been done to see if these polymorphs can be used to improve the mechanical properties a large number of ceramic phases (monoclinic), (tetragonal), (cubic). However there is still little work reported on attempts to fill cement porosity and form a

composite with mechanical property advantages deriving from the zirconia phase. Following a review and some experimental work done with zirconia, the research here is concerned in part with determining the properties of OPC-zirconia composites. Pore removal by non-pressure routes involving zirconia is another method that this thesis seeks to examine.

2.1 Ordinary Portland cement

The most widely used types of cement are the Portland cements, so named because of the similar appearance of set mortars to that of Portland stone. They are hydraulic in that they set and harden by the action of water only. They do not rely on atmospheric action or drying. The major advantages of cement usage are listed below ⁽⁸⁾:

- Low cost
- Flexibility of application: concretes, mortars, cement-grouts, etc.
- Variety of finishes obtainable
- Good compressive strength
- Protection of embedded steel from atmospheric corrosion

Cement is manufactured by grinding the raw materials: limestone, clays, shale, or blast-furnace slag containing alumina. The mixture is then heated, as it moves down a progressively hotter tilted kiln to temperatures above 1400°C. Over a period of six hours, the mixture undergoes a series of complex chemical and physical changes initiated by the heat energy. The heating process is carried out in a rotary kiln, which is more than 150m long

and 3.7m in diameter ⁽⁹⁾. At the high temperatures involved, waste products can be incinerated safely, to cut down the heating costs.

The chemical reactions occurring during the kiln process can simply be described as the conversion of calcium and silicon oxides into cement's principal constituents, calcium silicates. The presence of aluminium ions leads to aluminate and aluminosilicate phases, some of which are disadvantageous. The constituent phases of cement and their relative amounts determine the characteristics of the cement during each period of the hydration reaction, from an initial dormant period, when water is added, through to the setting period and a final period of hardening.

Portland cement is a polyphase, inorganic powder. EN197-1 guidelines define it as "a product obtained by mixing together calcareous or other lime-bearing material with, if required, argillaceous and/or other silica, alumina or iron oxide-bearing materials, burning them at a clinkering temperature and grinding the resulting clinker; a few percent of gypsum is added to the grinding process to regulate the setting time of the cement".

OPC consists mainly of silicate, aluminate and aluminosilicate minerals with distinct crystallographic structures, but the composition is expressed in a time honoured way as oxides: lime (CaO), silica (SiO₂), alumina (Al₂O₃) and iron oxide (Fe₂O₃), even though these are effectively not present but rather the mixture of silicate and aluminate crystalline products.

The combined content of the four principal oxides is about 90% of the cement by weight, and these are referred to as the “major components” of OPC. The remaining 10% consists of crystalline products expressed as the oxides; magnesia (MgO), alkali oxides (Na₂O, K₂O), titania (TiO₂), phosphorus pentoxide (P₂O₅), together with gypsum and some free lime; these combined are referred to as the “minor components”.

Cement science and technology has evolved its own shorthand nomenclature for the silicates, aluminates and oxides present in a mixture, for example, CaO = C, SiO₂ = S and so the silicate CaSiO₃ is expressed as CaO.SiO₂ = CS.

Compounds present in Portland cement in the system CaO-Al₂O₃-SiO₂ or C-A-S are given in Table 2.1.

Table 2.1

Cement Nomenclature ⁽¹⁰⁾

	CaO	SiO ₂	Al ₂ O ₃	Fe ₂ O ₃	K ₂ O	H ₂ O	SO ₃
Symbol	C	S	A	F	K	H	S

As shown in Table 2.2, the principal phases present in OPC have established common names, such as alite, belite, aluminate, and aluminoferrite ⁽¹¹⁾. Portland cement behaves as the sum of these four main constituents. The hydraulic properties of the cement and the resultant mechanical properties therefore depend on these phases. This in turn produces a complex relationship between time and properties as each of the main phases has different kinetics with respect to hydrolysis reactions. It is

worthwhile at this stage to briefly review the main components of OPC.

Table 2.2

Different presentations of the phases found in OPC

Compound	Chemical formula	Equivalent oxide formula	Cement notation	Common name
Tricalcium silicate	Ca_3SiO_5	$3\text{CaO}.\text{SiO}_2$	C_3S	alite
Dicalcium silicate	Ca_2SiO_4	$2\text{CaO}.\text{SiO}_2$	C_2S	belite
Tricalcium aluminate	$\text{Ca}_3\text{Al}_2\text{O}_6$	$3\text{CaO}.\text{Al}_2\text{O}_3$	C_3A	aluminate or celite
Tetracalcium aluminoferrite	$\text{Ca}_4\text{Al}_2\text{Fe}_2\text{O}_{10}$	$4\text{CaO}.\text{Al}_2\text{O}_3.\text{Fe}_2\text{O}_3$	C_4AF	ferrite
Calcium sulphate hydrate	$\text{CaSO}_4.2\text{H}_2\text{O}$	$\text{CaO}.\text{SO}_3.2\text{H}_2\text{O}$	CSH_2	gypsum

2.1.1 Tricalcium silicate (C_3S)

This phase is stable between about 1250 °C and 1800 °C. It melts at approximately 2150 °C. Below the stable temperature it is a peritectoid mixture of C_2S and C. There are seven reported forms of C_3S , three triclinic (T), three monoclinic (M), and one trigonal (R). The monoclinic forms are the ones that usually occur in OPC. These forms have different structures whose bonding is affected as a result of doping^(8, 12). The amounts by volume or by mass percent of C_3S in clinker range between 45 to 65%.

These polymorphs have equilibrium temperatures in the following sequence:

600 °C 920 °C 980 °C 990 °C 1050 °C 1070 °C

T1 → T2 → T3 → M1 → M2 → M3 → R

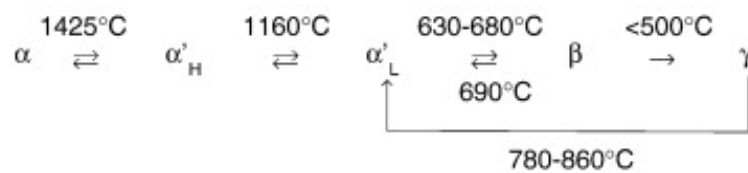
The impure phase of C_3S obtained on cement clinker formation is referred to as alite while Tricalcium silicate refers to the pure phase. Depending on the

impurity ions, alite is usually monoclinic (M1 or M3), but rhombohedral or triclinic modifications do occur. The most common impurity ions are Mg^{2+} , Al^{3+} , Fe^{3+} , Na^+ and K^+ , with none being present in large amounts ⁽¹³⁾. The levels of impurities determine the relative levels of pure and impure phases. Research still continues in to the relationship between the alite polymorph and impurity content, and Maki and Kato ⁽¹¹⁾ have recently identified a new form of alite in a clinker rich in magnesia to which they have ascribed the M3 structure.

2.1.2 Dicalcium silicate (C₂S)

Here again several polymorphs exist with five forms of C₂S having been well characterised⁽¹²⁾. The forms are designated, α , α_H , α_L , β , and γ . With the exception of γ -C₂S, all the forms are stable at high temperature in the pure state. γ -C₂S is stable only in the range 1420–1447 °C changing reversibly on cooling to the α -form. α is stable in the temperature range 800–1447 °C, but on cooling it persists down to 650–670 °C, where it changes reversibly to the β -form⁽¹²⁾. All polymorphs are impure when encountered in cement clinker because of isomorphous replacement and as such are gathered together under the general term belite.

A schematic representation of the range of stability is as follows:-



γ -C₂S is orthorhombic, β -C₂S is monoclinic, α -H and α -L are orthorhombic

and α is trigonal or hexagonal. C_2S takes up a greater proportion of impurity ions such as Al^{3+} , Fe^{3+} , K^+ , Na^+ , Sr^{2+} , Ti^{2+} , V^{3+} and Cr^{3+} into solid solution than does C_3S . This is not surprising in view of its structure, which is best described in terms of its composition Ca_2SiO_4 . As written this has the AB_2O_4 spinel, or in this case reversed spinel, structure and spinels are known to be very effective solid solution formers. However, the presence of the small highly charged Si^{4+} ion leads to such polarisation that the structure is better described as close packed $[SiO_4]^{4-}$ ions with interstitial occupation of the Ca^{2+} ions in this array. The Ca^{2+} would need to occupy the tetrahedral interstices in such an array of silicate ions to give the correct stoichiometry. Isomorphous replacement of Ca^{2+} is then easy and so too is Si^{4+} replacement by Al^{3+} as long as charge compensation ions like K^+ or Na^+ etc. are included in the crystal.

β - C_2S hydrates less vigorously than C_3S , having a heat of hydration of about 250 kJkg^{-1} . The hardened paste gains strength steadily and slowly for weeks and months as demonstrated in Fig 2.1. γ - C_2S is not a cementitious product because it does not in fact react with water but β - C_2S does⁽¹⁴⁾. The belite content of OPC averages about 25wt%, and its density is about 3280 kgm^{-3} .

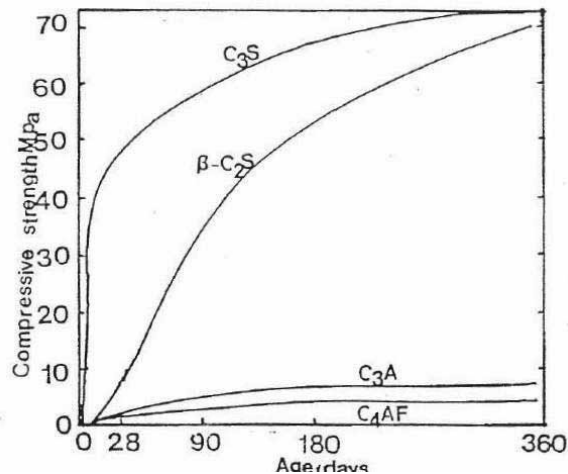


Figure 2.1 Development of Compressive strength of OPC major constituents with time. (Source: Design and Control of Concrete Mixtures, PCA Engineering Bulletin, 13th Edition, 1992)

2.1.3 Tricalcium aluminate (C₃A)

When C₃A reacts with water a “flash-set” occurs where the material hardens without strength development. C₃A tends to release a higher percentage of water during the hardening process, but this does not result in a significant increase in strength. Hydration of C₃S is more important for strength development than hydration of C₃A, thus the relative ratio of C₃A to C₃S is critical. This is accompanied by evolution of a large quantity of heat, in the region of 850 kJ.kg⁻¹. When pure, C₃A shows no polymorphism. However, five polymorphic forms have been identified in cement clinker ⁽¹⁵⁾. These polymorphs are obviously stabilised by impurity ions and have crystal forms described as two cubic (I, II), two orthorhombic (O1, OT) and monoclinic (M). They collectively used to be called celite but this is not often encountered now.

Mondal and Jeffrey⁽¹⁶⁾ determined the crystal structure of allegedly pure C₃A as cubic with $a = 1.526$ nm and space group Pa3. The structure is derived from [AlO₄]⁵⁻ tetrahedra joined by corner oxygen sharing into [Al₆O₁₈]¹⁶⁻ rings. Eight of these discrete ions per unit cell form the basis of the structure to make it quite open. Charge neutralisation is achieved by Ca²⁺ ions in eight fold coordinate sites.

Banda and Glasser⁽¹⁷⁾ have described a new form of C₃A, which they denoted as “proto-C₃A”. This contains Fe³⁺ and Si⁴⁺ ions as solid solution impurity and is metastable. It is obtained through a very rapid cooling of the corresponding mixture of Fe₂O₃, SiO₂ and C₃S.

Recently, Shin and Glasser⁽¹⁸⁾ examined the relationship between Na⁺ and K⁺ ions in C₃A solid solution and the properties of the C₃A phases. The presence of these ions increases the solubility of the non-cubic forms.

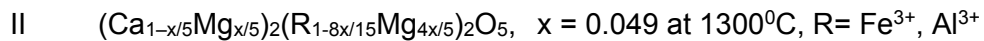
C₃A forms solid solutions with many oxides, such as Na₂O⁽¹⁹⁾, which may be present in OPC clinker. The celite content in OPC ranges from 5 to 10 wt%, with an average around 8 wt%. Its density is 3770 kgm⁻³. On reacting with water it develops little strength.

2.1.4 Tetracalcium aluminoferrite (C₄AF)

The aluminoferrite phase is a solid solution of composition C₂(A_xF_{1-x})₂O₅, where x is variously reported⁽²⁰⁾, but appears to have a maximum value about 0.7. This means that the ferrite phase is part of the C₂A-C₂F solid

solution series. C_4AF is stable at ambient conditions. It has an orthorhombic symmetry with $a = 0.56$ nm, $b = 1.477$ nm and $c = 0.543$ nm in space group $Pcmn^{(21)}$. Its structure is viewed as evolving from the end-member components. It contains layers of FeO_6 octahedra alternating with layers of corner sharing FeO_4 tetrahedral. Opportunities for isomorphous replacement are great within this structure and ions, such as Mg^{2+} , Si^{4+} , Ti^{2+} , Mn^{3+} and Cr^{3+} have been found in the tetracalcium aluminoferrite found in OPC, depending upon whether the Ca^{2+} interstitial ions or the Fe^{3+} network ions are substituted. These impure phases are present in cement clinker and are collectively known as ferrite.

Hahn *et al.* ⁽²²⁾ have proposed two types of solid solution, for example, when Mg^{2+} substitutes for Fe^{3+} or Ca^{2+} there are the series:



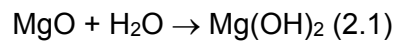
C_4AF reacts rapidly with water, and setting occurs within minutes. The heat evolution on hydration is approximately 420 kJkg^{-1} . Because of the rapid setting, strength values became variable. In Portland cement the ferrite phase varies in composition from C_3AF to C_6AF_2 with the median value being fairly close to C_4AF .

2.1.5 Minor constituents of OPC

(i) Magnesia (MgO)

Magnesium oxide in Portland cement is derived from magnesium carbonate

present in the original raw materials used in the manufacture of OPC clinker. At the clinkering temperature of about 1450°C, MgCO₃ becomes dead burnt to the mineral periclase, which hydrates slowly in water at ambient temperature⁽²³⁾:



Detectable quantities of Mg(OH)₂ only occur several days after the addition of water. The hydration of periclase involves a volume increase that may cause unsoundness. This depends on crystal size, because the smaller crystals tend to hydrate more rapidly without generating excessive internal stress. However, very fine MgO crystals, because of their basic nature, do react quite quickly with CO₂ from the air (alkali-silica reaction), thus introducing an alternative problem sometimes as the product softens and exfoliates^(24, 25).

A higher MgO content may be tolerated in cement made by rapid cooling of clinker because the size of the crystals depends on the cooling rate. Because of the CO₂ problem, for commercial purposes, the magnesia content is limited to 4 wt% in accordance with standard BS12.

In an attempt to shed more light on the role of MgO in cement, Mujumber and Rehis⁽²⁶⁾ investigated the mechanism of stabilisation of high magnesia cement by reactive silica under autoclave conditions. They found that MgO reacts very slowly with SiO₂.

Kasselouris *et al.* ⁽²⁷⁾ have also studied the hydration of cement containing MgO. Their results show that a limiting volume increase is achieved in an OPC paste at the age of eight years from the slow hydration process of MgO.

(ii) Alkali Oxides (Na₂O, K₂O)

Alkali oxide contents of OPC vary from 0.5 to 1.3 wt%. They are introduced into the cement from the raw materials. Invariably they are linked to sulphur trioxide, SO₃, content, since they appear as solid solutions of sodium potassium sulphate, K₂SO₄-Na₂SO₄. These sulphates are important when mortars and concretes are made because the fine forms of silica sand combine with these salts. This reaction results in the formation of alkali silica gel, which is accompanied by volume expansion, such that expansive forces may cause cracking and deterioration of the concrete or mortar. This may be avoided by using low alkali cement, i.e., the content of Na₂O should not exceed 0.6%. It has often been thought ⁽²⁸⁾ that the alkali content plays a considerable part in determining the reaction mechanism and hence the rate with which the calcium silicate phases react with water. Cement commonly has a higher content of potash than soda, and in British cements, the molar ratio K₂O:Na₂O varies from two to five ⁽²⁹⁾.

(iii) Titanium oxide (TiO₂)

The TiO₂ content in OPC varies from 0.1 to 0.4 wt.% being introduced into cement through the clay or the shale used in its manufacture. Most commonly it comes from the shale used to lower the clinkering temperature.⁽³⁰⁾

(iv) Phosphorus pentoxide (P_2O_5).

The P_2O_5 content in most Portland cement does not exceed 0.2 wt.% and it is usually introduced into the cement through the limestone. Its role in the complex interaction in hydrating cement is twofold. First, it decomposes C_3S in favour of a C_2S solid solution containing the P_2O_5 plus some lime, CaO . Thus the presence of P_2O_5 slows the cement setting and hardening because it breaks down some C_3S to C_2S . Secondly, large amounts of P_2O_5 may cause unsoundness because too much free lime would be formed which leads to a too rapid hydration and unsatisfactory microstructure.

(v) Gypsum ($CaSO_4 \cdot 2H_2O$)

Gypsum is added during the grinding of the clinker in order to regulate the setting time of the cement (See Section 2.3). Its content must be limited because an excess may cause cracking and deterioration in the mortar. This adverse effect is due to the formation of ettringite ($3C_3A \cdot 3C \cdot 3S \cdot 3H$) resulting from reaction between C_3A and gypsum. The formation of ettringite involves a volume increase. Because of its comparatively low density, 1730 kgm^{-3} , compared to an average of about 2500 kgm^{-3} for the other hydration products, this volume increase is particularly marked. Gypsum is not added to OPC for initial set regulation alone but also its presence has a longer-term effect as a grinding aid because of its low hardness values. It plays an important role in accelerating alite hydration, which of course affects the rate of strength development and volume stability ⁽³¹⁾. A major parameter influencing optimum gypsum content in cement is the fineness of the powder. This will be enlarged upon when the hydration reactions are discussed more

fully in section 2.3.

(vi) Free lime (CaO)

Free lime is present in most OPC as a mixture of CaO and Ca(OH)₂. If the amount of free lime is too high, it enhances gypsum dehydration by its considerable hygroscopicity, and also has the effect of delaying the rehydration of hemihydrate

CaSO₄.1/2H₂O. About 1.5 wt % or less of free lime is generally considered the optimum quantity in cement.

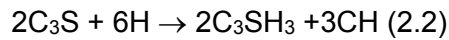
2.2 Hydration of OPC

In order to understand more clearly the potential chemistry and the final microstructure developed after hydration of OPC, it is necessary to consider the hydration mechanisms of the separate components of cement clinker.

2.2.1 Hydration of C₃S

C₃S is the most important component of Portland cement because it controls normal setting and is responsible for the early strength development of the cement body. As C₃S comes in contact with water, a vigorous reaction starts which results in the protonolysis of oxygen and silicate ions on the surface of tricalcium silicate. The majority of the hydration reaction has taken place within 28 days and is to a large degree effectively complete after about one year⁽³²⁾.

The reaction may be approximately represented by the following equation:



The products are calcium silicate hydrate, $\text{C}_3\text{S}_2\text{H}_3$ (also depicted as C-S-H to represent the variability in the composition of the different elements), and calcium hydroxide. The growth of C-S-H follows a diffuse pattern where the density of the packing in the phase of C-S-H is directly proportional to the extent of hydration. These are the main binders of hardened Portland cement paste and are the principal contributors to early strength development in the period up to 7 days. The resulting hydrate is poorly crystalline with a microstructure that produces a porous solid⁽³³⁾. The concept of dividing the C_3S hydration reaction into several stages has been accepted.

Reference (34) sets out the following stages⁽³⁴⁾:

- 1 An initial very fast exothermic reaction where the rate limiting step is associated with modified mechanisms of boundary nucleation as well as growth.
- 2 The induction period, lasting several hours, during which only small quantities of heat are evolved.
- 3 A period of renewed exothermic reaction where increasing quantities of heat are given out. Reaction kinetics are known to be affected by the level and type of mixing: hand versus high shear.
- 4 A period of reaction at a decreasing rate after about 12 hours.
- 5 A slow continuous reaction with the rate only gradually

decreasing after about one day.

The duration and rate of the above stages of hydration can be affected by temperature, zeta potential of early hydration products, water to cement ratio, surface area, and admixtures ⁽³⁵⁾⁽³⁶⁾. Numerous studies of this important reaction have been published, but as references (37) and (38), show, many reports appear to be contradictory. More recent work, carried out in controlled environments, and studied usually with the aid of an electron microscope, is beginning to show that much of the contradiction in the literature appears to arise from the presence of additives, either accidental or deliberate, to the sample.

For example, Singh *et al.* ⁽³⁹⁾ confirmed that melment (a type of superplasticizer) retards the hydration of alite, which is of course mainly C₃S. Another example is from Lorprayoon *et al.* ⁽⁴⁰⁾ who pointed out that salicylic acid has little effect on C₃S hydration which still needed more than 30 days for completion.

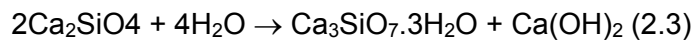
Mechanical effects also appear to be important ⁽³⁷⁾ because complete hydration of C₃S can be obtained in one or two days by grinding with an excess of water in a small ball mill ⁽⁴¹⁾.

2.2.2. Hydration of C₂S

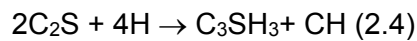
Despite the extensive polymorphism already described for C₂S, the β-form is the main silicate component in Portland cement involved in the hydration

process^(42, 43, 44). The phase hydrates much more slowly than C₃S does, but eventually forms a similar product described as (C-S-H) again denoting the variable stoichiometry.

The hydration is represented by the equation ⁽⁴⁵⁾:



or, in cement notation:



It can be seen that the hydration products are the same as those formed for C₃S, but one third less calcium hydroxide is formed when C₃S is hydrated. This has certain advantages for strength development, because calcium hydroxide contributes less to strength than C-S-H, and the greater the proportion of C-S-H to calcium hydroxide, the better the strength becomes⁽⁴³⁾.

It is more difficult to study the hydration reaction of β-C₂S by heat evolution methods because of the lower heat of reaction. On contact with water non-uniform etching of compressed discs is observed and grain boundaries are revealed as rapid precipitation of C-S-H occurs within 15 seconds ⁽⁴²⁾.

2.2.3. Tricalcium aluminate (C₃A) hydration

C₃A hydrates very rapidly as a pure phase in the presence of excess water to form the hexagonal hydrates C₂AH₈ and C₄AH₁₃. Both these have a plate-like

crystalline habit and are metastable, transforming over a period of time into a less soluble and more stable hydrate of composition C_3AH_6 , which belongs to the cubic crystal system. When C_3AH_6 is formed directly at room temperature in pastes with low water to solid ratio, the chemical equation can be expressed as follows:



If the temperature of reaction is raised, the cubic hydrate appears sooner and direct reaction to the cubic form occurs more rapidly above 40°C. When lime is present, especially in the absence of gypsum, C_4AH_{13} is formed.



It is reaction (2.6) that causes what is colloquially called “flash-set” in Portland cement.

C_3A hydrates differently in the presence of gypsum because of a reaction between C_3A and gypsum that result in ettringite ($3CaO \cdot Al_2O_3 \cdot 3CaSO_4 \cdot 31H_2O$). This continues to form until there is insufficient sulphate ion in the solution.

On mixing the cement with water, alkali ions readily pass into the solution and influence the early hydration reaction of cement components, particularly C_3A . Spierings *et al.*⁽⁴⁶⁾ have shown that at low concentrations of Na_2O the very early heat evolution in C_3A hydration decreases with increasing Na_2O concentration, whereas at high concentration, the heat evolution increases.

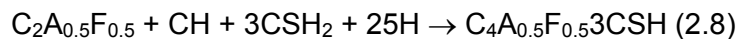
Holten and Stein ⁽⁴⁷⁾ studied the effect of finely divided quartz on C₃A hydration in the presence of gypsum and showed that SiO₂ also significantly accelerates the rate of C₃A hydration.

2.2.4. Hydration of Tetracalciumaluminoferrite (C₄AF)

This phase reacts with water at a slower rate than C₃A, but since it contributes little to the strength of Portland cement paste, this is not a particularly significant fact. However, it can influence the effect that the excess lime has on other components since, in the absence of gypsum, C₄AF reacts with lime and water to form an iron (III) substituted hydrate, C₄A_xFe_yH₁₃. The equation for the reaction is:

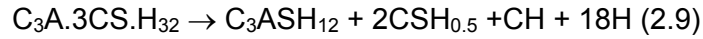


The iron substituted product is stable at ambient temperature and is responsible for removing some of the free lime content. However, in the presence of gypsum, an iron (III) substituted ettringite is formed according to equation (2.8) ⁽⁴⁸⁾:



Because the hydration of C₃A proceeds faster initially than C₄AF, and because OPC contains gypsum, the majority of the ettringite formed during early hydration originates from the reaction given as equation (2.8) ^(49, 50, 51). Ettringite has been reported to be stable up to about 110⁰C ⁽⁵²⁾ but decomposition around 55⁰C has been reported⁽¹⁾.

When it decomposes the monosulphate and hemihydrate are formed according to equation (2.9):



2.2.5 Hydration of the composite OPC

From the preceding paragraphs, we see that hydration of Portland cement will be a sequence of overlapping chemical reactions involving most clinker components, calcium sulphate and water, leading to continuous cement paste stiffening and hardening.

Immediately upon contact of the cement with water, an exchange of ionic species begins between the solids and water phase because of the relatively high solubility of some of the clinker components. This leads to a rapid increase in concentration of some ions in the solution with respect to the component ions of C_3A , calcium sulphate and alkali⁽⁴⁹⁾. The hydration of the cement may involve either, a “through-solution” mechanism, in which the reactants continue to precipitate out or by direct topochemical reaction in which the reaction takes place directly at the surface of the solid without the cement constituents going into solution. In the total hydration of OPC both mechanisms are probably involved because it seems that the first mechanism predominates in the early stages of hydration whereas the second operates during the later stages.

The overall reaction between cement components and water is exothermic and OPC and its constituent compounds still hydrate at $-5^{\circ}C$, but the

hydration reactions are immeasurably slow at -10°C ⁽⁵⁰⁾. Increasing the temperature increases the rate of the reactions, but essentially the hydration products of OPC in these conditions do not differ from those formed at ambient temperature. However, as the setting temperature is raised, there are differences in morphology and overall microstructure that do lead to changed mechanical properties ⁽⁵⁵⁾.

Whilst the overall reactions are those described above, it has been possible recently to study the process in more detail using SEM and Differential Scanning Calorimetry. These techniques have shown that hydration occurs in a number of distinct stages ⁽³⁴⁾ ⁽⁵³⁾.

(a) Stage 1

There is an initial hydrolysis of C_3S , and saturation of the water with respect to calcium hydroxide is quickly achieved from free lime and some impurities. The initial reaction is more controlled by the dissolution rates of CaSO_4 and clinker phases while the later phases of the reaction is more dependent on the crystal growth and nucleation rates and also on the rate of diffusion of water and dissolved ions. At this stage Al^{3+} is also leached from cement grains. The aluminium cations have an inhibiting effect on the dissolution of silicate anions from the solid phase particles. The dissolution and leaching process of Ca^{2+} and Al^{3+} lead to a thin surface layer around each cement powder grain that has a gel-like morphology and links all the particles together.

(b) Stage 2

This is called the dormant period because the reaction becomes very slow during this time. The slowing of the hydrolysis leads to the achievement of super-saturation in the solution phase. This period, in which there is gradual strength development, is shown in Fig 2.2. During this stage Ca^{2+} continue to dissolve from the cement grains, and those released from the solid have to move into a solution of increasing chemical potential through the silicon-rich material of the gel layer. The gel layer is itself separated from the solution by a membrane enriched in Ca^{2+} ions that are required for charge compensation of the gel.

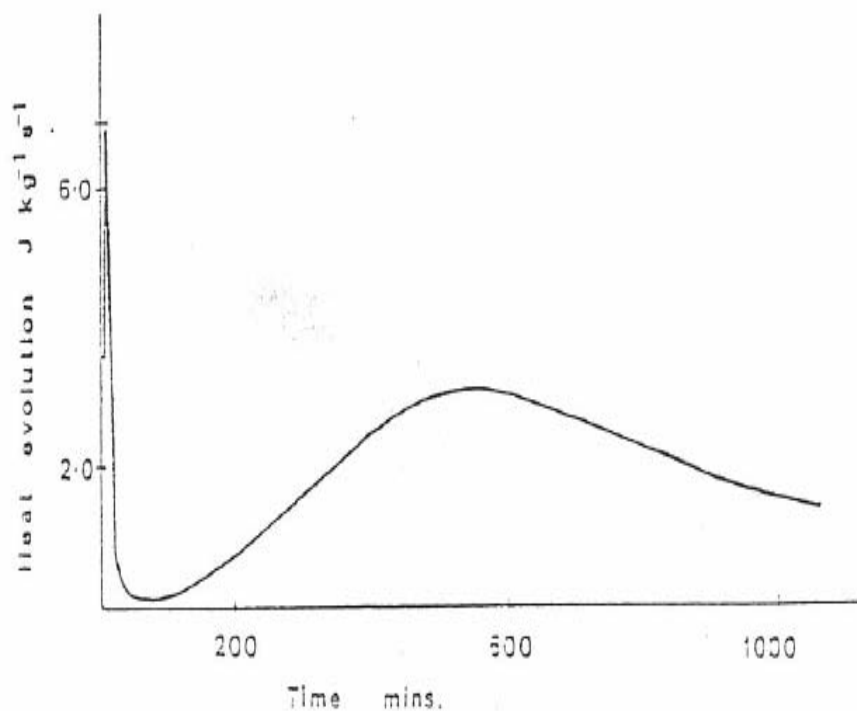


Figure 2.2 Evolution of heat from a cement-water paste ⁽³⁶⁾

In this period the rate of heat evolution drops to a very low value as it is controlled by solid-state diffusion determined by small chemical potential differences.

Lorprayoon and Rossington ⁽⁴²⁾ have shown that the greatest effect of organic retarders is at this stage because they lengthen the time of stage two. This results in an increase in the level of Ca(OH)_2 super-saturation before crystallisation of hydrates begins in stage three.

(c) Stage 3

This stage is associated with a drop in Ca^{2+} concentration in solution that causes the hydration reaction to proceed rapidly again as the chemical potential difference for Ca^{2+} increases. Precipitation of Ca(OH)_2 occurs near the surface of the gel-membrane layers causing localised heating and a resultant stress in the membrane. This combination of events produces fibrous growth at the membrane surface.

X-ray and electron diffraction data show that the crystals growing at this stage are ettringite. This process continues with steady heat evolution until the membrane has been destroyed and after which C-S-H forms rapidly as interwoven sheets from the surface of OPC powder particles. This microstructure gives strength to cement bodies. Elucidation of the mechanisms of these three stages is complicated by the numerous studies that have placed differing importance on the several physical factors that can be varied ⁽³⁵⁾ ⁽³⁸⁾.

These physical variants are as follows:

- Cement composition
- Powder fineness
- Water to cement ratio
- Temperature
- Presence of admixtures
- Relative humidity of the paste surroundings

However, at the microscopic level, from the study of individual, “pure”, cement phases, and from in-situ electron microscopic studies, it is generally agreed now that the process follows the three stages outlined above.

2.3 Setting of cement

Arising from the crystal structure of the cement phases and from the hydration mechanisms and product morphology, the phenomenon of cement setting emerges. To quantify, define and measure such a process for a complex mixture requires some simplified and comparative work. Within this context the setting time is a somewhat arbitrary property but is defined as the time that elapses after mixing the cement with water before the paste will resist penetration by an agreed stress. Initial mixing of cement powder with water produces a plastic workable paste and for some time the characteristics of the paste remain unchanged. This period corresponds to the “dormant period”.

In due course, the paste begins to stiffen to such a degree that whilst it is still soft, it becomes unworkable. The time to achieve this is known as the “initial setting time”. The paste continues to stiffen until it reaches a rigid solid stage; this is known as the “final setting time”. BS12 and ASTM 150 specify a minimum of 45 minutes as the initial setting time for most commercial Portland cements. In contrast, for final setting time, BS12 specifies a maximum of 10 hours whilst 8 hours is specified in ASTM 150.

The initial and final setting times are determined, almost universally; see for example, BS12, ASTM 191 and DIN 1164, using the apparatus known as the “Vicat needle”. This apparatus measures the resistance of a paste to the penetration of a needle with a 1mm^2 cross section under total normal load of 2.94 N. The needle is released at the surface of the hydrating paste at intervals until it penetrates only to a depth of 5 ± 0.5 mm from the bottom of the specimen mould, which is until it penetrates a depth of 5mm beneath its surface. Final setting time is determined by using a similar needle with a concentric ring of $5 \times 10^{-3}\text{m}$ diameter attached to the needle.

The final set is said to be attained when only the needle makes an impression on the surface. Using these semi-quantitative procedures, many workers have made observations on the effect of additives, for example Birchall and Thomas⁽⁴⁹⁾ established that sugars are good retarders of cement setting, and the best of those tried is sucrose.

Diamond *et al.* ⁽⁵⁶⁾ used the technique and reported that the setting time for low porosity pastes was substantially affected by water to cement ratio. Initial setting times have been observed to lengthen when the ambient relative humidity was higher than normal. Singh *et al.* ⁽⁵⁷⁾ showed that lactic acid reduced both the final and initial setting time of cement.

Papers and reports such as these above rely heavily on comparative results within the constraints of their materials, apparatus and techniques, but undoubtedly lead to useable technical findings.

In order to study the effect of zirconia and zirconia gel on OPC in this research, it was necessary to construct and use a form of Vicat needle.

2.4 Strength of Portland cement Bodies

Strength may be defined as a measure of the resistance to failure and collapse under external load. Increases in strength are brought about by the hardening of the cement paste, which, as section 1.3 shows, is caused by the formation of the C-S-H gel. The gel fills the space between the cement grains, bridges between them and gradually fills the pores, so the strength is closely related to the capillary porosity of the paste, which in turn is related to gel porosity.

Idron ⁽⁵⁸⁾ pointed out that ultimately, the strength of the hydrated cement must be due to the following:

- 1 Interatomic forces within the individual particles of hydration products

- 2 Atomic forces which bind the individual hydrates to each other and to grains of still unhydrated cement, i.e., grain boundary forces
- 3 The size, morphology, inter-growth and agglomeration of the hydration products
- 4 The microstructure that develops, that is, the geometrical arrangement and density distribution of the hydration products

Thus, there are many variables that may be strength controlling in any test performed to measure the strength of cement artefacts, with a consequent large variability of test results. This situation is not wholly overcome by adopting standard procedures and designing only self-comparative investigations as adopted in this research. Furthermore, one has to be very careful in considering other data as there are several forms of strength tests that are encountered in studies involving cement, mortar and concrete.

2.4.1 Factors influencing strength

The variability of cement product strength values arises mainly from the complex nature of the hydration processes. Over the years, the following factors have been found to be important.

2.4.1.1 Chemical and mineralogical composition of the clinker

The effect of composition and heat treatment of the clinker on the mechanical properties has recently been reviewed ⁽⁵⁹⁾. It has been confirmed that strength depends directly on the content of the calcium silicates. Increasing values of strength, all other factors remaining constant, are

associated with bigger contents of calcium silicates. Changes made to the composition that affect the proportions and form of the calcium silicate phases, directly affects the product strength. For example, a decrease of compressive strength was observed for cements prepared by adding 3 wt % ZnO to OPC because the ZnO altered the C₂S and C₃A amounts via a solid state reaction ⁽⁶⁰⁾.

2.4.1.2 Water to cement ratio (W/C) ⁽⁶¹⁾

Strength is practically dependent upon the degree of hydration of the cement as well as the water to cement ratio. However, there is no simple correlation between these two factors. When concrete is fully compacted, so that some consistency in microstructure is achieved, its strength is found to be inversely proportional to the water to cement ratio. This relationship, established by Abrams as long ago as 1919, is expressed as Eqn (2.10):

$$\sigma_c = A/B^{w/c} \quad (2.10)$$

Where w/c is water to cement ratio and A and B are empirical constants.

The importance of the water to cement ratio is emphasised because it determines to a large extent the porosity of the hardened cement paste at any stage of hydration. This fact is shown by the empirically determined equation (2.11):

$$p = (w/c)/(v_c + (w/c)) \quad (2.11)$$

In this equation, p is the porosity, v_c is the specific volume, and w/c is water to cement ratio. Thus, w/c affects the volume of voids in hydraulic cements

through the capillary porosity.

These two equations indicate the complexity of the problem because equation (2.10) indicates a linear decrease in strength, but equation (2.11) has porosity linked in an optimum fashion to w/c. This would not matter except that porosity is always a strength-degrading factor.

Jambor⁽⁶¹⁾ has shown that low porosity and the high specific binding capacity of hydration products leads to high strength bodies.

2.4.1.3 Porosity

The w/c ratio affects porosity and hence strength by the removal of water and its incomplete replacement by hydration products, but obviously, not all pores come from the removal of H₂O and replacement of its volume by hydration products. As might be expected, some of the porosity arises from poor green-state packing of the dry OPC powder, and as a result, porosity is always a major component of the microstructure of hydrated cement paste. As far as strength is concerned, the porosity of the hardened cement paste is the dominant factor. Watson⁽⁶²⁾ found that the compressive strength varies linearly with porosity for a range of values from 10 to 15% porosity, and many other semi-empirical relationships between strength and porosity have been reported, as Sereda *et al.*⁽⁶³⁾ point out.

Some examples of the reported equations are

$$\text{Schiller }^{(64)}: \quad \sigma = q \ln[P_{cr}/p] \quad (2.12)$$

$$\text{Roy and Gouda }^{(65)}: \quad \sigma = \sigma_o e^{-bp} \quad (2.13)$$

$$\text{Roy and Gouda }^{(65)}: \quad \sigma = 1/k \ln[p_o/p] \quad (2.14)$$

In these equations b , q and k are constants, σ_o is the strength of the material at zero porosity, P_{cr} is the critical value of porosity at zero strength, and p_o is the porosity at zero strength.

Feldman and Beaudoin ⁽⁶⁶⁾ have shown, via the Ryskewitch equation, that whilst porosity is a major factor controlling strength, it should also be related to other factors, such as density and the degree of crystallinity of hydration products, in order to predict more completely the compressive strength of hydrated cement systems. Bejza ⁽⁶⁷⁾ showed that strength is considerably influenced not just by total porosity but by the stages at which the porosity is introduced. For example, the lower the initial porosity, the higher is the strength at all ages.

Bajza work proposes a linear relationship between the compressive strength and the post curing porosity. His equation is:

$$\sigma = 3795 - 148.4p \quad (2.15),$$

Where σ is the compressive strength and p is the porosity, 3795 is an empirical constant.

Equation (2.15) applies to fully set pastes, and it must be emphasised that relationships found to apply earlier in the setting process are not linear.

Beaudoin ⁽⁶⁸⁾ pointed out that the increased flexural strength of mica-flake reinforced cement paste in the early stages is related to a function of the volume fraction of mica-flakes and porosity combined. Finally, to emphasise the complications, Poon *et al.*⁽⁶⁹⁾ pointed out that by introducing latex into OPC, the flexural strength is reduced despite lowering the total porosity by the process ⁽⁷⁰⁾.

Thus the overall relationship between strength and porosity is far from simple and is far from being solved.

More recently, Birchall *et al.* ⁽⁷¹⁾ have made a major contribution by focusing attention on pore size distribution and showing that cement compositions could display the same volume of porosity whilst having greatly varying strengths. Birchall then showed that the poor tensile properties of cement pastes arise from the presence of macroscopic pores. Macroscopic pores are defined as those with a diameter > 10µm. The elimination of such defects by the use of polymeric rheology modifiers and the application of shear forces during curing gives un-reinforced cement paste a flexural strength up to 150 MPa. Birchall demonstrated this technology by producing a cement spring. Mindess⁽⁷²⁾, from his studies on autoclaved lime-silica mixtures, suggested that the greater the proportion of smaller pores for a given total porosity, the stronger the material, which is in agreement with Birchall's findings. For cement paste, Zaitsev⁽⁷³⁾ showed that the smaller the average

pore size, the higher the compressive strength at a given porosity, and also he found that on increasing the maximum pore size at a constant mean pore size, the strength decreased substantially. This again supports Birchall's hypothesis and justifies the control method he used.

The way that macro-sized pores can dominate the behaviour led Birchall *et al.* ⁽⁷⁴⁾ and Kendall ⁽⁷⁵⁾, to consider the well-established Griffith relationship, eqn (2.16), for strength of brittle materials. The strength of a brittle material with Young's modulus, E, and fracture energy, γ , depends on the length, c of a crack-like pore according to Griffith's relationship:

$$\sigma = (E \gamma / \pi c)^{1/2} \quad (2.16)$$

For hardened cement paste, Birchall *et al.* showed that the Griffith equation did describe the flexural strength of notched beams, but only for notches exceeding the maximum natural flaw size, which was around 10^{-3} m in the material as commonly prepared.

Kendal *et al.* ⁽⁷⁵⁾ developed the theory to include the main influence on strength as being the presence of macro-defects that can initiate fracture in these materials. They have shown that the relation between Young's modulus and porosity is:

$$E = E_0(1-p)^3 \quad (2.17)$$

While for fracture energy, the relationship with porosity is:

$$\gamma = \gamma_0 \exp(-kp) \quad (2.18)$$

In the last two equations, E_0 is Young's modulus at zero porosity; γ_0 is the fracture energy at zero porosity; p is the porosity; and k is a constant. By calculating the energy, U , associated with a crack length $2c$, and using the equilibrium condition:

$$du/dc = 0$$

They showed that the criterion for crack extension in terms of porosity was:

$$\sigma = \{[E_0\gamma_0(1-p)^3\exp(-kp)]^{1/2} / \pi c\}^{1/2} \quad (2.19)$$

This equation suggests that strength is a function of two independent variables, namely volume of porosity, and length of a crack-like pore. They found that the un-notched bend strength rose to 66 MPa, but on reducing the volume porosity of MDF (Macro-Defect-Free) cement to less than 1%, the un-notched strength was near to 150 MPa as shown in Fig (2.3). Thus, whether the total pore volume only model or the Kendall two-regime model is considered, it is obvious that some attempt to control porosity, even in a simple way, should be tried when seeking strength improvements.

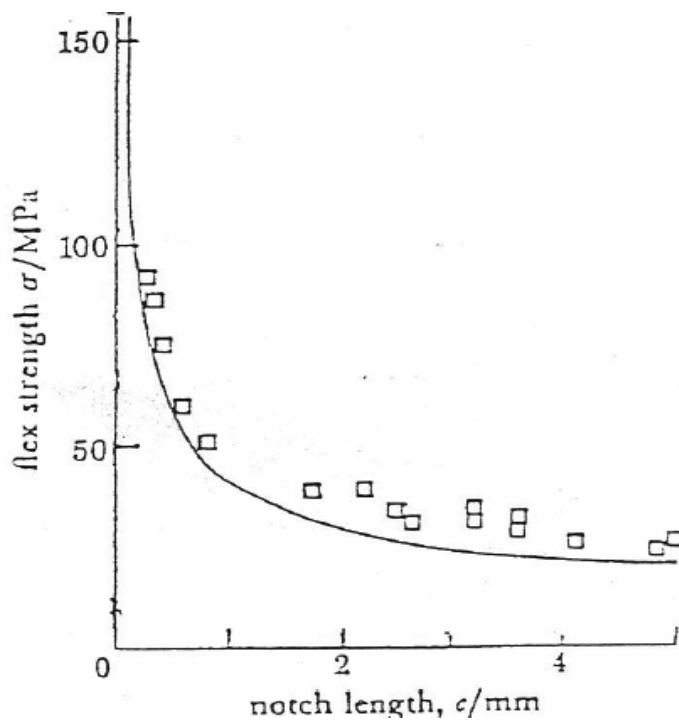


Figure 2.3 Flexural strength plotted against the notch length of MDF cement.

There is another approach to the relationship between strength and microstructure, based not on total porosity as discussed so far, but on fracture mechanics ⁽⁷⁶⁻⁹¹⁾. As mentioned above, cement is traditionally regarded as a brittle material that is very weak in tension that may be modelled as a multi-phase material in which pores, and unhydrated cement grains are dispersed in cement hydrates (C-S-H). In this composite the following observed feature point towards applying a fracture mechanics approach:

1. Fracture generally occurs in a brittle mode.
2. The strength of hydrated cement paste increases with increased rates of loading.

3. The tensile strength of cement is approximately 1/10 of the compressive strength and this is quite close to the value of 1/8 predicted by Griffith for a brittle material.

Davidge ⁽⁹²⁾ pointed out that the application of fracture mechanics to cement is more complex than for conventional sintered ceramics because of the various stages of strength development via the hydration reactions ⁽⁹³⁻¹³²⁾.

An early study of the application of fracture mechanics to cementitious materials was conducted by Kaplan ⁽¹³³⁾. His experiments involved bend tests on single edged notched beams of mortar and concrete, from which, G_C , critical strain energy release rate, that is the amount of energy required to create a crack of one unit area, was calculated. This, and other features, led to the conclusion that the Griffith concept of a critical strain energy release rate being a condition for rapid crack propagation and consequent fracture is applicable to these materials. Later, Berger *et al.* ⁽¹³⁴⁾ showed that at early times in the setting process there is some evidence that cracks propagate preferentially through the high porosity C-S-H phase. Shah and Chandra ⁽¹³⁵⁾ noted that the presence of water plays an important role in determining fracture behaviour, where under sustained load, the time to failure decreases, as the relative humidity at which the specimens were equilibrated, increases.

However, despite uncertainty as to which phase the crack propagates, as several examples show, the stress-strain curve for hydrated cement is

essentially linear until about 90-95% of its ultimate strength, Fig 2.4. The linear feature is common for dense well-formed conventional ceramics and glass, and might not be expected from such a complex material as hydrated OPC, with its many phases, some of which have a plastic nature, and with residual water as well as high porosity. Mindess ⁽¹³⁶⁾ ascribed the behaviour to the presence of good bonding between unhydrated cement grains and the C-S-H phase. The last few per cent of the stress-strain curve is non-linear, such a degree of non-elastic behaviour has variously been related to the rapidly growing micro crack density at the centres of stress concentration.

All these features, and much of the earlier work, indicate that the application of fracture mechanics might be a useful approach. Before this is pursued further it is worthwhile stating some of the basic work in linear elastic fracture mechanics in order to define the parameters of interest.

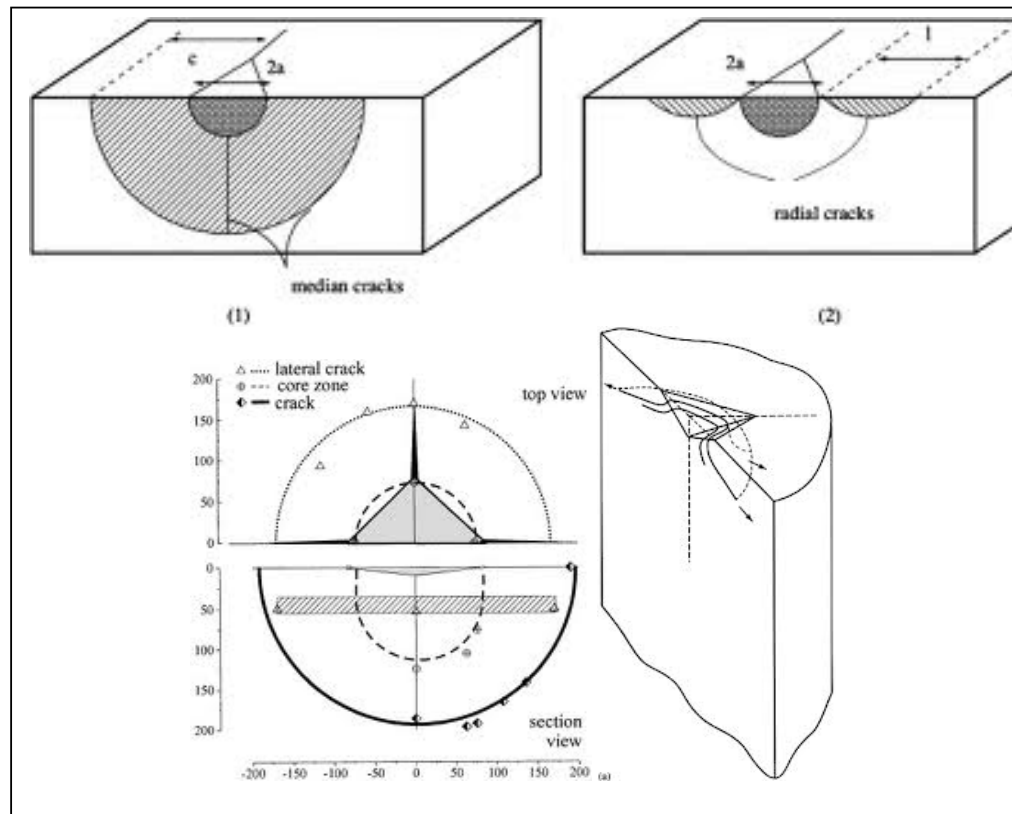


Figure 2.4: Schematic figure showing different cracks patterns¹⁷¹

2.4.1.3.1. Basic features of linear elastic fracture mechanics

The roots of fracture mechanics lie behind the works of Griffith ⁽⁷⁶⁾, who studied glass, a brittle material, and who postulated that the materials containing inert defects, which serve to concentrate the stress in highly localised regions, will fail when the theoretical fracture strength is exceeded locally at such defects. From this assumption, a criterion for failure, or for crack-extension, could be derived by considering the difference between the elastic strain energy that would be released if the cracks were extended and the energy required to creating new fracture surface.

Griffith considered an elliptical crack of length $2c$. The decrease in the elastic strain energy, U , when such a crack is formed in a plate of unit thickness was shown to be:

$$U = \pi c^2 \sigma^2 / E \quad (2.20)$$

In eqn 2.20, σ is the uniform applied tensile stress, E is Young's modulus and $2c =$ crack length.

Griffith suggested that the crack grows rapidly and causes fracture when the rate of strain energy release was equal to the surface energy created by the crack:

$$W = 4 c \gamma \quad (2.21)$$

Here γ is the specific surface energy and W is the strain energy release rate. He argued that instability would occur where a small increment of crack extension, dc , gave $du > dW$. This is the condition that the crack may extend, which from eqns (2.20) and (2.21) is:

$$d/dc (U-W) = d/dc [(\sigma^2 \pi^2 / E) - 4 c \gamma] = 0$$

This gives the strain energy release rate as $\sigma^2 \pi c / E = 2\gamma$, which leads to the well-known Griffith relationship for plane stress:

$$\sigma_C = (2E \gamma / \pi c)^{1/2} \quad (2.22)$$

and for plane strain:

$$\sigma_C = (2E \gamma / \pi c (1-\nu^2))^{1/2} \quad (2.23)$$

where ν is Poisson's ratio.

Neville ⁽¹³⁷⁾ made the first application of the Griffith theory to concrete and suggested that the effect of specimen size on the strength of concrete could be related to the random distribution of Griffith flaws.

Glücklich ⁽¹³⁸⁾ also applied Griffith theory to concrete and showed that the critical strain energy release rate, G_c , was much greater than twice the experimentally determined surface energy of concrete, 2γ . He suggested from this that the fracture of concrete was not limited to the growth of a single crack but rather to a zone of micro-cracking developed near the propagating crack tip. Davidge⁽¹⁰⁹⁾ demonstrated this zone concept in his analysis of the non-linear region. Glücklich ⁽¹³⁸⁾ also showed that high strength areas in the concrete, such as aggregate particles, could act so as to increase the energy demand for crack propagation, forcing the crack to go through a stronger region which requires more energy, or to go around it, so increasing the crack path, which also needs more energy.

Birchall *et al.* ⁽⁷¹⁾ pointed out that since their measured values of the fracture energy of hydrated OPC of about 19 Jm^{-2} was typical of strong brittle ceramics; the relatively low fracture strength of cement must be due to serious flaws in the structure. Birchall and co-workers measured the flexural strength of cement paste and related the values, through the Griffith equation, to the size of the largest natural flaws in the materials. The flaws appeared to be large, in the mm range, which they called macro-defects. They then, as already described, prepared special cements to eliminate the

large macro-defects via shearing mechanisms. Such cements were called macro defect free, MDF. These required much higher flexural stress to cause fracture.

Such samples had to be made by using viscosity modifiers, such as cellulose polymers, which induces a type of plasticity in the cement paste for a limited time. Whilst the plastic nature lasted the material could be put through a mechanical shearing process between rollers to remove its macro-sized pores. Thus, Alford *et al.* ⁽¹³⁹⁾ concluded that the higher strength of the MDF cement could be attributed to a simple reduction in inherent flaw size.

2.4.1.4 Temperature

The chemical reactions of cement hydration speed up when the curing temperature is raised, and this affects beneficially the early strength of cement. However, a higher temperature during placing and setting, although it increases the very early strength, may adversely affect the strength from about 7 days ⁽⁷⁹⁾.

Klieger ⁽⁸⁰⁾ has reported that there is an optimum temperature during the early life of cement that will lead to the highest strength at any subsequent age. Dodson ⁽⁸¹⁾ has confirmed the influence of temperature at the time of placing on strength. This detrimental temperature effect is of considerable importance, and as a result, Butt *et al.* ⁽⁸²⁾ have considered each of the constituents of a cement paste individually. Their conclusions were that the greatest cause of the detrimental temperature effect was the thermal

expansion of water and air which produces internal stresses during the soft plastic stage, which in turn increases the porosity of the paste. Increased porosity and internal stress may cause cracks to appear, the presence of which greatly reduces the flexural strength, via Equation (2.19), presumably without producing a correspondingly significant reduction in compressive strength.

2.4.2 Fracture Testing

The process of fracture and cracking has been studied extensively in literature.⁽¹⁴⁰⁻¹⁷⁰⁾ The principles and the application of indentation fracture have been reviewed by McColm in his book *Ceramic Hardness* ⁽¹⁷¹⁾. Relationships between the fracture toughness parameter, K_{1C} , and the measurable variables in a test, are derived from modelling the indentation process, combined with experimental observation. Thus, there is a range of equations that can be used. The common approach is based on the model of the sharp point of the indenter producing a nearly spherical plastic deformation zone constrained by the bulk of the sample, which behaves elastically. A deformation-induced flaw develops at the median vent, as the load increases. Stable growth of this occurs during the load application. On unloading residual stresses drive the median vent to the surface as a half-penny radial crack.

Lateral vent cracks also begin to develop during the process of unloading. From experiments on transparent, brittle crystals, when indentation diamonds, like the Vickers diamond, are overloaded as far as hardness

determination are concerned, a regular sequence of cracks is seen to develop.

(i) Median cracks

The median crack has a penny-like appearance, and is formed beneath the surface when the indenter is overloaded. Since the maximum stress occurs directly below the apex of the indenter, this is why it is usually found in the elastic peripheral zone below the heavily deformed region directly below the indentation diamond.

(ii) Radial cracks

These arise as a result of the tensile stresses that are developed as the indenter is withdrawn from the sample. These stresses translate the median to the half-penny radial crack. Radial cracks can be used as well defined strength controlling “flaws” in ceramic failure testing in three-point and four-point bend, thus allowing the determination of fracture toughness parameters with high accuracy. The characteristic fracture pattern for a Vickers indentation where the radial cracks are orientated normal to the specimen surface and have a half-penny configuration. It is these traces that make the indentation method possible with non-transparent specimens.

(iii) Lateral cracks

These cracks are formed on unloading at the boundary between the elastic, non-permanently deformed material close to the indenter. They extend from near the base of the deformation zone into a sub-surface saucer-like

configuration. The lateral cracks can produce surface traces if a critical load is exceeded and are responsible for surface spalling in erosion tests. These cracks nucleate just prior to complete unloading of the indenter. Nucleation is followed by an initial unstable propagation to a stopped stage beyond the immediate indentation plastic zone. On unloading the indenter, the laterals continue to propagate stably, and the final crack length is always greater than the indentation diagonal.

(iv) *Palmqvist*

These cracks are shallow radial surface cracks lying within planes containing the axis of the indenter extending out from the corner of an indentation. They are frequently subsumed into the radial half-penny trace of the medians.

2.4.2.1 Indentation hardness-fracture toughness equations

Evans and Charles ⁽¹⁵⁴⁾ were amongst the first to show that fracture at a microhardness indentation in a brittle material could be interpreted in such a way as to yield the fracture toughness of the material. They introduced the first semi-empirical relationship for determining K_{1C} by combining results from the double torsion technique to measure K_{1C} and parameters from the hardness method using a Vickers diamond pyramid indenter. A subsequent dimensional analysis of indentation fracture showed that the indentation crack length c , could be related to the impression diameter, a , through the function:

$$K_{IC}/H_v a^{1/2} = F_1(c/a)F_2(v.\mu.R_y/a) \quad (2.24)$$

In eqn 2.24, K_C is the fracture toughness, H_V is the Vickers hardness, θ is the constraint factor (often taken as 3), ν is Poisson's ratio, μ the coefficient of friction between the indenter and the material, R_y is the plastic zone radius and F_1 , and F_2 are empirically determined functions of the variables in the brackets.

The Evan's experiments revealed that the F_2 function could be replaced by two bulk mechanical properties and so used more easily.

This relationship was shown to arise from a model of a penny-shaped crack wedged by a force P at its centre and its application, which, together with some semi-empirical analysis of data from a wide variety of ceramic systems showed F_2 to have a form:

$$F_2 = (H_V)^{0.4}/E\theta \quad (2.25)$$

The final outcome of the analysis was the relatively simple eqn (2.26) as the first way to determine fracture toughness from cracked indentations.

$$K_C = 0.0732(E/H)^{0.4}H_V a^{1/2}(c/a)^{-3/2} \quad (2.26)$$

However, because Young's modulus is not always available while the other variables come from the hardness determination, Evans sought to simplify the procedure further and through a zero order model reduced equation (1.26) to the simpler format of equation (2.27).

$$K_C = 0.16 H_V a^{1/2}(c/a)^{-3/2} \quad (2.27)$$

Equation (2.27) comes from a zero order model but is able to deliver practical values of fracture toughness to +/- 30%. Equation (2.26) produces toughness parameters well within these limits when values for E are available.

Second and higher order models have been developed to yield more precise and relevant equations, and these are discussed and described in the text Ceramic Hardness by McColm⁽¹⁷²⁾.

Equations (2.26) and (2.27) are possible equations that might be used to determine the K_{1c} parameter of hydrated OPC discs and the more specific ones in ref⁽¹⁵⁸⁾ may be considered if necessary. Beaudoin⁽¹⁶⁰⁾ earlier showed that there is a relation between fracture behaviour of high alumina cement systems, morphology of the hydration products, and the microhardness values of the discs, which means it may be possible to estimate the value of the fracture toughness from microhardness measurements.

Any results obtained in this research would need to be compared to the K_{1c} values obtained from more conventional techniques and summarised in Table 2.3. Even compared to ceramic values, those reported for OPC pastes are extremely low. Removal of the macrosized pores tends to lift the values upwards above unity.

Table 2.3: Some collected mechanical properties data for cements and concrete

Material system	Test geometry	K1c MNm -3/2	Flexural strength MPa	E GPa	Ref
hcp	3-point bend	0.13-0.17			139
concrete	3-point bend	0.23-0.26			139
hcp	notched beam	0.31-0.45			140
concrete	4-point bend	0.37-0.72			140
hcp	4-point bend	0.3			136
concrete	4-point bend	0.45-0.95			136
hcp	3-point bend	0.32	12.8	17.7	142
concrete		0.5-0.66	9.1	27.4	143
hcp		0.87-0.88	7.3	43.2	143
concrete	3-point bend	0.36-0.45	15-19	-	138
hcp	3-point bend	0.1	6.04	-	143
concrete	3-point bend	0.15-0.2	5.6	-	143
mortar	3-point bend	0.13-0.24	6.52	-	143
hcp	3-point bend	0.41-0.48	15.7	20.6	132
MDF	3-point bend	0.71-1.04	39.7-72.1	29-37.6	132
compacted hcp	Brazilian test	0.68	27.9	28.3	132

2.4.2.2 Indirect tension (splitting strength): The Brazilian Test

This test was developed originally in Brazil by Carnieo and Barcellos⁽¹⁶¹⁾ as long ago as 1953 and has recently come into rather general use. It has been standardised as ASTM (C496).

The indirect tensile test is an apparently simple way of testing cement in tension and does not require any other equipment than that normally found in a materials laboratory. A cylindrical mould and an ordinary Universal test machine are used. The cylindrical specimen is idealised for the purpose of developing a model of stress distributions, but for experimental purposes, in order to avoid point loading leading to excessive stress concentrations two flats are polished. Bearing strips, usually made from plywood, but here wool or sponge rubber were used, to distribute the compressive load over the flat plane are sufficient to avoid undue concentration of stress. The compressive

force produces a distribution of stress because the normal stress at any point is:

$$\sigma_n = \cos^2\theta(\sigma_1 \cos^2\psi + \sigma_2 \sin^2\psi) + \sigma_3 \sin^2\theta \quad (2.28)$$

Because the disc is thin relative to the diameter, a plane stress generalisation can be made to reduce the stress components to two tensile and one shear that contribute to σ_n . Hondores⁽¹⁶³⁾ gives expansions for σ_r , σ and T_r

for example:

$$\sigma_r = -2p/\pi[(\alpha - \sum[1-(1-n)^{-1} (r/R)^2](r/R)^{2n-n} \sin 2n\alpha \cos 2n\theta] \quad (2.29).$$

By choosing $n > 20$, a computer solution can be obtained. Few researchers have been so thorough, and the paper by Varder and Finnie⁽¹⁶⁴⁾ is an exception that uses the complete analysis to show that using the multiaxial treatment and Weibull analysis, measurement of strength based on bending beams agree well with strength values in disc tests of various rock samples.

Most workers consider only the loaded diameter and simplify the calculation to relate to tensile stress along the compression diameter. Failure along this diameter is sought and often achieved. In practice, only samples that split along the vertical diameter are used to find strength values, and this was the criterion used in this work. The maximum tensile strength acts across the loaded diameter and is given by eqn (2.30):

$$\sigma_T = 2P/\pi DL \quad (2.30)$$

Where σ_T is the splitting tensile strength, P is the maximum applied load, D is the cylinder diameter and L is the cylinder thickness.

Compressive stresses also act along the loaded diameter, and these vary from very high values immediately under the load. This is a useful feature because the compressive stress helps to minimise the effects of surface flaws.

It was perceived that, by using a cylindrical die and press, consistent specimens could be made of a modest size, i.e., 13 mm diameter and thickness around 2–5 mm and that the application of pressure to the paste would provide a more consistent microstructure.

By experiment, a pressure of 12-13 MPa was found to be satisfactory. Above this pressure, too much water was squeezed out while below it, more obvious pore size variation was apparent.

These discs could be stored in controlled humidity bell jars quite easily and in reasonably large numbers so that some statistical confidence could be gained.

Because of all these features, this particular strength test was standardised and used. It was noted, however, that the two types of tensile test, that is the 3-point bend, and Brazilian disc, give quite different results ⁽¹⁵⁹⁾. The splitting tensile test is the easiest to perform and gives more uniform results,

but they are about one and a half times greater in the value of strength than those obtained in a direct tension test. Before the decision was taken to focus on the Brazil test, considerable effort was put in to trying to develop the flexural bend test.

The two fracture parameters measured by linear elastic fracture mechanics are the critical strain energy release rate, G_{1c} , and the critical stress intensity factor, K_{1c} , often called fracture toughness, which is a measure of the crack tip stress when the crack starts to propagate.

There is a relationship between G_{1c} and K_{1c} ⁽¹⁴⁰⁾ that is given by equation (2.31) for plane stress:

$$K_{1c} = \sqrt{E G_{1c}} \quad (2.31)$$

And for plane strain:

$$K_{1c} = \sqrt{E G_{1c} (1-\nu)^2} \quad (2.32)$$

Where E is Young's Modulus and ν is Poisson's ratio.

Values obtained for both G_{1c} and K_{1c} are dependent on the specimen geometry, the type of test, and the method of measurement.

The K_{1c} parameter is often a useful representation of a material for engineering application. The test methods to determine the parameters are almost exclusively three-point and four-point bending of notched beams;

double cantilever beam (DBO) experiments; compact tension (CT); double torsion plate specimen tests and double-edge-cracked specimen tests.

Peterson⁽¹⁴¹⁾ studied the degree of approximation involved in the application of linear elastic fracture mechanics, such as the three-point bend test of a notched beam by using the formula.

$$k_{1c} = \sigma \sqrt{a} y \quad (2.33)$$

Where $y = 1.93 - 3.07 (a/d) + 14.53 (a/c)^2 - 25.1 (a/d)^3 + 25.8 (a/d)^4$ and

$$\sigma = 3 F_{\max} / 2bd^2 \quad (2.34)$$

In these two equations, F is the applied load, l is the span, i.e., the distance between the supports, b is the width of the beam, d is the depth of the beam and a is the notch depth.

Experiments on notched cement beams are hard to carry out, and the data is difficult to interpret because the porous microstructure makes control of the crack propagation difficult in such a brittle material. Davidge⁽⁹²⁾ highlighted the significant variation in the fracture toughness values obtained for cement and suggested that some variation with crack length is not unexpected.

Hillemeier *et al.*⁽¹⁴²⁾ showed that the addition of polymer dispersants and other admixture appear to decrease the fracture toughness, K_{1c} , of cementitious materials. In contrast, Beaudoin⁽⁶⁸⁾ showed that the fracture toughness of Portland cement paste is significantly increased by the

presence of mica flakes for samples of similar matrix porosity. Other work has shown that K_{1c} increases through the early stages of setting, reaching a constant value after about 28 days. This implies that the K_{1c} is dependent not solely on porosity but also on the structure, and the relative composition of the solid constituents, and on specimen size⁽¹⁴³⁾⁽¹⁴⁴⁾. Alford *et al.*⁽¹³²⁾ found the k_{1c} value of OPC pastes were between 0.41 and 0.48 $\text{MNm}^{-3/2}$ whilst compacted paste had a k_{1c} value of 0.68 $\text{MNm}^{-3/2}$ and MDF paste containing polymer dispersants had values greater than this, ranging from 0.71 to 1.04 $\text{MNm}^{-3/2}$. These data are shown in Table 2.3.

A paper of some relevance to the type of work described in this thesis is that of Kitagawa *et al.*⁽¹⁴⁵⁾ because they used a diametric compression test on discs of mortar and concrete to determine the fracture toughness of these complex, flaw-containing materials. As a result, some relevant theory for the process was presented, and it was emphasised that preparation of disc specimens was easier, giving more uniform behaviour.

This was an encouragement in that we had already decided to make such specimens for similar reasons. The discs in Kitagawa's work were much larger than those we prepared, being in the range 10-15 cm diameter and were made to contain a slit. It was not made clear whether the Kitagawa discs were pressed or just hand-laid artefacts. Each disc had a centre slit of length $2a$, the disc had a diameter of $2R$, and a thickness t , related to R . Experiments showed that slit width c , R , and a , had to be maintained within limits, for example $2c = 1 \text{ mm}$ and $2R = 100\text{mm}$ and $a/R = 0.2$, $t = 2R/c \text{ mm}$.

For mortar, which is silica bonded OPC paste, as far as we are concerned here, fracturing loads, P_F , were obviously linked to specimen size, whilst K_1 calculated from these loads was relatively constant. The value for K_1 were obtained from eqn (2.26) which had earlier been derived both by Tweed⁽¹⁵¹⁾ and Isida⁽¹⁵²⁾:

$$F = K_1 P_F / RT (d/\pi)^{1/2} \quad (2.35)$$

This equation applied as long as a/R was in the range 0-0.4; F was dependent on a/R according to equation (2.36):

$$F = 1.0 + 1.5 (a/R)^2 \quad (2.36)$$

Further analysis of the way that K_1 values varied with specimen dimensions led to the concept of equivalent crack length whereby the notch, $2a$, has an added value, x , arising from the fact that flaws and inhomogeneities are present in mortar and act to effectively increase the notch length.

Equation (2.37) was derived relating the parameters of two different sized discs R_1 and R_2 :

$$(P_{F1}/R_1^{3/2})\sqrt{(a_1+x)/R_1[1+1.5(a_1+x)/R_1]^2} = (R_{F2}/R_2^{3/2})\sqrt{(a_2+x)/R_2[1+1.5(a_2+x)/R_2]^2} \quad (2.37).$$

Application of equation (2.37) to two different sized discs enabled, x , to be quoted as $0.6837 \times 10^{-3}m$ which is interesting in the light of the sizes of macro defects proposed by Birchall earlier. For fixed values of x , as the sample R is increased, the concept of crack length has less meaning, and

the measured notch length $2a$ can just be used with eqn. (2.35). Comparison of three-point bend results and the results from eqns. (2.35) and (2.37) were good: K_{1c} , from fracture load for 10cm discs, of $0.45 \text{ MNm}^{-3/2}$ and $0.468 \text{ MNm}^{-3/2}$ for 15 cm discs respectively while K_{1c} was $0.487 \text{ MNm}^{-3/2}$ for both discs using equation (2.37). These are comparable to the three-point bend value of $0.481 \text{ MNm}^{-3/2}$. Hence, this method, at least for large discs, appears convenient and reasonably accurate. However, the pressed discs in the research done here were considerably smaller and could not be conveniently slit; hence, the method could not be applied.

This resulted in the investigations of the following:

- 1- Hardness indentation to find K_{1c}
- 2- A closer look at the diametral compression test
- 3- Some consideration of statistical aspects

2.4.2.3 Statistical examination of ceramic strength data.

Generally ceramics are brittle materials; small specimens of brittle materials may exhibit large variations in fracture stress. Davidge⁽¹⁶⁸⁾ summarised two reasons for this variation:

- (i) There are inaccuracies in the test method that include the sensitivity of the measuring device and the accuracy of specimen dimension measurement in a mechanical property test.
- (ii) There is a genuine variation from specimen to specimen. This variation could be related to the size variable in the Griffith equation, expressed as eqn (2.22). Hence, variation in strength should be related to

the distribution in size of an appropriate micro-structural feature, which may be crack size, pore size or grain size. This introduced the need for a statistical component in fracture analysis.

Fracture statistics is based on a consideration of three elements which are as follows:

- (i) Extreme value statistics
- (ii) Fracture mechanics
- (iii) Material microstructure

One immediate question arises from the large number of statistical functions that can be applied to analyse the variations in the strength of ceramics; which function is best applied? The particular function which has assumed a prominent position was developed by Weibull⁽¹⁶⁹⁾. Weibull's model of a brittle material is that it is homogenous, isotropic and has uniformly distributed randomly oriented flaws. Despite these extremely broad assumptions, much useful data has emerged from using the technique. To this model, he applied the weakest link theory. It is assumed that a brittle solid can be approximated by a series model, that is, the strength is that of the weakest unit, and there is no interaction between flaws and that failure occurs when the strength as determined by the worst flaw is reached. Only tensile stress is assumed to cause the failure.

Consider a chain of N links in which individual failure probabilities, at a given load, are $F_1, F_2, \dots, F_i, F_n$ which can be used to define P and S , the failure and

survival probability, respectively of the chain as a whole. The probability that the chain survives is the product of the individual survival probabilities:

$$S(\sigma) = 1 - p(\sigma) = \prod (1 - F_i) \quad (2.38)$$

If F_i is small, we can generalise this result to a volume composed of elements dV which may be under different tensile stress, σ .

Weibull proposed for a uniaxial stress the following two parameter expression:

$$F_i(\sigma) = (\sigma/\sigma_0)^m dv \quad (2.40)$$

Therefore, the failure probability is given by:

$$P = 1 - S = 1 - \exp(-\int (\sigma/\sigma_0)^m dv) \quad (2.41)$$

Where σ_0 is a scaling constant which has the dimension of stress and m is the Weibull parameter, sometimes called flaw density parameter. Equation (2.40) was further modified to a three parameters expression by introducing the concept of a threshold stress below which failure does not occur. For the three parameters distribution, we have equation (2.42):

$$P(\sigma) = 1 - \exp[1 - v (\sigma - \sigma_u)/\sigma_0]^m \quad (2.42)$$

This is the fundamental equation of the failure probability of the applied stress, σ , v is the volume of the specimen, σ_u is a threshold stress below which the probability of failure is zero, which for ceramics is usually taken a

zero. Thus, the larger the value of m the less variable is the strength of a material.

Ceramics have values of m between 5-20 compared to metals where m values lie between 40 and 60 ⁽¹⁷³⁾.

Equation (2.41) can be written in a linear form by taking the logarithm twice and rearranging this:

$$\ln \ln(1/(1-P(\sigma))) = \ln v + m \ln(\sigma - \sigma_0) - m \ln \sigma_u \quad (2.43)$$

So a plot $\ln \ln 1/(1-P(\sigma))$ against $\ln \sigma$ should result in a straight line the slope of which gives the m parameter when P , the failure probability, is expressed as:

$$P = J/(N+1)$$

J is the ranking position within N the number of tests.

By applying uniform stress on two different specimen of volume v_1 , v_2 the probability of survival is given by:

$$\sigma_{v1}/\sigma_{v2} = (v_1/v_2)^{1/m} \quad (2.44)$$

Which demonstrates the observed situation that the larger the specimen the lower its strength.

2.5 Zirconia (ZrO₂)

Determining the effect on strength, modulus and hardness that replacing porosity with zirconia would have is a major aim of this research and so to

complete the introduction a review of zirconia is necessary.

Zirconia, a tough ceramic material ^{(84), (85)}, has the potentially useful property of imparting toughness to ceramic matrices. This usefulness arises from its crystal structure. Pure zirconia has three polymorphic forms, cubic, tetragonal, and monoclinic. The high temperature form, stable from about 2370⁰C up to a melting point of 2680⁰C, is cubic and has the fluorite-type structure in which each Zr⁴⁺ is coordinated by eight equidistant oxygen ions and each oxygen ion is tetrahedrally coordinated by four zirconium ions.

A tetragonal phase is stable between 1170⁰C and 2370⁰C. It has a less symmetrical structure in which each Zr⁴⁺ ion is surrounded by eight oxygen ions, at a distance of 0.2455 nm and the other four at a distance of 0.2065 nm⁽⁸⁶⁾.

From room temperature to around 1170⁰C the stable phase has the baddeleyite structure, with a monoclinic unit cell of $a = 0.5174$, $b = 0.5266$, $c = 0.5308$ nm and $\beta = 80.2^\circ$. The structure of this form, as determined by x-ray diffraction analysis ⁽⁸⁰⁾, has sevenfold coordination of Zr⁴⁺, with Zr-O distances of 0.205 to 0.228 nm. Layers of triangularly coordinated O₍₁₎-Zr and tetrahedrally coordinated O₍₁₁₎-Zr, in which all the Zr⁴⁺ ions are located in layers parallel to the (100) plane, separated by O₁ and O₁₁ ions on either side exist in the structure.

Having these three forms, zirconia exhibits the following transformations:

1170°C 2370°C 2680 ° C

Monoclinic → Tetragonal → Cubic → Liquid

It must be emphasised that the transformation of monoclinic to tetragonal is most unusual in that a substantial volume decrease occurs, variously quoted as 8-14 % ⁽⁸¹⁾.

This decrease in volume results in tensile stress being generated in zirconia artefacts that usually then fracture at the transition. However, if metastable zirconia in the tetragonal form can be obtained at room temperature, then the reverse transformation to the monoclinic modification, initiated by stress, could be of some value in improving the mechanical properties by generating crack-closing compressive stresses in the system. Over the past 30 years, this possibility has been well researched ^{(89) (90)}. Recent reviews ^(90, 91, 180) identify two related mechanisms for improving toughness via zirconia transformations in mixed composite systems of matrix ceramic plus zirconia, these can be briefly summarised as:

1- The increase in volume produces many microcracks in the zirconia-matrix interface, so an increase in fracture energy is needed to make all cracks grow. In this case, it is obviously important to restrict the distribution of these microcracks so that they do not merge to produce long cracks and so drastically reduce the strength as we would expect from the classic Griffith equation (2.22).

2- The volume change does not cause cracks because the modulus of the matrix is sufficiently high, and /or the volume of zirconia is too low, but produces a compressed zone in the region of each zirconia particle that inhibits primary crack growth.

These mechanisms depend upon the production of a metastable tetragonal phase that will transform under the influence of the stress field that precedes a crack. As a result, considerable effort has been put into the preparation of such a phase and retaining it in ceramic-composite artefacts. When tetragonal zirconia is successfully incorporated as a second phase into a host matrix, two different effects can occur depending upon whether the zirconia is wholly retained as the tetragonal phase or part is transformed to the monoclinic phase in the fabricated ceramic.

In the first case, one can get toughening plus strengthening, in the second, one can find toughening but commonly without strengthening ⁽⁹²⁾.

In order to achieve the desirable situation of improved toughness and strength, some parameters must be met: the particle size of zirconia must be very fine, typically 1 μ m or less; secondly, the zirconia must be well distributed. Thirdly, the rigidity modulus of the matrix must have an optimum value.

Several strategies have been developed to achieve the first of these requirements and maintain tetragonal zirconia during processing. The

earliest of these was to use solid solution stabilisation whereby cubic oxides such as Y_2O_3 ⁽⁹³⁾, CaO ⁽⁹⁴⁾, MgO ⁽⁹⁵⁾, are dissolved in the zirconia structure in amounts in 1-10 mole% range. Such stabilised zirconias have advantages and disadvantages. The main disadvantages, in the context of the work to be undertaken here, is that they are often too stable to easily convert to the monoclinic modifications on application of modest stress concentrations. Furthermore, they are frequently more chemically reactive because of the charge mismatch, e.g., Mg^{2+} for Zr^{4+} which is balanced by the presence in the structure of a high concentration of anionic defects. More detailed consideration of the nature of the monoclinic to tetragonal transformation has led to other possible ways for metastable retention of tetragonal zirconia. For example, Bansal and Heuer⁽⁹⁶⁾, who obtained single crystals of monoclinic symmetry and cycled these crystals through the transformation, proved conclusively that the transformation was of the brittle martensitic type and therefore nucleation control was all important. This focused attention on the mechanism of the transformation. More detailed studies of the nucleation of the process are necessary, if control is to be sought via nucleation. One part of the research presented in this thesis identifies the transformation from amorphous zirconia to a crystalline modification as a surface phenomenon which means that it may be controlled by surface additions.

Garvie⁽⁹⁷⁾ considered that fine particles of the tetragonal form are stabilised because the surface energy of the tetragonal phase is lower than that of the monoclinic phase. Assuming that Garvie's suggestion is correct, the preparation of fine powders of zirconia is essential in this area of technology

if one wants the tetragonal form.

Particle size, as well as controlling the tetragonal content, is an important parameter in the toughening mechanisms so far reported and reviewed^(98, 99). Lange⁽¹⁰⁰⁾ found that retention of the tetragonal structure at room temperature or below is critically dependent on the grain size of the microstructure. Garvie⁽⁹⁴⁾ noted that unconstrained tetragonal zirconia powders are obtained at room temperature when produced with a particle size less than 30 nm.

The tetragonal \rightarrow \longrightarrow monoclinic transformation takes place when the particles and the matrix system can reduce the total free energy.

Eshelby⁽¹⁰³⁾ expressed the change in free energy between the two lattice modifications per unit of transformed volume as:

$$\Delta G = \Delta G_{\text{chem}} + \Delta U_{\text{T}} + \Delta U_{\text{a}} \quad (2.45)$$

In eqn (2.20) ΔG_{Chem} is the chemical free energy difference between the transformed and untransformed material, ΔU_{a} the applied strain energy, and ΔU_{T} is the transformational strain energy, which is modified by an applied stress according to equation (2.46):

$$\sigma_{\text{a}} = -\Delta U_{\text{a}}/\epsilon_{\text{T}} \quad (2.46)$$

In eqn (2.35) ϵ_{T} is the transformational strain.

The condition required for the transformation to occur is:

$$-\Delta U_a > (\Delta U_T + \Delta G_{\text{chem}}) \quad (2.47)$$

Thus, the applied stress necessary to cause the transformation should have a threshold value given by equation (2.48):

$$\sigma_a > (\Delta U_T + \Delta G_{\text{chem}})/E \quad (2.48)$$

As already outlined, different possible mechanisms of toughening may operate via the tetragonal \rightarrow monoclinic transformation in zirconia which then has the potential to increase the toughness of ceramic composites. The favoured mechanisms have been described in more detail in the literature:

2.5.1 Stress-induced transformation toughening in matrix plus Zirconia composites

This mechanism is based on the existence of well-dispersed zirconia precipitates, or small, retained grains, kept in the metastable tetragonal form, that can be induced to transform to the monoclinic form by the stress field associated with the crack tip of an extending crack ⁽¹⁰⁴⁾. McMeeking and Evans ⁽¹⁰⁵⁾ have pointed out that if a crack is made to extend under stress, large tensile stresses are generated around the crack tip which relaxes the matrix constraint on the tetragonal zirconia particles, hence allowing them to transform to the monoclinic modification with a resultant localised volume increase.

The stress associated with a crack tip, σ_T , may be approximately represented as:

$$\sigma_T = K_1 r^{-1/2} \quad (2.49)$$

In this equation K_1 is the stress intensity factor at a distance, r , from the crack tip. It is imperative that the crack tip must be able to generate a local stress equal to, or greater than, that necessary to transform metastable zirconia particles as given by eqn (2.49). The relevant volume expansion and shear strain developed in the particles causes a resultant compressive strain being generated in the matrix.

Garvie *et al.* ⁽¹⁰⁶⁾ have shown how higher strengths can occur as a result of this process from the absorption of energy during the martensitic transformation from tetragonal to monoclinic forms. Trunec and Chlup ⁽⁹¹⁾ believe that the increase in fracture energy is caused by the volume and shape changes of the particles ahead of the crack tip due to transformation counteracting the stress distribution.

McMeeking and Evans ⁽¹⁰⁵⁾ have given an equation for the toughening increment arising from this mechanism:

$$\Delta K_T = 0.22[V_f e^T E/h(1-\nu)]^{1/2} \quad (2.50)$$

Where ΔK_T is the transformation toughening increment as calculated at any given temperature T , V_f is volume concentration of the tetragonal zirconia, e^T

is the unconstrained dilatational transformation, E is Young's modulus of the matrix, ν is Poisson's ratio of matrix and h is the width of the transformation zone.

This shows that the increment of fracture toughness depends on the magnitude of the mechanical properties of the matrix. Also, from this equation and the assumed mechanism, the following parameters can be adjusted to optimise the toughening effect:

- (i) Zirconia particle size as small as possible, with a mono-dispersed particle size distribution, in order to maintain the tetragonal form during fabrication.
- (ii) Maximise the volume fraction of tetragonal zirconia particles for example by solid-state precipitation reactions as in partially stabilised zirconia (PSZ).
- (iii) Choose a matrix with high Young's modulus for maximum zirconia constraint.

2.5.2 Micro crack toughening

The micro crack nucleation mechanism implies that the increase in fracture energy is due to the formation of a large number of small micro cracks. Micro cracks can be induced by incorporation of a second phase zirconia particle in the ceramic matrix at high temperature when it is tetragonal and allowing it to transform to the monoclinic form on cooling. The volume expansion causes these micro cracks to form, which are generated by high tensile stresses,

around the transformed particle. They can be extended in the stress field of a propagating crack to dissipate the crack energy, which means the ceramic's toughness is increased, but the strength is reduced.

In the nucleation of micro cracks, elastic energy is converted into surface energy, according to eqn (2.51):

$$K_{1c} = K_0 + (2E \gamma m r)^{1/2} \quad (2.51)$$

Where: K_0 is the toughness of the matrix; E is the Young's modulus of matrix, γ is the specific energy of the crack surfaces, m is the micro crack area density and r is the radius of a stressed process zone of cylindrical shape. The micro crack area density is related to zirconia particle size, d , through $m = (v/d)F$, where v is the volume fraction of tet-ZrO₂ and F is a function which has $1/d$ as a variable.

Claussen ⁽¹⁰⁸⁾ has shown that the volume fraction of zirconia inclusions must be in an optimum range to obtain maximum toughness increase without a significant strength decrease, because if the Zirconia particles are near enough to interact with each other, a drastic decrease in strength results due to the generation of merging micro cracks. Davidge and Green ⁽¹⁰⁹⁾ found that for zirconia particles to induce micro cracks that act as failure nuclei, the particle size d must be $\leq d_c$ where:

$$d_c \geq C/\sigma^2 \quad (2.52)$$

In eqn (2.52) C is a given inclusion particle size and σ is the hoop stress. Green ⁽¹¹⁰⁾ has pointed out that micro crack size and volume density are initially related to the zirconia grain size and volume fraction. A consideration of the analyses in the literature indicates that toughening by micro-cracks may be optimised by:

- (i) Making smaller particle size zirconia with a narrow particle size distribution and adjusting the thermal mismatch between zirconia and the matrix phase.
- (ii) Using a matrix of high inherent fracture toughness, high grain boundary energy and high Young's modulus.

2.5.3 Surface toughening

This technique suggests that both strength and toughness may be increased by introducing compressive stresses in the surface layers of an artefact. This stress acts against the major defects that occur from handling and machining. Compressive stress can be obtained by transforming tetragonal particles in the surface layer to monoclinic symmetry and maintaining those in the bulk as the tetragonal polymorph. The phase transformation can be produced by grinding ⁽¹⁰⁸⁾ or chemically destabilising tetragonal or cubic particles near the surface and allowing them to transform.

The surface toughening is expressed by a critical stress intensity factor:

$$K_{ST} = K_{1C} + K_C \quad (2.53)$$

K_{1c} is the fracture toughness of the composite and K_c is the stress-intensity factor due to the compressive field. K_c is estimated from eqns (2.54) and (2.55):

$$K_c = \beta \sigma (\pi a. M)^{1/2} \quad (2.54)$$

$$M = 1 - (2a/\pi S) \quad (2.55)$$

In the last two equations β is a geometrical factor, M is a correction factor, a is the flaw size and S is the transformation depth.

In summary, it appears that toughening by zirconia addition inevitably involves the interaction of monoclinic zirconia with tetragonal zirconia, since either the advancing stress field has transformed the tetragonal zirconia to monoclinic or earlier, the forming or processing activities have induced the transformation. Thus, one is concerned with micro crack zones in the matrix, or areas in compression, both of which contribute to higher values of γ in the composite.

This brief summary of the mass of detailed work over the past twenty-five years does suggest that there are still some technological aspects to be considered and solved in the use of zirconia as a ceramic additive. Many of these problems concern powder preparation and how composites can be fabricated. Predominant research on zirconia involved studies pertaining to high temperatures and associated equations. However, additional studies are required to fully understand properties at lowered temperatures.

In this work, we will be attempting to introduce tetragonal zirconia in to pre-existing pores to develop a room temperature composite of hydrated OPC and zirconia as well as dispersing tetragonal zirconia in OPC and then forming by hydration.

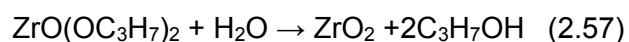
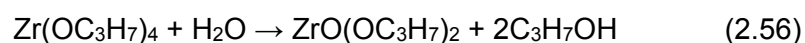
Here now are some of the zirconia preparation and dispersion techniques, which have so far been tried:

2.5.3.1 Sol-gel technique

The sol-gel method is being used successfully in a wide range of applications because of its ability to produce spherical powders of same-sized particles from aqua sols. Tirgensons and Stranmanis⁽¹¹¹⁾ defined a sol as a dispersion of solid particles, called the disperse phase, in a liquid, called the dispersion medium, in which the diameter of the solid particles is in the range of 1-1000 nm so that each contains 10^3 - 10^9 atoms. At this size range, in order to minimise surface energy, the disperse phase has a spherical habit, and will be the tetragonal or cubic form of ZrO_2 .

A gel phase results if the sol viscosity increases following depletion of the dispersion phase. Eventually the gel becomes rigid.

The following equations involving zirconium propanolate and water summarise the process for zirconia production:



There are several advantages of the sol-gel technique:

1. Better purity and homogeneity from the use of high purity precursors being mixed as solutions.
2. Low temperature of preparation which saves energy and minimises evaporation losses; gives no reaction with containers, and generally leads to non-crystalline products.

Some of the disadvantages are as follows:

- 1 Long processing times
2. High cost of raw materials
3. Large shrinkage during processing
4. Residual fine pores and trapped hydroxyl ions
5. Health hazards of organic solutions

2.5.3.2 Solution-Suspension Method

At least one of the components in this method should be in the form of a sol, and the other a solution of the salts that on evaporation will become the additive. It is possible to control purity since methods such as precipitation or crystallisation are involved.

Sulphates and chlorides are the most commonly encountered salts for the solution method. Homogeneity is maintained and powder agglomeration is minimised in this method usually by pH control.

In a work pertinent to this research, Witek and Butler ⁽¹¹²⁾ found that fracture strength and toughness are increased when mixing zirconium containing

solutions with alumina sol because homogenous dispersions of zirconia particles in the matrix were produced.

Kosmac *et al.* ⁽¹¹³⁾ used yttrium nitrate as a solution and mixed into this tetragonal zirconia sol as a means of increasing the amount of retained tetragonal zirconia.

2.5.3.3 Mechanical Mixing

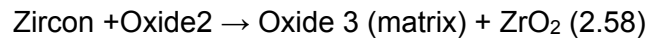
As far as the ceramics industry is concerned, this is the common method for composite preparation. Powder components, especially oxides, are wet mechanically mixed using a ball mill or by using an attrition mill⁽¹¹⁴⁾. The main disadvantages of this route are that it adds impurity, which contaminates the powders, and it cannot produce ultra-fine powders, since the particle diameter limit is about 1.0 μm .

Despite the above problem, Claussen and Jahn ⁽¹¹⁴⁾ found that simple mixing of zirconia with Si_3N_4 produced an improvement in mechanical properties of the nitride matrix phase. Also, by introducing zirconia particles into an alumina matrix by this route, Claussen *et al.* ⁽¹⁰⁷⁾ found that when the particle size of zirconia is small, the toughness increased with the volume fraction of zirconia, as too did the strength.

2.5.3.4 High Temperature Chemical Reactions

The decomposition of zircon, ZrSiO_4 , at temperatures above 1750 $^{\circ}\text{C}$, has been used to prepare oxide matrices in which zirconia is well dispersed. The

main drawback is dehydration at lower temperatures (50-70°C) but which can be prevented by combining it with tungsten or yttrium, which can be separated later upon culmination of the reaction. The reaction is summarised as:



A typical reaction for the above equation that has been quite extensively studied is found in the work cited as references (115) and (116) and expressed as eqn (2.48):



2.5.3.5 Vacuum Filling

Most ceramics pass through a processing stage in which the material is highly porous, and instead of viewing this as a necessary evil, it can be used to introduce additional material into the ceramic as solution, sol, or slurry.

However, even though this has not been a commonly used or well-explored route, it was chosen as the desired route for this work. A method similar to the one designed for this work has been reported earlier for ceramics ⁽¹¹⁷⁾ reporting a method similar to that developed in the early stage of this work. Firstly, the ceramic matrix sample should be evacuated for sufficient time to allow the gas deep within the solid to diffuse out and then back filled with a solution containing zirconium ions such as zirconium nitrate or oxychloride. The filling depth is controlled by the filling time and degree of interconnecting porosity. However, the infiltrant may react with the free surfaces of the compact to form a chemically new surface or it may even dissolve the

surface. If it does not react, it will form a composite usually with more zirconia in the surface layer. Secondly, after drying, a heat treatment, about 400°C, is used to decompose the zirconium salt to give the tetragonal form of zirconia.

CHAPTER THREE

EXPERIMENTAL TECHNIQUES

3.1 Materials used in this study

The cement material under consideration and used was an Ordinary Portland Cement (OPC) which has been made available by the firm Blue Circle Cement Plc, UK, part of Lafarge group since 2001 who also provided the analysis given in Table 3.1.

The total oxide composition is given at 99.6% which reflects the loss on ignition and the lack of inclusion of insoluble residue in the elemental composition.

Table 3.1

Analysis of the cement used for all this work

Oxide	Content wt%
CaO	65.8
SiO ₂	21.1
Al ₂ O ₃	5.6
Fe ₂ O ₃	2.3
MgO	1.1
SO ₃	2.9
Na ₂ O	0.19
K ₂ O	0.62

The phase composition was given as C3S = 57.5%, C2S = 19%, C3A= 11.0%, C4AF= 7.0% and it had a surface area of 388 m²kg⁻¹, and lime saturation factor (LSF) of 98.9 %.

The reagents used in conjunction with this cement were Analar grade as supplied by BDH chemicals limited, these were:

- 1- Zirconium nitrate, $Zr(NO_3)_4$.
- 2- Zirconyl chloride (Zirconium oxychloride) $ZrOCl_2 \cdot 8H_2O$.
- 3- Zirconium tetrachloride anhydrous, $ZrCl_4$.
- 4- Zirconium silicate (colloidal suspension) $ZrSiO_4$.
- 5- Stannous chloride, $SnCl_2 \cdot 2H_2O$.
- 6- Ferric nitrate, $Fe(NO_3)_3 \cdot 9H_2O$.
- 7- Ferric Chloride, $FeCl_3 \cdot 6H_2O$.
- 8- Ammonia Solution, NH_4OH .

3.2 Preparation of zirconia powders

Several methods were investigated to prepare tetragonal zirconia for these experiments. The different methods were selected in order to facilitate comparison and identification of a suitable method that aligns with the aims of the project:

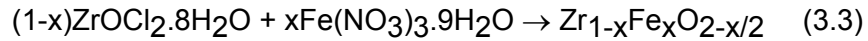
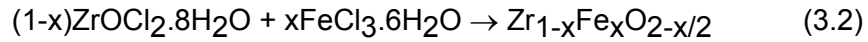
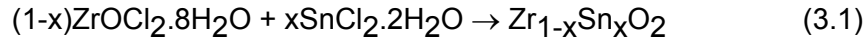
1. Calcination of zirconium nitrate.
2. Precipitation of a gel from zirconyl chloride or zirconium tetrachloride solutions followed by calcination.
3. Precipitation of a gel from zirconium nitrate solution and calcination.
4. Precipitation as a mixed silica-zirconia gel from zirconium silicate solution and subsequent calcination.

5. Precipitation of mixed gels from zirconium nitrate solution doped with stannous chloride solution followed by calcination.
6. Precipitation of mixed gels from zirconium nitrate solution doped with ferric nitrate or chloride solutions followed by calcination.

The gels were made at different pH levels, and under controlled conditions using concentrated ammonia solution, added drop-wise, with vigorous stirring. The ammonia solution was added drop-wise to each solution, the pH of which had been adjusted with acid or alkali and monitored with a pH meter during the addition to keep the mean pH within a chosen range. The precipitate was allowed to settle and the supernatant liquor decanted before filtering with Whatman filter papers. The filter cake was washed several times with distilled water until the chloride ions, in the case of oxychloride and tetrachloride methods were removed from the gel. Absence of Cl^- was concluded when silver nitrate solution failed to give an opaque shade on adding it to the washings. The papers containing the gel were dried in a fan oven at 110 °C or freeze dried by continued pumping on an Edwards's rotary vacuum pump for 24 hours.

The resultant hard glassy lumps from the oven-dried material were ground in a mortar and pestle in to a fine powder before thermal analysis to determine the transformation processes involved. Freeze-dried powders were soft, of low density, and non-aggregated. Different molar percentages of tin or iron dopant into the zirconia were achieved by pre-mixing appropriate volumes of

stock 0.5M zirconium solution with 0.5M tin or iron stock solutions. The equations that satisfy the solid solution formation after heating are:



3.3 Cement disc preparation

A weight range of 1–10g OPC was added to a beaker containing distilled water by volume from a burette to obtain the required water to cement ratio (w/c) of 0.5 and then mixed by hand, at room temperature. Samples for setting and testing were prepared in the form of discs (13mm diameter) using a Beckman-RHC LTD KBr die (Model K-13) and a hydraulic press. The paste was pressed uniaxially under pressure (12–13 MPa) over a duration of one minute, which was subsequently reduced to ambient pressure. These discs were allowed to hydrate in a humid environment (100% relative humidity) inside a dessicator over two weeks at room temperature. The discs were then allowed to dry under ambient humidity in the laboratory.

The purpose of compaction was to produce consistent low porosity pastes and samples suitable for strength testing by the Brazilian test.

3.3.1 Fabrication of OPC-ZrO₂ composites

(a) Wet mixing of OPC and tet-ZrO₂

Zirconia gel was heated to just beyond the transition temperature to yield tetragonal zirconia, then crushed to a fine powder. A measure (0.5–15 wt %) of tetragonal zirconia was mixed mechanically with OPC as a dry powder for 24 hours in a rotary mixer or a vibromill.

Distilled water was added to the mixture in amounts needed to obtain different w/c ratios. A paste was formed as before and pressed into disc as described in section 3.3.

(b) Calcining of gel in situ

Measured weight percentages of the dry gel in the range 0.5-12 wt% were mixed mechanically with OPC for 24 hours in the rotary mixer and the resultant mixture was heated to the gel transition temperature to convert it to tetragonal zirconia. The mixture was cooled and the requisite amount of distilled water was added to produce the paste by mechanical mixing. A tendency to flash setting due to dehydration of gypsum and formation of anhydrite after this procedure made the paste production more difficult.

(c) Vacuum infiltration

Since most ceramics, especially cement, pass through a processing stage in which the material is highly porous, this stage is considered as an appropriate point to introduce additional materials into such pores. Thus a process that involves infiltrating a solution or suspension into a set sample

after 4 weeks was designed. In this method, the infiltration depth can be controlled by varying the infiltration time but in this work this was kept constant at 20 minutes per filling. The porosity removed depends on the volume of infiltrating solution and the depth to which it entered the disc and this was varied in this work.

Discs were first evacuated overnight before filling and also after removal from the filling media in order to evaporate solvent or suspension medium and leave the original dissolved solid in the pores. This was done on the apparatus shown in Fig.3.1.

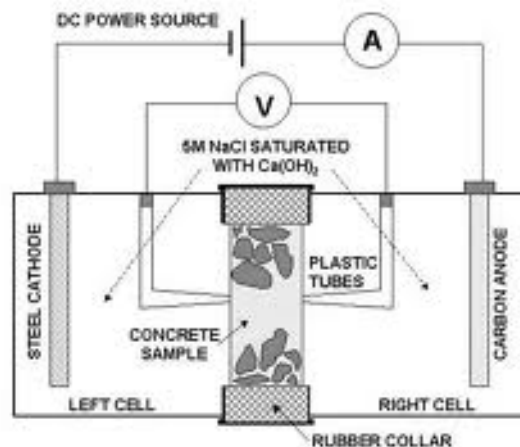


Figure 3.1: Apparatus used for solvent evaporation from cement discs

Most infiltration experiments were tried with $Zr(NO_3)_4$ solution, $ZrO_2 + 7\%$ SnO_2 solution or tetragonal-zirconia-water suspension. For the solution method samples were heated to $400^\circ C$ after each filling or after each 5 fillings to decompose the nitrate but this step was not necessary in the case of the suspensions. The amount of infiltrants and the oxides after the heating, were estimated by weight gain after each filling and heating. Heating

to 400 °C obviously involved cement hydrate decomposition and in the end this method was found to have too many uncertainties so that colloidal suspension work becomes more important.

3.4 Characterisation

3.4.1 Combined thermogravimetry differential thermal analysis

(TG/DTA)

The differential thermal analysis technique allows transitions in a material to be studied by recording the differences in temperature between the material under analysis and a known reference material both subjected to the same linear heating rate. Any transitions that occur in the sample will give rise to either an exothermic or an endothermic effect that may appear as a peak or a baseline change on the DTA trace depending on the kinetics of the process. The small variations in temperature between the sample and reference are picked up by thermocouples, which in this case were Pt/Pt-13%Rh, and fed into an amplifier and then to a chart recorder as sketched in Fig 3.2. A Stanton Redcroft ST780 combined thermogravimetric differential thermal analyzer was used with α -alumina for the reference material. The α -alumina was obtained from BDH Chemicals Limited and had a mean grain size of 12–20 mesh.

Measurements were made in flowing air at a heating rate of 10 °C min⁻¹ for most of the work. However an interesting study was made using different heating rates from (5-99 °C min⁻¹) to study the effect of heating rate on the

crystallisation exothermic peak temperature of the ZrO_2 amorphous to crystalline transition in order to measure the activation energy of the process. Some tests were made on the DTA apparatus to see if hydration rates might be detected for free OPC and for OPC containing various form of ZrO_2 . In these tests 40 mg of OPC or OPC + tet- ZrO_2 were used and hydration was begun by adding water so that the w/c ratio was about 0.5. The sample pan was covered with a foil lid and a trace taken for 24 hours. This technique whilst not of absolute value proved useful in a comparative way in the case of the immediate reaction between H_2O and the powders but was not useful for the slow long-term hydration reactions. This was because, heat generation was low in hydration over short-term in contrast to long-term hydration where heat generation was directly proportional to hydration time until the attainment of a plateau (Figure 2.2).

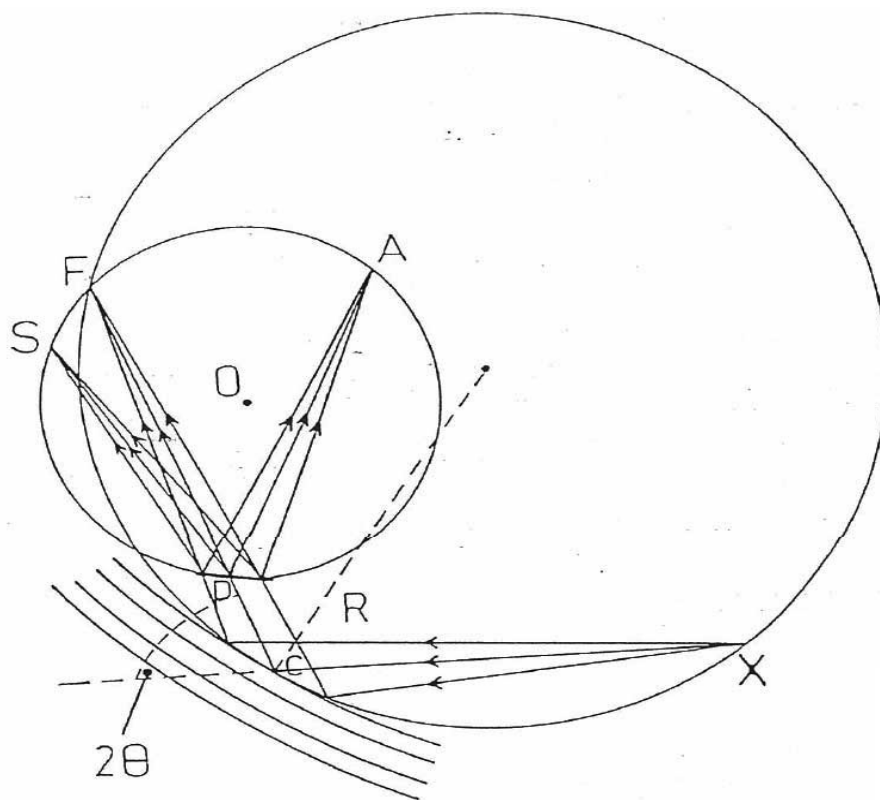


Figure 3.2 (DTA/TG) Block diagram of a typical XRD system¹⁷⁶

X: Line focus of x-ray tube

Y: Focal Line

C: Axis of monochromator crystal

R: Radius of monochromator focusing circle

O: Centre of film holder

P: Centre of powder specimen

A: Diffraction line in the additional case

S: Diffraction line in the subtraction case

2θ : Angle of x-ray beam deviation at the monochromator

3.4.2 Thermogravimetry alone

The availability of very sensitive microbalance equipment with and without a differential thermal analysis capacity (DTA), suggested that a series of water vapour absorption tests might be carried out. This data would be useful in evaluating the solvent absorption capacity of the prepared zirconia which would further function as a confirmatory method to for the efficacy of the solvent vacuum process. Additionally the thermogravimetric method by itself is not adequate to quantify solvent absorption by the sample. There was also the possibility that some insight into the effect of zirconia on the hydration processes might be gained by adding liquid water to the powders in this type of apparatus. It was felt that such work might enhance the information available from the Vicat needle setting experiments.

The Electrobalance is based on the null-balance principle, which is generally accepted as the most accurate and reliable technique of measuring changes in mass. When the sample mass alters, the beam will deflect moving the flag, changing the intensity of light falling on the photocell and hence the signal from the cell. The photo-generated current is fed into the input stage of a 2-stage servo-amplifier whose output is applied to a coil attached to the beam. The coil is contained in as uniform a magnetic field as possible allowing the current in the coil to exert a force on the beam to restore it to its original position. The change in the moment produced by the current is proportional to the change in mass. As the change in the current is practically instantaneous the beam is stated by manufacturers as not to deflect at all. The restoring force is so fast that the beam appears visually to be locked in

position.

By Ampere's law, the electromagnetic restoring force is directly proportional to the current in the coil and hence the mass. To display the various mass ranges, the coil voltage is backed off using a range of accurate standing voltages so that the recorder only displays the variations in a mass range. Variations of the standing voltage and amplification give a wide range of masses. A low pass filter is used to reduce stray forces such as vibrations.

The Cahn Balance is housed in a bell-jar, made of Pyrex that has a volume of 3.5 litres. Down tubes are attached via B40 cones and sockets, the one on the sample side is water cooled to protect the vacuum grease and minimise error due to expansion of the balance arm. The sample tube consists of a silica bottom joined through graded seals to normal Pyrex glass. The sample holder is made of silica and is suspended by a silica fibre so that the container is as close to the thermocouple as possible. The down tube on the tare side is made of Pyrex. The whole assembly was attached to a conventional vacuum and gas-handling rig via a ball and socket joint. The sample mass of approximately 40 mg is suspended from the outer loop of the balance arm, thus giving maximum sensitivity. The sensitivity was adjusted so that the chart paper width represented 10mg so 1 unit of the chart paper, which can be easily read, represents 0.1mg, 0.25% of the sample mass. The balance is mounted on an outside wall below ground level reducing mechanical vibrations and electrical surges ensuring that the balance worked well within its specifications.

A Stanton Redcroft linear temperature programmer provides temperature control around the specimen. This unit incorporates a motorised linear potentiometer that provides a steadily varying voltage corresponding to that generated by a thermocouple when heated or cooled at a uniform rate. A number of workers have discussed the conversion of Cahn electrobalances to thermobalances.

3.4.3 X-ray powder diffraction

Most powder x-ray diffraction data was obtained using a Guinier-Hägg focusing camera, XDC-700 on a Philips generator, employing $\text{CuK}_{\alpha 1}$ radiation ($\lambda = 1.54059 \text{ \AA}$).

The curved crystal serves to monochromate and focus the x-ray beam. The main beam is diffracted by the bent quartz crystal and one diffracted beam is focused on to a circle radius (R). This circle becomes the circumference of the film holder. Powder thinly spread on sellotape is placed in the path of the reflected beam and the x-rays are diffracted to the film. The focusing camera has advantages over the Debye-Scherrer in that it gives a much clearer pattern with twice the resolution for a smaller exposure time, and the value of the wavelength used is known exactly. Absorption errors at low values of θ are also greatly reduced. However, it has disadvantage that only a limited range of θ may be covered.

The film constant k, was determined by taking repeated exposures of high purity silicon and KCl powder and produced a value of $k = 0.286707$. This

constant was checked periodically and found to vary by less than 0.01%.

Lattice d-spacing, but more usefully $\sin^2\theta$ values, were calculated from the Bragg equation:

$$\lambda = 2d\sin\theta \quad (3.4)$$

The lattice parameters were calculated where necessary after indexing of the observed patterns.

In much of this work it was necessary to determine the relative percentages of different zirconia phases and the method given by Schmid ⁽¹¹⁷⁾ was used. This involves equation (2.5) and x-ray line intensity measurements:

$$f(t) = I_t(111)/[I_t(111) + I_m(111)] \quad (3.5)$$

In this equation $f(t)$ = tetragonal zirconia fraction, $I_t(111)$ is the intensity of the tetragonal phase (111) peak and $I_m(111)$ is the intensity of the monoclinic phase (111) peak.

3.4.3.1 Crystallite size determination

Crystallite size, D , was determined by using the Scherrer equation ⁽¹²⁰⁾ which is related to the breadth of diffraction lines at half peak-height:

$$D_{hkl} = k\lambda/\beta_{hkl}\cos\theta \quad (3.6)$$

In equation (2.6) k is a shape factor depending on the crystallite shape, (hkl) are the Miller indices of the reflecting planes, β_{hkl} denotes the corrected half-width of the chosen line k depends on the particular definition of β and $D^{(120)}$, a value of 0.9 was used in this work, θ is the Bragg angle of the hkl reflection and λ is the x-ray wavelength which was 1.5418 Å for CuK_{α} .

To calculate the crystallite size of zirconia, a fine powder of Y_5Si_3 was used as a reference material because it has a very good crystalline form and gave lines close to, but not overlapping, those of interest. An x-ray pattern of a mixed powder consisting of reference and the sample was obtained using a Debye-Scherrer camera. For zirconia the (202) line at $2\theta = 50.7^\circ$ was chosen to compare with the $2\theta = 52.23^\circ$ of Y_5Si_3 , which are the nearest lines without overlapping since nearby lines are needed to make geometrical conditions as similar as possible.

A Joyce-Leobel automatic recording microdensitometer, model MK-111CS, was used to measure the peak-intensity. Using Jones⁽¹²⁰⁾ correction curve for the lack of monochromaticity of the x-ray beam and instrumental broadening. Determination of β_{hkl} comes from the graphical representation of the relationship between β/B and b/B , where b is the peak width at half peak maximum for the chosen line of the Y_5Si_3 standard and B is the same parameter for the ZrO_2 sample. The classical calibration curve of Jones is shown in Fig.3.3.

For example, using ZrO_2 precipitated from $\text{Zr}(\text{NO}_3)_4$ at pH 8.5 the line width at half peak intensity, $B = 1.15^\circ(2\theta)$, and that of reference material, $b = 0.502^\circ(2\theta)$. Therefore, $b/B = 0.436$. Interpolating this value from the curve in Fig 3.2 gives the values of β/B , from which β can be calculated.

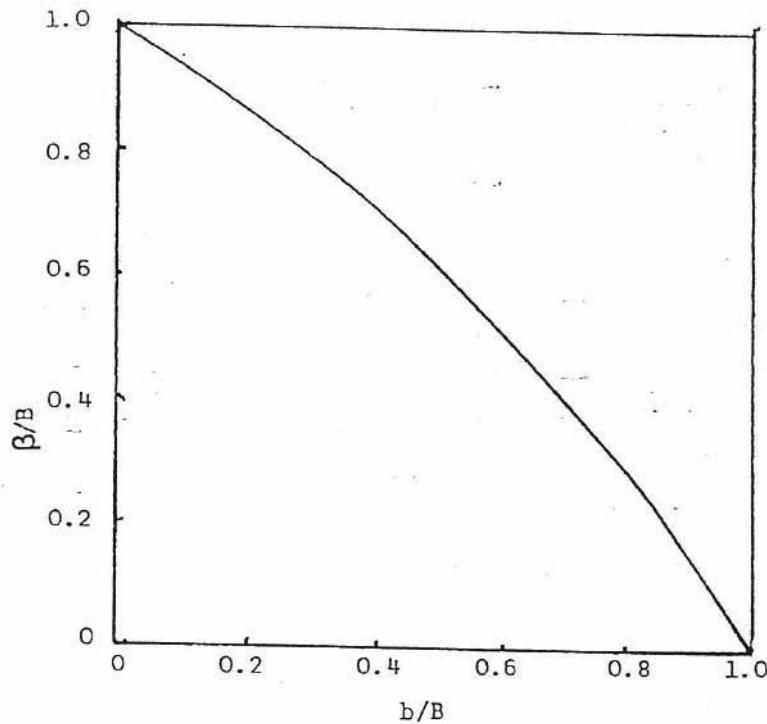


Figure 3.3 Curve for correcting line width of Debye-Scherrer lines for instrumental broadening¹⁸⁸.

3.4.4. Porosity measurement

To measure the apparent porosity, the sample was weighed dry in air (W_d), suspended in boiled water (distilled) to fill the pores (W_b), and weighed in air again with water filling the pores (W_s). The relationship between apparent porosity and the above weights is:

$$\text{Apparent porosity} = 100[W_s - W_d]/[W_s - W_b]$$

3.4.5 Microstructure analysis

The microstructure of the discs of hydrated OPC, OPC-tet-ZrO₂ composites and zirconia powders were studied by scanning electron microscopy, SEM, and by using the Leitz miniload microhardness microscope.

Discs were polished to a mirror finish surface. All polishing was done by a two-step procedure: first a 1 μm diamond paste rubbed into a satin cloth was used for coarse polishing to obtain a flat surface. At this stage line scratches from the 1 μm diamond are visible and 0.05 μm α-alumina slurry poured into a microcloth is used to remove them. Washing with alcohol is needed at every step in the procedure. After the final polish the samples are ultrasonically cleaned and finally rinsed in alcohol before allowing it to dry. The procedure was repeated on both sides of the disc before final mounting on a brass stub.

Because cementitious samples have very high electric insulation capacity and low thermal conductivity, it is desirable to apply a thin layer of a conducting material using a sputtering method. The layer is made as thin as possible within the range 5–50 nm. The choice of coating is optimised for maximum secondary electron production and an 8–10 nm thick layer of gold was found to be excellent in this respect. When X-ray analysis in the SEM was needed a graphite (carbon) coating was applied by the same process on the surface and side of the specimen before insertion into the electron beam.

An approximate measure of the thickness of the coatings was obtained from eqn (3.6):

$$d = mA Kv t k \quad (3.7)$$

In eqn (3.7) mA is milliamps, Kv is the voltage applied, t is discharge time in minutes, k is a constant that is approximately 10 for argon or 4 for nitrogen, and d is the thickness of the film in angstrom units.

Both polished, fractured and powder samples were examined in the microscopes. The machine used was a SUPER-III A ISI. This work was done on the SEM by using the Back Scattered Electron (BSE) and Secondary Electron (SE) techniques, so that a semi-quantitative phase analysis could be obtained. In the electron microscope, back scattered electrons are produced from elastic collisions of the incoming electrons with nuclei of the atoms in the specimen, which means the intensity increases with the atomic number of the specimen, so that areas with a high average atomic number appear bright in the resultant image and areas of low atomic number appear dark.

3.5 Mechanical Properties

3.5.1 Microhardness measurement

These measurements were made on a Leitz miniload hardness apparatus, using both Vickers and Knoop diamond indenters. The load was applied over a period of 15 seconds and then maintained for a further 15 seconds. The

Leitz instrument used here was equipped with a polariser, the use of which enabled the surface feature to be seen without prior etching.

Both the vertical and horizontal diagonals of the indent were measured and the average of the two measurements was related to Vickers hardness as follows:

$$H_v = 1.817 \times 10^{10} P/d^2 \quad (3.8)$$

Where, H_v = Vickers hardness in GN m^{-2} , P is the load in grams and d is indent diagonal length in μm .

The hardness tester allowed the diamond to be changed and so for some estimates of Young's modulus to be made a Knoop diamond was periodically used.

3.5.2 Fracture toughness measured by indentation technique

The aim of this work was to study the feasibility of using the microhardness technique to measure of the toughness, K_{1c} , of cementitious materials. Fractured discs from the Brazil strength test were used for indentation testing. Increasing loads were used on a Vickers pyramid diamond to make an indent until cracked indents were found. After removing the load the dimensions of the indent were measured in the usual way, but as well as the impression diagonal, the length of the cracks emanating from the indent corners were measured. Several indentations were made on the same specimen but no readings were taken if overlapping cracks were observed. When loads greater than 19.6 N were needed indentations were made on

the same specimen but no readings were taken if overlapping cracks were observed. A Vickers microscope Macrohardness Tester No 254221 supplied and calibrated by Denison-Mayes Ltd was used. The shock application of loads in excess of 20 kg sometimes caused samples to shatter.

3.5.3 Young's modulus measurement by the Knoop hardness method

Young's modulus, E , was determined by the Knoop hardness method as described by Martienssen *et al.*⁽¹²¹⁾ Use is made of eqn (3.9):

$$E = 0.45 H_k / (0.1406 - b/a) \quad (3.9) \text{ Check this number}$$

In eqn (3.9) H_k is the Knoop hardness, b = indent short length and a is the indent long length. A load of 0.98N was used to make the indent, an example of which is shown in Fig 3.4.

3.5.4 Tensile strength measurement

A J-J tensile testing machine (T20K) was used to measure the fracture strength (splitting strength) by using a 20 KN load cell in a compression cage and a cross-head speed of 2mm/min. The tests, which were performed at room temperature, were of diametral compression type on the disc specimens prepared as already described. The disc was placed between contoured anvils made of stainless steel. A thin pad of cotton wool was placed between the test disc and the hard loading anvils to accomplish proper load distribution and to avoid surface cracking and non-diametral fracture as far as possible.

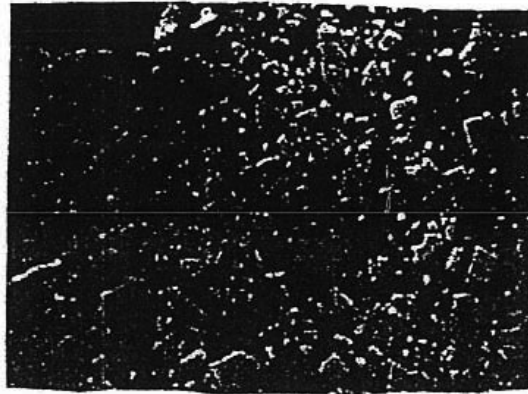


Figure 3.4 BSE micrograph of the surface of a hydrated OPC disc

The fracture strength was calculated by using the following expression:

$$\sigma = 2P/\pi Dt \quad (3.10)$$

Where σ is the fracture strength, P is the applied load, D is the disc diameter and t is the disc thickness.

CHAPTER FOUR

STUDY OF THE AMORPHOUS TO CRYSTALLINE PHASE TRANSITION OF ZIRCONIA

4.1 Introduction

The mechanism of transformation toughening was outlined in Chapter One, the importance of which was mentioned; to obtain a high percentage of the tetragonal form of zirconia in any powder to be used as admixture in the OPC-ZrO₂ composites. Zirconia powders are commonly obtained by thermal decomposition of amorphous hydrated hydroxide precursors. Since powders containing high percentages of metastable tetragonal zirconia were desirable, that would themselves be as sensitive as possible to stress conversion to the monoclinic form, it was decided to examine more fully the amorphous to crystalline transition for pure zirconia and mixed, oxide-zirconia, systems. However, the systems to be examined were chosen so that well stabilised or partially stabilised zirconia was not formed, therefore neither Y, Mg, nor Ca oxides were chosen for this study. As emphasised previously in Chapter One, the vast majority of zirconia research is concentrated on the monoclinic → tetragonal phase change. This is despite the fact that for successful applications involving ZrO₂, reproducible powders must be made from essentially amorphous material and the successful transformation of this powder to the tetragonal form is important. The most notable feature of the formation of crystalline zirconia from hydrous gels, which is the most commonly encountered way of making zirconia powders, is the sharp energy burst that occurs. This has led to it being

variously named: the crystallization burst phenomenon, the exothermic glow peak and the exothermic burst. Samples have been seen to glow white hot on undergoing the transition to a crystalline form. The effect is particularly noted because of the relatively high temperature at which it occurs and the fact that it happens over a very short temperature interval, when compared to similar transitions in other hydrous gel systems. ⁽¹²²⁾ For example, Cr_2O_3 , transform over a wide temperature interval usually beginning and ending at much lower temperatures than those noted for ZrO_2 crystallisation. The visible effect on a DTA thermogram of the transition to a crystalline phase is a sharp, spike-like peak for ZrO_2 and a broad, low temperature hump for other gels.

The crystal structure, and general morphology of ZrO_2 , just after crystallisation has been studied in great detail in the past and a lot has been established about the nature or the mechanism of the transformation to a crystalline form despite the notable differences to other crystallisation processes, such as Al_2O_3 from $\text{Al}(\text{OH})_3 \cdot x\text{H}_2\text{O}$. The purpose of this thesis is to add on to the existing body of knowledge on zirconia.

First some of the more important relevant papers must be reviewed. Gimblett et al. ⁽¹²³⁾, for example, concentrated on the effect of the precipitant on the properties of the amorphous powders, and the effect this has on crystallisation, by examining the exothermic-glow peak using DTA, TG and evolved gas analysis techniques. Their results were interesting when NH_3

gas was the precipitant used by bubbling it through zirconyl chloride, $ZrOCl_2 \cdot 8H_2O$, solution. The main gas evolution at $150^{\circ}C$, consisted of H_2O and NH_3 , and this was followed by a further small evolution of H_2O at $450^{\circ}C$ when the exothermic crystallisation peak occurred on the DTA trace.

A similar study, but one which involved techniques more like those applied here was presented Exter and Winnubst⁽¹²⁴⁾ where the precipitant was kept constant for $ZrOCl_2$ solution, but the effect of varying the solution pH was particularly studied. Reasonably good agreement between the work presented in this thesis and that of Crucean was eventually achieved once the importance of changes in the heating rate on the temperature of the crystallisation process start point was realised. This led to the new work in this thesis on heating rate effects on the process. A comparison of Crucean's data with that presented here does show that a simple crystallite size effect is not satisfactory in explaining the polymorphic form of the eventual product. The crystallite size is only one parameter. Other aspects are:

- (i) Temperature of the transformation,
- (ii) Symmetry of the transformation,
- (iii) Overall heat evolved,

Indeed the literature in this area is now ambiguous as to the role played by particle size in the crystallisation process. For example, boiling $ZrOCl_2$ solution flocculated with NH_4OH produces monoclinic crystalline material with a crystallite size of 5.0 nm,⁽¹²⁵⁾ while the same solution when treated at

room temperature yields a tetragonal phase that has 25 nm crystallites present. This is in contradiction to Scian et al.⁽¹²⁶⁾ who postulated that it is particle size that determined whether tetragonal or monoclinic crystals occur because the specific surface energy of the monoclinic form is greater than the tetragonal form and therefore below a critical size only tetragonal should exist.

Blesa et al.⁽¹²⁷⁾, in a recent study involving ZrOCl_2 solution destabilised by NH_3 solution further demonstrate the ambiguity of crystallite size effects and present a useful hypothetical scheme for the formation of crystals containing tetramers of $(\text{Zr-O})_4$. These structural units have been discerned in crystalline $\text{ZrOCl}_2 \cdot 8\text{H}_2\text{O}$ and are present as $[\text{Zr}_4(\text{OH})_8(\text{H}_2\text{O})_{16}]^{8+}$ ions in solution.

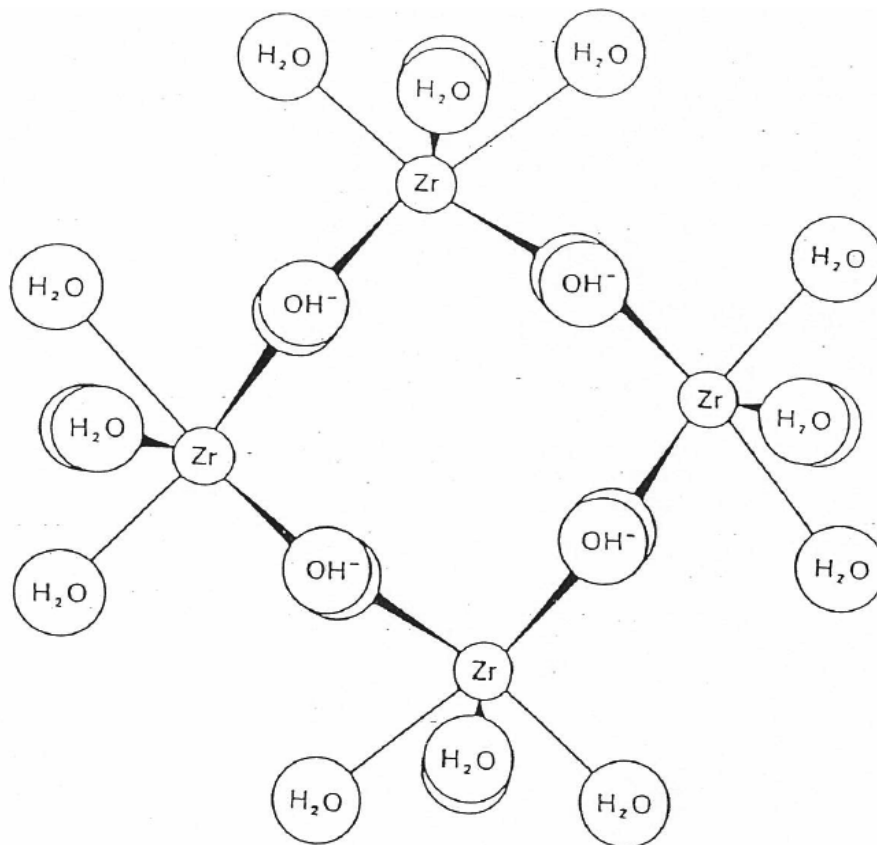
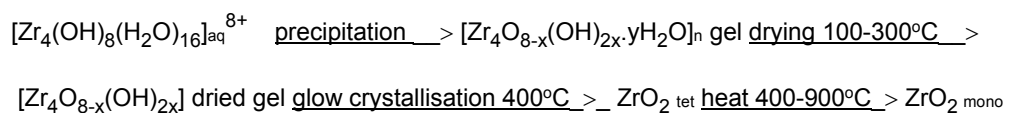


Figure 4.1 Projection on (001) plane of {Zr₄(OH)₈(H₂O)₁₆} tetramer

Figure 4.1 shows this structural unit. This led Blesa to suggest that the dried gel prior to the crystallisation glow phenomenon was also essentially tetrameric. Thus this formed the template for crystallisation of the tetragonal form of ZrO₂ at the exothermic glow temperature.

Blesa scheme is:



4.2 Results

4.2.1 Zirconia made from solutions containing zirconium cations only

(a) $ZrOCl_2$ solution

Figure 4.2 shows the DTA and TG traces of ZrO_2 gel precipitated from $ZrOCl_2 \cdot 8H_2O$ solution at pH 10.4, as described in Chapter 2.

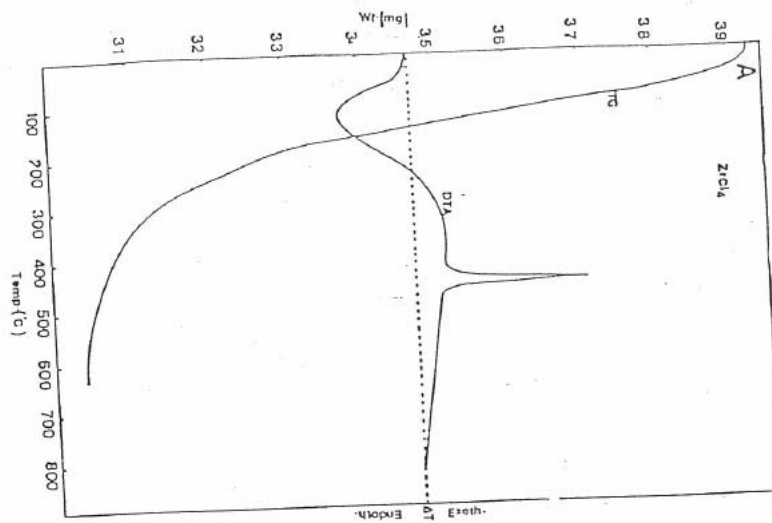


Figure 4.2: DTA traces of typical ZrO_2 gels

There is a typical loss of mass, due to volatilisation of water, of about 10% of the total mass change which corresponds to the broad endothermic peak completed by $120^{\circ}C$ on the DTA. This broad peak is followed by a very sharp exothermic peak at $438^{\circ}C$ corresponding to the formation and crystallisation of a ZrO_2 phase which x-ray analysis showed to be cubic zirconia. An overall 22.9 % loss of weight from room temperature up to

450⁰C is observed. The results in Table 4.1 indicate that cubic ZrO₂ arises from solids precipitated from high pH value solutions.

Table 4.1

Peak temperature, weight losses, and particles sizes of ZrO₂ Precipitated from ZrOCl₂ solution

Precipitation pH	wt loss at exothermic peak temp. %	wt loss between peak temp and 950°C %	Exothermic peak temperature °C	Crystallite size after exothermic event nm	ΔH kJmol ⁻¹
3.7	26.9	3.6	456	13.0	19.7
4.6	20.1	2.2	447	12.5	24.7
5.8	-	-	451	13.2	29.7
7.3	23.2	2.3	454	14.3	27.4
8.5	26.3	0.2	440	11.5	32.6
10.4	22.9	0.4	438	10.0	35.4

The exothermic peak maximum position for these gels shows a decrease from 456 to 438⁰C as the pH of the precursor solution is raised. The exception appears to be the pH 7.3 samples, but if the correlation is with the crystallite sizes and not pH this ceases to be an anomaly because it has a size close to the pH 3.7 samples and a peak maximum temperature almost the same. From this it appears that the temperature of the exothermic peak maximum correlates more closely with the crystallite size of the emergent crystals than with the pH of the solution from which the gel came.

On the other hand the zirconia polymorph is definitely associated with alkalinity or acidity and hydrogen ions do seem to be involved in some way. For example when gel precipitates made at pH 1.4 and 8.5 were washed

with water as normal, followed by a wash with dilute acid solution, before drying, the transformation peak maximum was unchanged in all cases except when sulphuric acid was used on pH 10.4 gel when the exothermic peak maximum was shifted to 510⁰C. Much more noticeable however was the fact that after the acid washes the dried gels always transformed to tetragonal zirconia and not the cubic form. Thus suggesting an important role played by ions adsorbed on the gel surface.

In general, acidic solution precipitates produce larger overall mass losses during the thermal decomposition and in particular show a significantly greater weight loss at, and just after, the crystallization temperature. Acidic solution gels crystallise as tetragonal ZrO₂.

Drying methods do not reflect in the crystallisation peak maximum position and notably a freeze dried powder had a peak maximum at 433⁰C compared to 438⁰C for oven drying for gel made at the same pH. In this case it was noted that the crystallite sizes were very close at 9.7 and 10 nm. This again demonstrates the close correspondence between crystallite size and crystallization peak maximum temperature.

For all the powders made in this work the transformation from tetragonal to the monoclinic structure began at approximately 600⁰C and was complete at 900⁰C depending on solution pH from which the material was made.

Crystallite sizes compare well to those reported by Crucean being in the 10-14 nm range.

(b) Zirconium Nitrate Solution

Tetragonal zirconia was obtained from zirconium nitrate by two different procedures. In the first method, the solid nitrate was directly decomposed in the air at 380⁰C resulting in a crystallite size in the region of 11.2 nm. The second method is the normal solution route using ammonia as the precipitant in acid pH solution. Results for gels obtained from Zr(NO₃)₄ solution are shown in Table 4.2 At any comparable pH the exothermic peak maximum is some 10-20⁰C higher than for gels obtained from oxychloride solutions, indicating some delay in the nucleation process. Once again, as Fig 4.3 shows, this correlates most effectively with the amorphous phase crystallite size, which is in each case greater from the nitrate solution. Excluding the pH 7.3 results obtained using ZrOCl₂, a good correlation between exothermic peak maximum temperature and crystallite size continues to be evident, in that high values of peak maximum correlate with larger crystallites.

Table 4.2

Peak temperature, weight losses, and particles sizes of ZrO₂ Precipitated from Zr(NO₃)₄ solution

Solution pH	Exothermic peak max temp °C	Wt loss up to peak. max %	Final wt loss %	Crystal type after exotherm	ΔH kJmol ⁻¹	Crystallite size nm
3.7	475	18.7	20.7	Tetragonal	19.9	18.4
4.6	457	15.3	16.2	Tetragonal	24.6	15.6
5.8	443	17.0	17.1	Tetragonal	30.9	13.4
7.3	462	22.9	23.5	Tetragonal	29.7	16.3
8.5	456	13.7	13.7	Cubic	24.2	18.6
10.4	458	20.7	20.8	Cubic	25.4	17.0

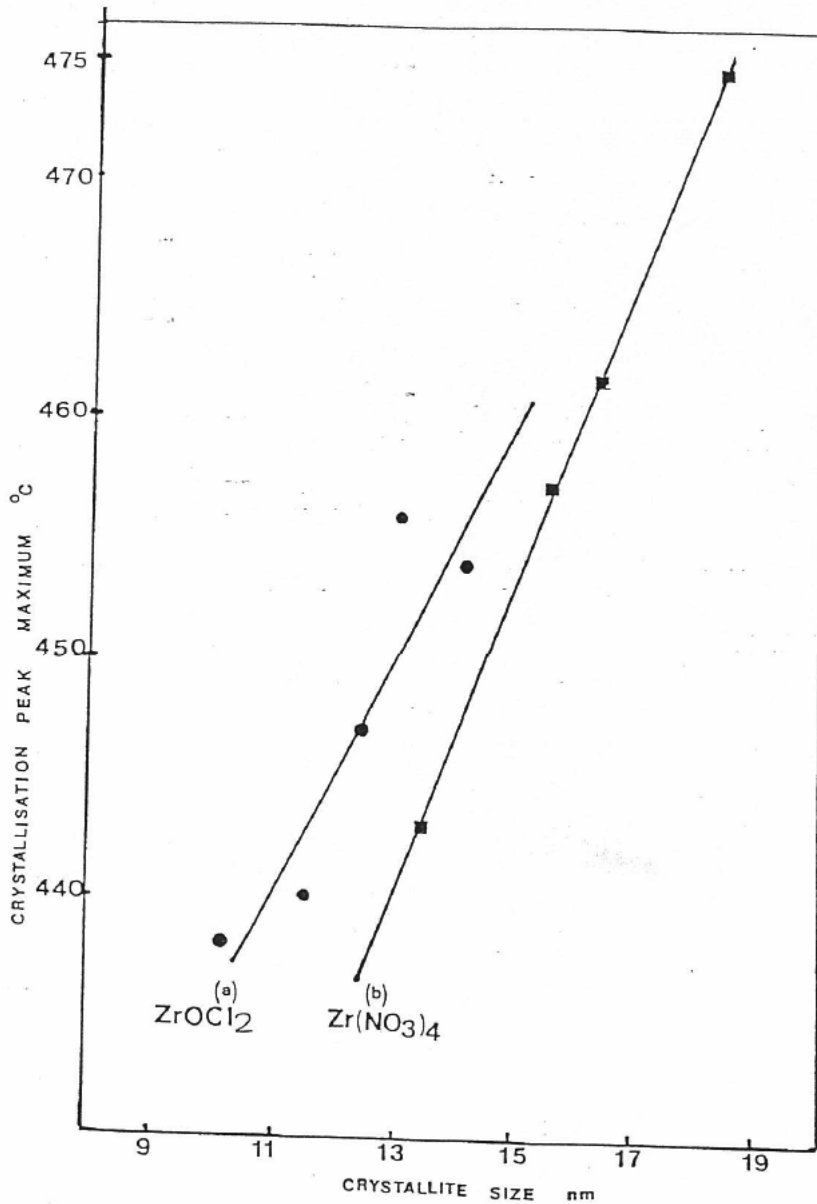


Figure 4.3: Peak max temp v particle size

The enthalpy of transformation data, given in Table 4.1 supports this trend too. The molar enthalpy of transition rises to a maximum for the sample with the smallest crystallite size and the lowest exothermic peak temperature, before rising again for alkaline precipitates. Only for the sample made at pH 5.8 is the crystallite size in the same range as the powders from oxychloride

solutions, otherwise the crystallites are considerably larger than those from oxychloride solutions. Compared to the oxychloride-derived powders, the nitrate-derived powders show smaller weight losses on calcinations at all comparable pH's of preparation, but again significant weight losses after the exothermic peak are generally only associated with acid precipitates.

The acid pH derived powders invariably yield tetragonal ZrO₂ while precipitates from very alkaline solutions lead to the cubic modification. This was also the case for the oxychloride solution gels. This relationship between continuing weight loss after crystallisation, crystal symmetry, and pH is a constant feature for these systems as the data for the mixed-gels shows in Table 4.3. The weight loss during the crystallization process was observed to be sudden. The mixed-gel data also confirm the lower exothermic peak maximum temperatures for acid-derived compared to alkaline-derived powders.

Table 4.3

Thermal analysis data

Composition	pH of formation	Crystallisation exothermic peak max temp °C	ZrO ₂ polymorph after cooling from 950 °C	Mass loss up to 950 °C %
Zr _{0.93} Sn _{0.07} O ₂	3.7	530	tetragonal	27.7
	10.8	461	tetragonal	21.9
Zr _{0.93} Fe _{0.07} O _{1.965}	4.6	495	tetragonal	25.4
	9.9	466	cubic	20.4

From the micrograph shown in Figure 4.4 it can be seen that the tetragonal ZrO₂ shows aggregates of small round particles. Aggregation is quite severe because a laser particle size analysis gives a mean size around 4µm

compared to 20 nm for crystallite size measurement. Figure 4.3 shows relationship between peak maximum temperature versus particle size.

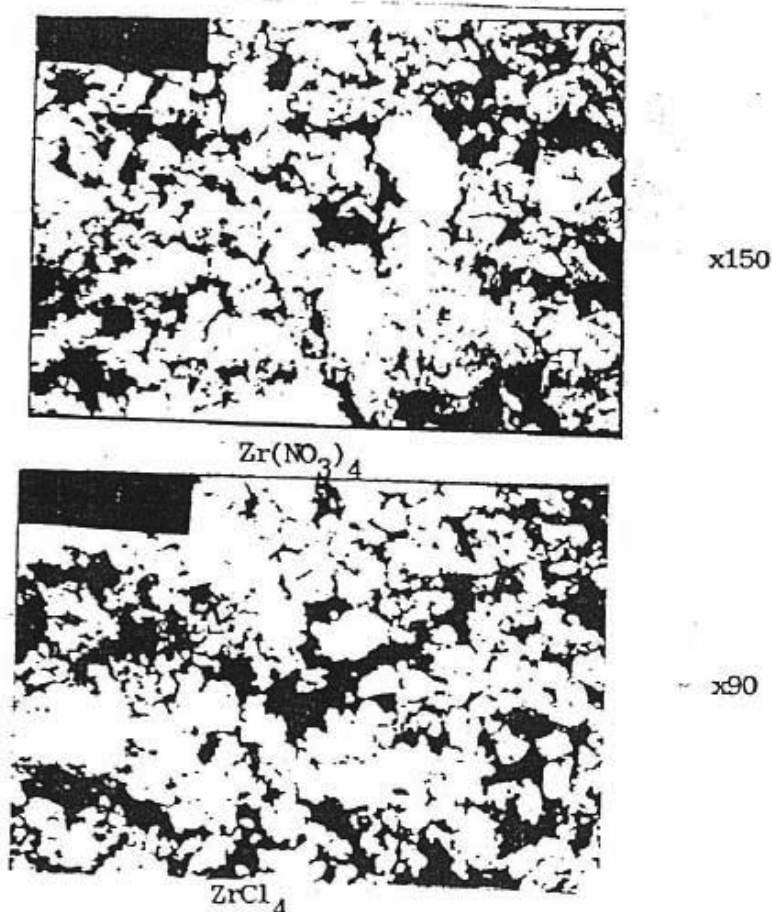


Figure 4.4: SEM micrographs of zirconia powders

(c) Zirconium Tetrachloride ($ZrCl_4$)

One high pH gel precipitated from $ZrCl_4$ solution showed similar behaviour to the other gels, as the DTA and TG curve show in Fig 4.2. A broad hump with a peak maximum, denoting initial loss of water, occurred at $117^{\circ}C$ and this

was followed by a moderately strong, very sharp, exothermic crystallisation peak at 431⁰C, by which time the overall weight loss was 22%.

In order to compare this powder with the zirconium oxychloride gels, it was heated to 450⁰C and then x-rayed, which showed it to be tetragonal but with a smaller unit cell volume than the tetragonal ZrO₂ arising from oxychloride gel i.e. 0.1335 nm³ compared to 0.1347 nm³. Further x-ray analysis using the Debye-Scherrer camera revealed a relatively large crystallite size, around 21 nm, and as shown in Fig 4.4 the solid is an agglomerate or aggregate of round crystallites.

Transformation from tetragonal to monoclinic form started at 550⁰C and continued until 900⁰C when the sample becomes fully monoclinic.

(d) Acid sol of zirconium silicate

A sol of ZrSiO₄ coagulated with excess ammonia added rapidly with no attempt to control the pH, when filtered and dried, gave a hard, glassy gel. The DTA and TG traces are shown in Fig 4.2. A mass loss beginning at 90⁰C is indicated and a severely delayed exothermic crystallisation peak, which was very small and uncharacteristically broad, is indicated at 633⁰C. The crystal symmetry of the ZrO₂ was cubic as the x-ray films in Fig 4.6 show. This symmetry reflects the overall alkaline conditions of the preparation. The overall mass loss was 23.4%. The lattice parameter of the

cubic phase was $a = 0.509$ nm for a sample heated to 633°C and $a = 0.5083$ nm for a sample heated to 800°C .

Eventually when heated for some time at 1200°C the crystal symmetry became tetragonal with lattice parameters of $a = 0.506$ nm, and $c = 0.519$ nm. Of all the Table 4.3: Thermal analysis data for some precipitated mixed ion gels made these had the smallest crystallite size at 9.3 nm. This is after the transformation at 633°C when it must be remembered all other samples would have crystallite sizes in excess of 18 nm.

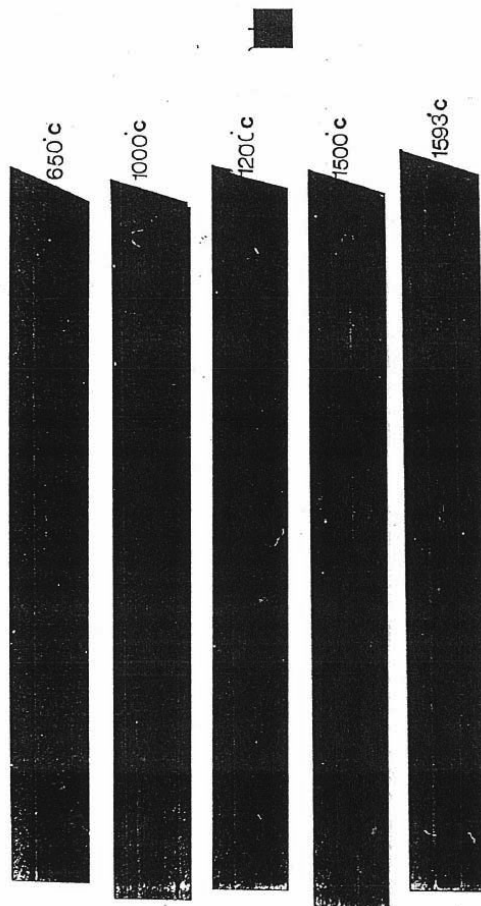


Figure 4.5: X-ray films for the product from ZrSiO_4

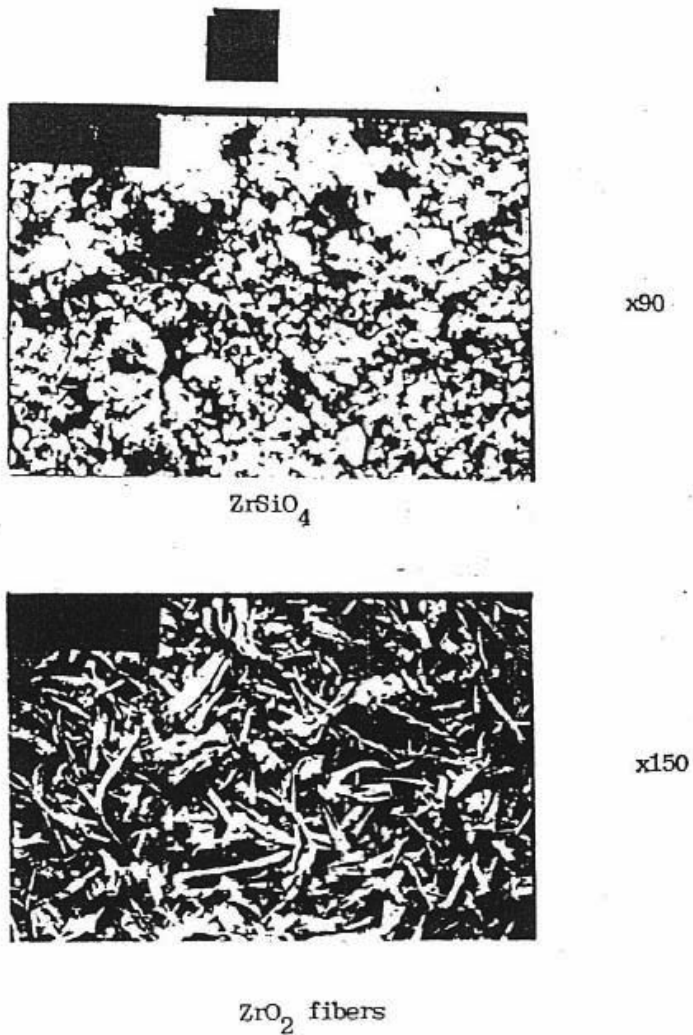


Figure 4.6: SEM micrographs of zirconia

The preparation did give zirconia with the small crystallite size as reported, but should also have a dispersed silica gel prepared simultaneously in the mixture. However as Fig 4.5 shows even when heated to $1200^{\circ}C$, no x-ray evidence could be found for the existence of any crystalline silica phase. An SEM picture is shown of a powder that was also examined by the EDX technique for Si and Zr content. The results given in Table 4.4 show the

powder has approximately equiatomic percentages of Si and Zr. Thus the powder must contain an amorphous form of SiO₂, since the x-ray film showed only cubic or tetragonal ZrO₂ lines.

Table 4.4

Data on the products arising from fired sol made from acidic zirconium silicate.

Temperature °C	Si at%	Zr at%	X-ray phase analysis
650	40.5	59.5	Cubic ZrO ₂
800	46.5	53.5	Cubic ZrO ₂
1000	44.4	55.6	Tetragonal ZrO ₂
1200	48.6	51.4	Tetragonal ZrO ₂
1400	-	-	Tetragonal ZrO ₂ plus monoclinic ZrO ₂
1500	49.2	50.8	Tetragonal ZrO ₂ plus monoclinic ZrO ₂ plus β-SiO ₂ plus ZrSiO ₄
1600	49.4	50.6	ZrSiO ₄

The presence of the SiO₂ clearly has a big influence on the crystallisation temperature and the phases that become apparent when the gel is calcined: at 1400 °C monoclinic ZrO₂, is detected and at 1500 °C a mixture of tetragonal ZrO₂, plus monoclinic ZrO₂ or high cristobalite and zircon, ZrSiO₄, it is difficult to decide. Then as expected by 1600°C the material recombines to form zircon, ZrSiO₄. A second experiment involved an acidic zirconium silicate sol prepared by thermal hydrolysis at 150 °C. This produced a powder that gave an exothermic crystallization peak at 440 °C and an x-ray diffraction pattern for tetragonal ZrO₂ with a = 0.509 nm, c = 0.517 nm. The crystallite size of this material was 12.9 nm.

Thus both acid and alkaline conditions produce zirconia modifications that are in agreement with the results from the three other solutions tested. The unusual stability of the alkaline-prepared cubic phase was probably caused by the dilution or surface effect of the amorphous silica. The data in Table 4.5 support a dilution theory because the small crystallite size of 9.3 nm showed an enthalpy change of only 15.2 kJ mol⁻¹ when as the earlier data show, small crystallite size products have increased enthalpy of crystallisation values. The ΔH of crystallization was calculated assuming pure ZrO₂. If the sol was basically ZrSiO₄ i.e. ZrO₂ plus SiO₂ then the ΔH value would be approximately 30 kJ mol⁻¹, which is nearer to that predicted from the data contained in Table 4.3. If nothing else, at this stage these results indicate the importance of examining several mixed gel system because of the effect that co-gel can have on the properties of the ZrO₂ nanopowder that is produced.

Table 4.5

Data on preparations made from pH 10.4 solutions

Solution	Exothermic crystallisation Temperature °C	Mass loss at crystallisation temperature wt%	ΔH_{cryst} kJ mol⁻¹	Crystallite size nm
Zr(NO ₃) ₄	458	20.7	17.0	25.4
ZrOCl ₂	438	22.9	10.0	35.4
ZrCl ₄	431	20.9	20.9	23.4
ZrSiO ₄	633	20.7	15.2	9.3

4.2.2. Zirconia from solutions containing tin and iron cations

The combined effect of precipitate pH and the presence of a second gel phase, on the characteristics of the zirconia is already evident in the result so far presented for the zirconium silicate solutions.

The characteristics of the thermograms observed in this work show in general that as the pH increases the exothermic peak maximum temperature for zirconia crystallisation, moves to lower values but at any particular pH in a mixed system when compared to the pure zirconia case, there is a marked increase in the temperature at which the exothermic event occurs. Although, crystal size impacts thermograms extensively, minor effects may also result from fluctuations of pH levels. This makes it easier to prepare cubic or tetragonal forms of zirconia but may produce metastable zirconia that is more difficult to transform by the stress field ahead of a crack and so prevent phase transformation toughening. In order to assist this form of toughening the effect of co-precipitated tin and iron gels was examined.

4.2.2.1 Zirconia made from solutions containing Fe³⁺ ions.

Concentration and temperature dependent colour changes were observed and this, along with evidence from the SEM of sample conductivity, was an indication of solid solution formation in these mixed-gels and their calcined products.

Some results are contained in Table 4.6 and Fig 4.7, which show some broad general features. First the exothermic peak maximum temperature is

raised in the presence of the $\text{Fe}(\text{OH})_3$ gel, for example when the Fe^{3+} concentration is kept constant at 7% and the pH of gel formation from $\text{Zr}(\text{NO}_3)_4$ solution is varied, the crystallization event is delayed by some 50°C for acid precipitates as can be seen by comparing the results in Table 3.8 with those for pure ZrO_2 in Table 4.2.

Table 4.6

Effect of Fe^{3+} concentration on the crystallisation of ZrO_2 gel made at pH 8.5 from ZrOCl_2 solution

Fe^{3+} %	Crystallisation peak Max $^\circ\text{C}$	Mass loss %	Crystal type at 600°C	Crystal type at 900°C	Crystal type at 1200°C
1	469	-	Cubic	-	-
3	488	-	Cubic	monoclinic	monoclinic
4	486	25	Cubic	monoclinic	monoclinic
5	488	25	-	-	monoclinic + Fe_2O_3
7	510	24.9	cubic $\Delta\text{H}=26.7$ kJmol^{-1}	tetragonal + monoclinic	monoclinic + Fe_2O_3
10	521	24.9	Cubic	monoclinic	monoclinic + Fe_2O_3
15	557	19.8	Cubic	monoclinic	monoclinic + Fe_2O_3
20	570	24.8	Cubic	monoclinic	-
24	607	-	-	-	monoclinic + Fe_2O_3
50	674	24.7	Cubic	tetragonal + Fe_2O_3	monoclinic + Fe_2O_3
70	718	-	Cubic	tetragonal+ monoclinic+ Fe_2O_3	-
100	363, 422	24.1	$\Delta\text{H}=63.5$ kJmol^{-1}	-	-

The effect is much less marked for alkaline solutions being only an 8-15 $^\circ\text{C}$ increase compared to pure zirconia.

Secondly the dilution effect on the crystallization process is evident in the results shown in Table 4.6 where precipitation pH was maintained at 8.5 but

increasing volumes of FeCl_3 solution were added to a ZrOCl_2 solution. Graphically the effect of the co-precipitation on the crystallization process is shown in Fig 4.7 where it can be seen that $\text{Fe}(\text{OH})_3$ has a bigger effect than $\text{Sn}(\text{OH})_2$ and overall the effect is much greater than that expected from the crystallite size considering the size changes shown in Table 4.7.

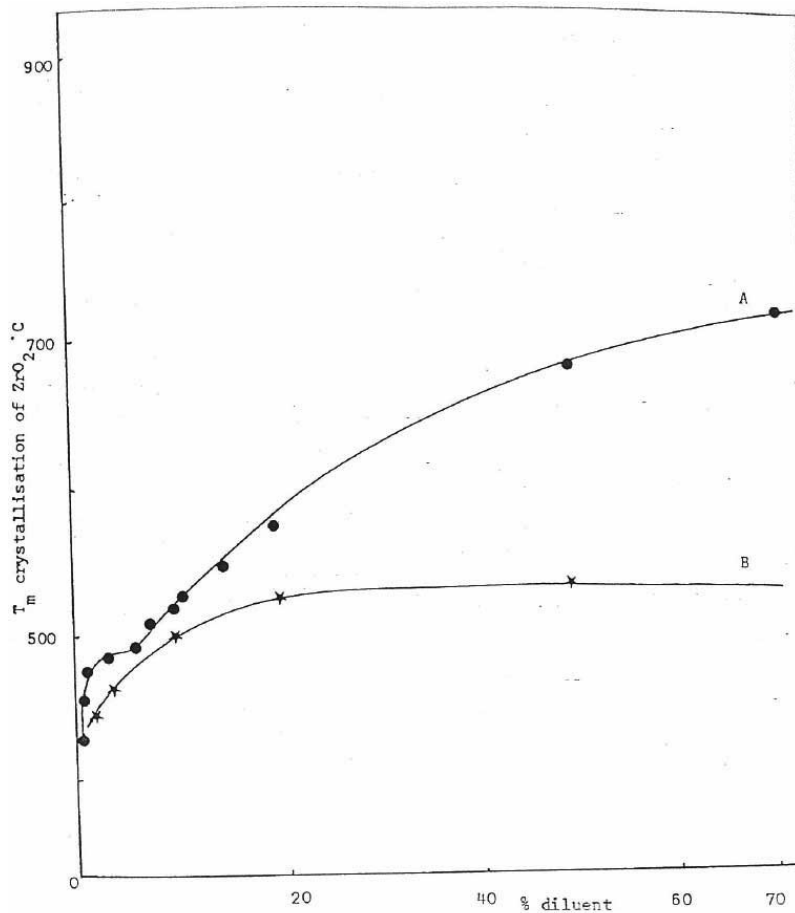


Figure 4.7: Relationship between crystallisation temperature of zirconia and % of (a) Fe_2O_3 and (b) SnO_2 present

A general analysis of the ZrO_2 crystallisation data is given in the discussion Chapter 7, where an equation relating peak maximum temperature in the DTA experiment to crystallite size is developed as equation (7.2).

Table 4.7

DTA results for crystallisation peak maximum temperature obtained at 10^0C min^{-1} heating rate for powders obtained from $\text{Zr}(\text{NO}_3)_4$ solutions containing 7% $\text{Fe}(\text{NO}_3)_3$

Precipitation pH	Crystallisation peak temperature $^{\circ}\text{C}$	Mass loss at peak temperature %	Mass loss at 900°C %
3.5	526	23.3	23.8
4.8	495	20.4	21.1
6.7	496	19.7	19.7
8.0	491	18.2	19.9
9.9	486	18.4	18.4

Using equation 6.2 with the crystallite sizes in Table 4.8 gives the experimentally observed range of $400\text{-}700^0\text{C}$.

Table 4.8

Effect of Fe^{3+} ions on the crystallite size of ZrO_2

Fe^{3+} content %	Crystallite size nm
3	12.4
4	10.4
5	14.3
6	20.6
7	17.3

Thus the fact that co-precipitation does strongly influence the crystallite size range is interesting in that it is the same effect as that found for pure ZrO_2 made from oxychloride solution. This is in contrast to the much smaller size of the crystallites measured for the tin ion case and in the coprecipitation of zirconium silicate sol with ammonia. This will be considered more fully in Chapter 6 when solubility data is considered and offered as an explanation of these observations.

Some evidence for a change in behaviour between 4 and 7 wt% Fe_2O_3 can be seen in the curve shown in Fig 4.7 which may be associated with the extent of solid solution that can be achieved. The precipitated and dried powders in the 4-7 wt% composition range are pale-brown in colour, remaining so when heated to 600°C , but when heated to 950°C the colour changes to a purple-brown and on further heating to 1250°C the zirconia transformed to the monoclinic structure and lines from $\alpha\text{-Fe}_2\text{O}_3$ were weakly visible in the x-ray powder pattern.

Table 4.6 shows that beyond 5–7 wt%, $\alpha\text{-Fe}_2\text{O}_3$ was always found after heating to 1200°C and also that at 600°C the symmetry of the ZrO_2 phase was, like the pure ZrO_2 case, pH dependent. Cubic lattice parameters change in such a way as to suggest that about 7% is the critical dilution with respect to solid solution formation at the gel-hydrate stage.

Fig 4.7 shows the effect of Fe^{3+} content on maximum peak temperature of monoclinic zirconia when the mixtures are heated to 1200°C . The effect is a very small decrease of about 1.5%. This behaviour reflects a reaction between Fe_2O_3 and ZrO_2 at 1200°C that becomes more apparent as there are more interfaces for reaction to occur. The sharper drop of about 0.5% up to 10% Fe_2O_3 reflects the fact that solid solution at the co-precipitate stage occurs at the most in the range 7-10% as confirmed by the presence of Fe_2O_3 for all preparations above this level. At 1200°C the surface reaction

between the two oxides is responsible for a further very small increase in solid solution formation that can apparently be quenched.

4.2.2.2 Zirconia made from solutions containing Sn^{2+} ions

All gels and precipitates were transparent or white and the effect of tin hydroxide on the zirconia crystallization temperature was less evident than that of $\text{Fe}(\text{OH})_3$ as Fig 4.7 shows. The presence of tin ions, and tin hydroxide precipitates, at all the concentrations and pH's studied, is to make the crystallization reaction yield only tetragonal ZrO_2 as the results in Table 4.10 show. A white \rightarrow yellow \rightarrow red transition at elevated temperature for mixed precipitates containing more than 10 wt% Sn^{2+} indicates the presence of SnO_2 in the mixture and x-ray analysis confirms this for compositions about 20%. The tetragonal modification was the preferred form even though the mass losses varied from 24–17% for pH's in the range 3.7–10.8, as shown in Table 4.11. Unit cell volume changes for monoclinic zirconia obtained by heating the mixed oxide to 1200°C were negligible being well within the experimental error.

Table 4.9 shows the effect of $\text{Sn}(\text{OH})_2$ co-precipitate on the crystallite size and it is notable that the sizes are much smaller, being in range 7–9 nm.

Table 4.9Effect of Sn²⁺ concentration on the crystallite size of ZrO₂

Sn ²⁺ Wt %	Crystallite size nm
3	7.5
5	8.0
8	9.3
10	9.7
15	8.7

Table 4.10

Thermal analysis and x-ray data for mixed zirconia-tin oxide gels

Tin oxide Mol %	Crystallisation peak Temperature °C	Mass loss %	Crystal symmetry after heating to crystallisation temperature	Crystal symmetry after heating to 900°C
5	484	28.0	tetragonal	monoclinic
10	499	24.3	tetragonal	monoclinic
20	526	22.2	tetragonal	monoclinic
50	529	23.3	tetragonal	monoclinic
100	305, 383	24.9	tetragonal	tetragonal

Table 4.11

Crystallisation peak maximum temperature and mass loss data for a heating rate of 100C min⁻¹ for gel made from Zr(NO₃)₄ solution containing 7 mol % SnO₂ at made at different pH values

pH	Crystallisation temperature °C	Mass loss at crystallisation %	Mass loss at 900 °C %
3.7	530	24.4	24.7
5.0	536	23.6	23.8
7.6	481	17.0	18.1
9.0	462	17.6	18.4
10.2	462	16.6	15.1

They are thus like those prepared from ZrSiO₄ sol. For this size range according to equation (7.2) the crystallization peak maximum would be

expected to be about 488⁰C, but as Fig 4.7 shows, it is well above this value, which again reflects the effect of diluent oxide as well as some solid-solution effect. The enthalpy of crystallization is seen to increase as the Sn²⁺ concentration in solution was raised from 3–10 wt%. Fig 4.6 shows this to be a linear increase that does not correspond to the way that the crystallite size changes.

4.2.3. Activation Energy of Zirconia Crystallisation as Evaluated from DTA Experiments

DTA has been extensively used here to investigate and identify the endothermic and/or exothermic reactions that occur as zirconia is prepared from gels. Normally this is done in a qualitative way but it can be used more quantitatively to estimate heat changes as long as standardised procedures and calibration standards are used.

It was noted in the earlier stages of this work that, agreement with reports about the temperatures of peak maxima for reactions like the zirconia glow effect, were not good. Consideration of the literature suggested that a variable may be the heating rate at which experiments were performed. All the DTA investigations done on Zr(OH)₄.xH₂O gels or the gels doped with Fe(OH)₃.xH₂O and Sn(OH)₂.xH₂O, which have so far been reported in this chapter, used a constant heating rate of 0.167 K sec⁻¹ (10⁰C min⁻¹). However when experiments were done on the powders at different heating rates it immediately produced interesting data: changes in the DTA peak

maxima were readily observed. This was indicative of an activated process that must follow a form of the Arrhenius equation:

$$K = K_0 \exp(-E/RT) \quad (4.1)$$

This fact can be used to probe activation energies and to draw possible conclusions as to the mechanism of nucleation of a transformation.

In general it is assumed that the reaction proceeds according to an equation that is of the form:

$$dx/dt = f(x, T) \quad (4.2)$$

Where dx/dt is the rate of reaction and $f(x, T)$ is a function of the amount reacted, x , and T is the absolute temperature at a time t .

Kissinger ⁽¹²¹⁾ developed a theoretical treatment using a model involving transformation of crystalline solid A to crystalline solid B with evolution of gas from decomposition. This of course only partly describes the change of $Zr(OH)_4 \cdot xH_2O$ to ZrO_2 , because a decomposition is involved at lower temperatures to yield an amorphous solid and then there is an amorphous to crystalline transition at the exothermic glow peak temperature that we wished to study.

Kissinger's equation is:-

$$\phi = A(1-x)^n e^{-E/RT} \quad (4.3)$$

Where A is a constant, x is the fraction of sample reacted, n is the order of reaction, E is the activated energy, T is the absolute temperature and R is

the gas constant. In a reaction of the type considered by Kissinger, several mechanisms have been suggested, each characterised by the exponent n and in order to evolve any form of practical equation for comparison purposes n must be assumed to be constant over a period during which more than 70% of the transformation takes place. In eqn (4.3) ϕ , the rate of reaction, rises to a maximum value as T is rising during the athermal heating process and then falls back to zero as the reaction is exhausted. Thus the maximum reaction rate occurs when $d\phi/dt = 0$. By setting the heating rate, α , to be a constant, then eqn.(4.3) can be seen to have the variables of fraction un-reacted, and temperature which changes in the athermal experiment as the function:

$$T = T_0 + dT/dt = T_0 + \alpha$$

Equation (4.3) can be differentiated by parts before setting $d\phi/dt = 0$ at the maximum rate and simplification leads to Eqn (4.4):

$$d\phi/dt = \phi[(E\alpha/RT_m^2) - nA(1-x)^{n-1} \exp(-E/RT_m)] \quad (4.4)$$

In equation (3.4) the subscript m denotes that the maximum rate of reaction occurs at T_m and can be found by setting eqn (3.4) to zero. When the maximum rate is occurring at T_m the material left untransformed is given by $(1-x)_m$ which is not readily determined in the experimental arrangement for DTA. T_m is taken as the temperature of the DTA trace peak maximum. This leads to eqn (4.5):

$$E\alpha/RT_m^2 = An(1-x)_m^{n-1} \exp(-E/RT_m) \quad (4.5)$$

The activation energy, E, is the variable in the systems of interest but cannot be extracted from eqn (4.5) because $(1-x)_m^{n-1}$ is unavailable. This problem was addressed by Murray and White⁽¹²⁹⁾ who showed that the original, eqn (4.3), can, with difficulty, be integrated by successive integration by parts to give the result:

$$1/n-1 (1/(1-x)^{n-1} - 1) = (ART_m^2/E\alpha) \exp(-E/RT)(1-(2RT/E)) \quad (4.6)$$

At the peak maximum temperature on the DTA trace T_m , eqn (4.6) becomes:

$$1/n-1 (1/(1-x)_m^{n-1} - 1) = (ART_m^2/E\alpha) \exp(-E/RT_m)(1-2RT_m/E) \quad (4.7)$$

Using eqn (4.3) a value of e^{-E/RT_m} can be found to substitute in the above equation:

$$\exp(-E/RT_m) = E\alpha/RT_m^2 A n (1-x)_m^{n-1}$$

and substituting this into equation (4.6) gives:

$$1/n-1 [1/(1-x)_m^{n-1} - 1] = 1/n (1-x)_m^{n-1} [1 - 2RT_m/E]$$

which becomes:

$$n(1-x)_m^{n-1} = 1 + (n-1) 2RT_m/E \quad (4.8)$$

Substituting this value into eqn (4.3) it can be rearranged so that:

$$\alpha/T_m^2 = (2R^2AT_m/E^2)[1+(n-1)]\exp(-E/RT_m)$$

and now expressing this logarithmically:

$$\ln\alpha/T_m^2 = \ln K - E/RT_m \quad (4.9)$$

Where $K = (2R^2AT_m/E^2)[1+(n-1)]$

This is now known as the Kissinger equation and indicates that a linear plot will be obtained for $\ln\alpha/T_m^2 \text{ v } 1/T_m$ for reactions involving decomposition follow a mechanism in which the order of reaction lies between 0 and 1.

This equation was used to test the ZrO_2 crystallization peak maximum temperature as a function of heating rate for a series of samples. The slopes of the lines were used to calculate the activation energies and these are listed in Table 4.12. As the figures show reasonable straight-line plots were obtained. However the activation energies are not very comparable to those quoted in Kissinger early work for the decomposition of magnesite, calcite and brucite; the E values in Table 4.12 are considerably higher than those obtained by Kissinger. However the activation energies are of the order that might be taken to support the decomposition-crystallization scheme ⁽¹²⁰⁾ and outlined in the introduction.

Table 4.12

Activation Energies for the decomposition-crystallisation process for different samples of zirconia as found using different model equations

Gel Sample	Preparation pH	Activation Energy from eqn (3.9) kJ (mol)^{-1}	Activation Energy from eqn (3.11) kJ (mol)^{-1}	n^*	m^*
ZrO_2	9.3	172.5	-	1	1
ZrO_2	7.3	173.6	184	1	1
ZrO_2	7.3	557	-	3	1
ZrO_2	7.3	278.5	-	3	2
ZrO_2	7.3	185.7	-	3	3
ZrO_2	7.3	363.8	-	2	1
ZrO_2 gel	7.3	181.9	191	2	2
ZrO_2	7.3	121.3	127.3	2	3
ZrO_2	4.6	215.5	231	1	1
$\text{Zr}_{1.97}\text{Sn}_{0.03}\text{O}_2$	9.9	163.4	-	1	1
$\text{Zr}_{1.95}\text{Sn}_{0.05}\text{O}_2$	9.9	173.2	-	1	1
$\text{Zr}_{1.90}\text{Sn}_{0.10}\text{O}_2$	9.9	199.5	-	1	1
$\text{Zr}_{1.96}\text{Fe}_{0.04}\text{O}_2$	9.9	268	293.4	1	1
$\text{Zr}_{1.93}\text{Fe}_{0.07}\text{O}_2$	9.9	194	-	1	1
$\text{Zr}_{1.93}\text{Fe}_{0.07}\text{O}_2$	4.8	172.5	-	1	1

* n and m are model constants that define a reaction mechanism (see text)

It is difficult to see any very obvious trend in the data shown in Table 4.12 with the exception that increasing the SnO₂ content at constant pH moves the activation energy steadily to higher values, thus suggesting that decomposition-crystallization becomes more difficult to achieve in the presence of increasing amount of SnO₂. There is a linear relationship between tin content and activation energy. On the other hand, increasing the Fe₂O₃ content at constant pH decreases the activation energy.

As they stand these two observations are in accord with what might be expected if the zirconia is essentially precipitated ahead of the Sn(OH)₂ and the tin oxide coats the ZrO₂ surface whilst the Fe(OH)₃ precipitates first and forms the core on which Zr(OH)₄ is precipitated.

The effect of changing the pH of precipitation at constant Fe₂O₃ content is to change the mechanism of the crystallization to give either tetragonal or cubic ZrO₂ and this is reflected in the activation energies. Pure zirconia itself produces cubic ZrO₂ emerging from the lower activation energy process involving alkaline pH gels. This work has been encouraging in that activation energies were found but the basis of the equations used is for endothermic decomposition of hydroxides and carbonates ⁽¹²⁸⁾. Here we have used the analysis to examine very sharp exothermic peaks by assuming that within this reaction a decomposition of [Zr₄O_{8-x}(OH)_{2x}] gel structural units is

occurring, which helps to confirm a decomposition mechanism involving species in the gel like the one suggested by Bleza.

This in the main precludes us from using the DTA curve profile analysis ⁽¹²⁸⁾ for broad endothermic DTA-peaks, to measure the reaction order.

Partial success in this area of work suggested that perhaps a more appropriate thermal curve analysis should be sought. The work of Hayward *et al.* ⁽¹³⁰⁾, whilst being much more recent, also deals with nucleation and crystallization of amorphous glass-ceramics and may therefore be more appropriate. In the Hayward paper, and other related work, the surface free energy of finely-powdered samples is noted as being a significant part of the total free energy needed.

to initiate crystal growth if it occurs on a surface. This would be an explanation of the DTA peak maximum shift to lower temperature as the crystallite size decreases and which we have demonstrated in Section 4.2. As the crystallite size increases surface free energy becomes less important and other mechanism of crystal initiation can be dominant. Thus analysis related to various mechanisms might be of interest. Matusita⁽¹³¹⁾ has shown for non-isothermal crystallization, peak maxima can be related to heating rate through Eqn (4.10):

$$\ln\alpha = (mE/nRT) - 1/n \ln[-\ln(1-x)] + \text{constant} \quad (4.10)$$

where n and m are constants indicative of the nucleation mechanism and all other symbols are as stated earlier in this section.

Assuming that at T_{\max} the percentage of crystallization is the same whatever value for T_{\max} this reduces to:

$$\ln \alpha = (mE/nRT) + \text{Constant} \quad (4.11)$$

From a paper by Ozawa ⁽¹³²⁾ concerning the crystallization of glasses relevant values of n and m are:

- (a) $n = 1, m = 1$, for surface nucleation.
- (b) $n = 3, m = 3$, for bulk nucleation with a constant number of nuclei and 3-D growth.
- (c) $n = 4, m = 3$, for bulk nucleation with a variable number of nuclei and 3-D growth.

Hence comparison of activation energies, for these values of n and m in eqn (4.11), might afford detection of mechanism (a) compared to (b) and (c) if the data from the Kissinger route are used. Further consideration by Matsusita led to an equation related to eqn (4.11):

$$\ln(\alpha^n/T_m^2) = (mE/RT_m) + \text{Constant} \quad (4.12)$$

Eqn (4.12) can be used by assuming a value for n , the constant related to the nucleation mechanism, and the m values can be tested in terms of “reasonable” value for activation energy as compared to that derived from the Kissinger equation, which did produce good linear plots. The acid powder, pH 4.6, is a good straight line with a slope that leads to the

activation energies shown in Table 4.14 for various n and m combinations.

The value for $n = 1, m = 1$, that is surface nucleation, is the closest to the Kissinger equation values.

The near neutral powder, pH 7.3, produced data that gave possibly a slight curve when eqn (4.11) was used. However, any deviation from linearity was only slight. Taking the best line as shown, the activation energies were calculated to be those given in Table 4.13.

Table 4.13

Activation energies for gel crystallisation calculated from the Ozawa equation⁽¹³²⁾

Sample gel	pH	Activation Energy kJ (mol) ⁻¹	Equation constant n	Equation constant n	Notes
ZrO ₂	4.6	231	1	1	Implies surface nucleation
ZrO ₂	4.6	462	2	1	Implies bulk nucleation and 1-D growth
ZrO ₂	4.6	346	3	2	Implies bulk nucleation and 2-D growth
ZrO ₂	4.6	308	4	3	Implies bulk nucleation and 3-D growth
ZrO ₂	7.3	184	1	1	
Zr _{1.95} Sn _{0.05} O ₂	9.9	268	1	1	Tetragonal

Table 4.14

Activation energies calculated for crystallisation of pure ZrO₂ gel using the Matusita equation (4.12)

Gel pH	n	m	Activation Energy kJ mol ⁻¹	Zirconia symmetry
4.6	1	1	215.5	Tetragonal
	2	1	449.4	Tetragonal
	3	1	461.9	Tetragonal
9.3	1	1	172.5	Cubic
	2	1	358.4	Cubic
	3	1	399.0	Cubic

Using the same equation for the alkaline pH 10.8, $\text{ZrO}_2 + 7\% \text{Sn}^{2+}$ co-precipitate, a very good linear relationship was obtained in Fig 4.7. The activation energy values are closest to the Kissinger equation again when $n = 1$, $m = 1$, but this time the agreement is not so good.

An alkaline co-precipitate, pH 9.9, with 4% $\text{Fe}(\text{OH})_3$ does give a curve rather than a straight line plot. Taking an average straight line the activation energies are tabulated and the value of 293 kJmol^{-1} for the $n = 1$, $m = 1$ case is in good agreement with the 268 kJmol^{-1} obtained from the Kissinger equation.

In typical plots, good lines are obtained when the product crystals are produced from acid gels, that is ZrO_2 with pH 4.6 and $\text{ZrO}_2 + 7\% \text{SnO}_2$, whilst the near neutral ZrO_2 gel causes some curvature, and the cubic iron co-precipitated material leads to a definite curve. Greater mass losses at crystallization are associated with acidic powders that yield tetragonal crystals and this may be a factor. So far the best E value agreements have been obtained when $n = 1$, $m = 1$ but of course this is true for $n = 2$, $m = 2$, and $n = 3$, $m = 3$, which precludes any conclusion about surface or bulk mechanisms. Consequently, the data was re-evaluated using eqn (4.12) by Matsusita with $n = 1$, $n = 2$ and $n = 3$ in an attempt to determine the most probable value of n . Activation energies are shown in Table 4.14.

From Table 4.14 it is clear that the process leading to cubic ZrO₂ from alkaline gels is more easily achieved. Which value in the table is the most realistic is not easily decided, but E has values close to those obtained from the Kissinger equation for n = 1, m = 1 only, which again suggests a surface nucleation mechanism; see also Tables 4.13 and 4.14.

Collected below are the calculated ranges for the activation energies using the different analyses which show the agreement is only good when parameters indicative of surface nucleation are used (Table 4.15).

Table 4.15

Ranges of activation energies using different analyses

Activation Energy from Kissinger Equation kJ mol ⁻¹	Activation Energy from Ozawa Equation for surface nucleation kJ mol ⁻¹	Activation Energy from Ozawa Equation for bulk nucleation kJ mol ⁻¹	Activation Energy from modified Kissinger Equation for surface nucleation kJ mol ⁻¹	Activation Energy from modified Kissinger Equation for bulk nucleation kJ mol ⁻¹
170-220	184-230	300-460	172-215	350-460

When Hayward considered the re-crystallization of various glass-ceramics his results showed values for E in the range 400-500 kJ mol⁻¹ with close agreement in every case between Kissinger equation values and Ozawa equation values when n and m for bulk nucleation for varying numbers of nucleation sites. Here we can only get Kissinger value and Ozawa value agreement when surface nucleation is considered i.e. n = 1, m = 1 and so this may be reasonable evidence for this mechanism.

This whole detailed study did lead to a method for making tet-ZrO₂ with reasonable stability and easier transformation possibilities for use in the context of strengthening and toughening OPC discs.

CHAPTER FIVE

DETERMINATION OF THE PROPERTIES OF THE PORTLAND CEMENT PASTE USED IN THIS RESEARCH

5.1 Introduction

This chapter presents work undertaken on standard samples of the OPC; given that one of the primary aims of the research was to assess the potential of tetragonal zirconia as a cement improver, particularly with reference to mechanical properties. For this reason the methods to be used had to be established in order that comparisons could be made to OPC-zirconia composites. At the outset it seemed possible to investigate the following properties with the apparatus available:

- (i) Strength
- (ii) Young's modulus
- (iii) Fracture toughness
- (iv) Hardness
- (v) Microstructures
- (vi) Water uptake

The initial work was aimed at fixing variables such as water to cement ratio, sample geometry, setting conditions and times before establishing consistent testing procedures.

Samples were all prepared and examined as described in section 3.3. Examining some of the microstructures observed here highlights the

magnitude of the difficulty involved in obtaining consistent data in cement research.

The discussion of cement hydration in Chapter 2 leads to the conclusion that hydrated paste can be considered as a composite material consisting largely of C-S-H, CH, unhydrated cement particles, and pore space. The amount of each component depends on the degree of hydration and w/c ratio. This is not unexpected as it is commonly found that pores are concentrated on fracture surfaces because of course they are the main cause of failure. From the micrograph (Figure 4.4) the dark, porous area, has pores from 0.5-4 μm in cross section.

The polished surfaces of the samples prepared by the dry pressed-infiltration method were examined and the microstructures were not good because there were too many cement particles that were unhydrated. Pores were clearly present, especially around the unhydrated particles. Clearly, the pores, their number and uneven distribution, were going to dominate the properties and so the infiltration method was abandoned and a hand mixing method was developed to get a paste suitable for using in a press to improve the pre-set microstructure. However, before amassing data, a standardised procedure for shaping the samples had to be established prior to choosing a water to cement ratio. This search became an essential part of developing a satisfactory method for determining fracture strength which by necessity would mean the preparation of many hundreds of samples.

5.2 Development of a Fracture Strength Procedure

We were from the outset interested in trying to improve the tensile properties of OPC pastes by zirconia additions and so a baseline procedure and data to compare with for OPC alone was needed. First of all standard flexural test methods on small beams were tried.

5.2.1 Flexural Test

Flexural tests determine the tensile strength in bending and when hydraulic cements are subjected to bending, direct shearing stresses are developed. This test more commonly employs beams and slabs and it may be carried out in several ways. The most common way is to apply the ASTM (C78) test using a simple beam with three-point loading as shown in Figure 5.1 with centre point loading as described in ASTM (293).

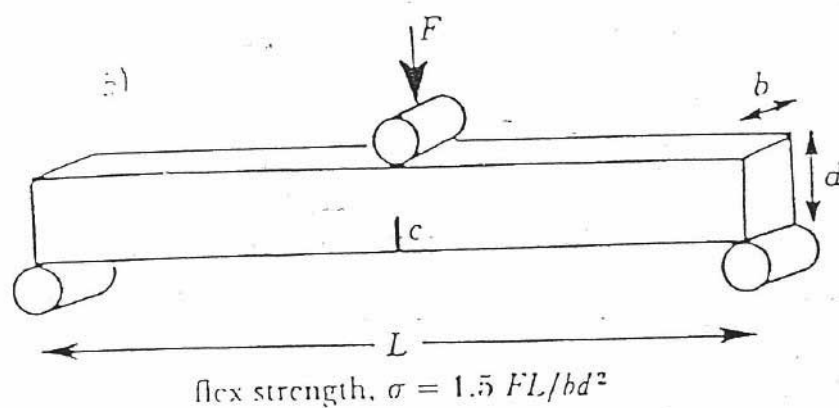


Figure 5.1: Flexural strength testing arrangement¹⁸⁹

Flexural strength is expressed in terms of a modulus of rupture, which is the maximum stress at failure computed from the well-known flexural formula:

$$\sigma = MC/I \quad (5.1)$$

In the equation σ is the stress or modulus of rupture, M is the maximum bending moment, C is one-half of the beam depth and I the moment of inertia of the cross section.

At first this was thought to be the method to use and numerous OPC paste bars were made with nominal dimensions 55 x 10 x 5.2 mm in a demountable wooden mould. Great variation in the appearance of such beams matched wide variation in strength and macrostructure. Noticeable curvature was often produced and different water to cement ratios did not affect this situation, nor did applied pressures from the top surface. The most probable reason for this was uneven drying rates through the sides and ends of the moulds compared to the top surface. Cutting and polishing to achieve sound external geometry and dimensions was not easy and often resulted in poor final appearance and beam dimensions varying in the range $L = 40\text{-}52$ mm, $d = 8.9\text{-}10.0$ mm, $b = 5\text{-}5.2$ mm and $c = 4.2\text{-}4.9$ mm. Many samples were grossly cracked. A typical set of data for a batch of samples is shown in Table 5.1.

Selected results are given in Table 5.2 where it can be seen that when care is taken in selecting samples consistent strength values can be obtained. However for each result shown at least 10-15 samples had to be discarded on the grounds of appearance, failure to be able to cut a satisfactory beam, or gross cracks and other microstructural features producing a very low strength reading. The data suggests a dependence on the water to cement

ratio such that an increase in w/c ratio was associated with a decrease in flexural strength (MPa).

Table 5.1

A batch of Six OPC beams tested in 3-point bend mode; w/c = 0.23, 28 days aging

L mm	d mm	b mm	c mm	Failure load N	Flexural strength σ MNm ⁻²
40.0	9.2	5.2	4.3	46.4	6.29
40.0	9.7	5.7	4.0	25.1	4.73
40.0	9.7	5.0	4.0	22.4	2.86
40.0	8.9	5.2	4.9	28.5	4.13
40.0	10.0	5.2	4.5	57.4	6.59
40.0	8.9	5.0	4.3	28.8	4.34

Furthermore it was observed that for the same w/c ratio there was also a gradual decrease in flexural strength (MPa). Similar decrease in flexural strength was observed in other studies where an inverse proportional relationship was observed with respect to w/c ratio⁽¹⁷⁷⁾. Clearly this is not a satisfactory way to proceed and from this effort it was decided that some improvement particularly with respect to repeatability would only be achieved with smaller samples made in a more controlled way. This suggested the Brazil test as the way forward.

Table 5.2

Relationship between flexural strength of hcp and water to cement ratio

w/c ratio	Flexural strength MPa	Mean MPa
0.2	6.91, 6.74, 6.29, 6.88, 5.96	6.56±0.42
0.23	6.07, 6.15, 6.08, 6.13, 6.12, 6.29, 6.59	6.20±0.18
0.30	6.74, 5.57, 6.64, 6.14, 5.79	6.18±0.51
0.35	5.60, 5.33, 4.67, 4.25, 5.30	5.03±0.55
0.40	4.12, 3.89, 4.07, 4.21, 4.10, 3.37	3.96±0.31

5.2.2 The Indirect tension method: The Brazil test

The standard test has been described in Chapter 2. Here a few variations were developed, for example the specimens were prepared under a constant pressure to improve the microstructure and to produce small compact cylindrical shapes that could be kept in at controlled humidity for the necessary time before testing. Realising that applying pressure could squeeze out water an optimum pressure had to be chosen and this was done via an extensive set of trials. More than 100 sample batches were tested as groups of 6 for different periods of ageing. The large sample size and the time variation are reflected in the rather large error. Table 5.3 shows the experimental results for 4 batches of 28 day hydrated samples. There was a definite indication that the pressing load should be set at 3 kN and so 0.35 tonnes was applied to the die that contained the paste discs as this produced the strongest samples with least visible evidence for water press out.

Table 5.3

Brazil Fracture strength of OPC pastes aged for 28 days. Pressed at 3 kN m² (w/c of 0.23)

Batch 1 Fracture Strength MN m⁻²	Batch 2 Fracture Strength MN m⁻²	Batch 3 Fracture Strength MN m⁻²	Batch 4 Fracture Strength MN m⁻²
7.3	7.8	7.9	7.0
9.0	7.4	8.9	7.3
6.4	8.6	9.6	8.2
9.1	6.3	7.7	9.0
10.5	7.6	10.2	9.3
11.3	7.4	9.3	8.2
Mean 9.0	Mean 7.5	Mean 8.9	Mean 8.2

Soft wool was attached to the disc rim to prevent the steel damaging the sample. The method allowed only correctly fractured samples to be considered, that is, samples that failed along the vertical diameter only.

The data in Tables 5.2 and 5.3 are comparable in magnitude but the improved structure gained by pressing discs is reflected in the improved sample strengths. The ability to disregard results where the failure mode was not down the disc diameter is also reflected in the smaller batch variation for the Brazil test compared to the three-point bend test. There were sufficient samples tested to detect a significant deviation when different failure modes occurred at all ageing times and these data are shown in Table 5.4, where triple crack failure leads to increased strength values. All of this, along with comparable data from compression tests done by the cement manufacturers and shown in Table 5.5, is presented as justification for selecting the procedures described. The new procedure was used to study the effect of some system variables as described below.

Table 5.4

The effect of failure mode and sample ageing time on Brazil strength of nominal w/c 0.25 pastes pressed at 0.3 tonnes (triplicate samples)

Ageing time	4 Hr	6 Hr	8 Hr	1 Day	4 Day	7 Day	14 Day	16 Day	28 Day
Triple crack failure strength MNm ⁻²	-	2.8 ± 0.12	-	8.2 ± 0.15	-	11.0 ± 0.09	11.3 ± 0.21	-	11.4 ± 0.15
Diametral failure strength MNm ⁻²	0.47 ± 0.22	-	4.1 ± 0.11	6.8 ± 0.13	7.9 ± 0.33	8.2 ± 0.25	-	8.4 ± 0.08	8.5 ± 0.12

Table 5.5

Manufacturer's data for compressive strength of OPC prisms made from material supplied for this research.

Setting time Days	Compressive strength MNm ⁻²	Tensile strength* MNm ⁻²
2	27.0	2.7
7	46.0	4.6
28	69.5	7.0

* see text

5.2.2.1 Results of the effect of water cement ratio

As discussed in Chapter two there are several important factors that influence the strength of a hydrated cement paste and one of these is the water to cement ratio. The results given in Table 5.2 for the 3-point beam test confirm this. Beam tests were used because the pressed discs squeezed out some free water. Higher strength can be achieved by keeping the w/c ratio low, but it should be recognised that low w/c ratio of cement paste commonly in the range, 0.23–0.30, has a characteristic microstructure different from that with higher w/c ratio. The low w/c ratio paste is a more heterogeneous composite material than the high w/c ratio cement paste because it contains significant amounts of unhydrated cement particles embedded in a C-S-H matrix that according to Peterson⁽¹⁴¹⁾ prevent further hydration at the water tensions available at this w/c ratio ~0.25. The unhydrated cement particles, and the C-S-H matrix, both contribute to strength. The relationship between w/c ratio and the fracture strength of 4-week old hardened cement paste beams tested here. A relationship is observed that shows a somewhat linear decline in strength from about 0.2 w/c upwards. However, for some w/c ratio (especially in the lower range), there was no *decline*, and an increase was

observed. The range of values, 6.6-4.0 MPa, for strength is in keeping with the microstructure. The w/c ratios used in this work were in the range 0.22-0.28 and the strength for such samples is seen to be 5.5-6.0 MPa in line with values in Tables 5.2.

However when comparing the data to that in Table 5.3 it suggests that pressing decreases the w/c ratio from 0.28 to about 0.15 where strengths are about 8.5 MPa. Hence the effect of pressing is not only to give a more consistent microstructure but also to reduce the w/c ratio in a controlled way, assuming that pressing at the same load for the same time removes the same amount of water. It helps to explain why increasing the pressing load does eventually lead to a decrease in strength as too much water is pressed out and the w/c ratio drops below about 0.1.

Data obtained at a much later date in this research on samples prepared and stored in controlled humidity for a time test in Jordan combined with data obtained in Bradford, confirm the improved strength at lower w/c ratios. The results for the average of 5 samples that failed diametrically per batch aged over different times and with different trial w/c ratios are shown in Table 5.6.

Table 5.6w/c effect on Brazil strength at different ageing times (Data: Mean \pm S.D.)

Time Days	0.33	1.0	3.0	7.0	14	21	28	90	180
w/c									
0.33	4.4 \pm 0.32	4.5 \pm 0.55	4.7 \pm 1.06	4.8 \pm 1.12	5.8 \pm 0.75	-	7.2 \pm 0.57	7.6 \pm 0.00	7.6 \pm 0.22
0.25	4.3 \pm 0.31	5.6 \pm 0.78	6.2 \pm 1.25	6.5 \pm 1.37	6.9 \pm 0.66	7.2 \pm 5.09	8.0 \pm 0.45	7.6 \pm 0.47	7.9 \pm 0.23

5.2.2.2 Results on the effect of porosity

Porosity is one of the major factors controlling the chemical attack and the mechanical properties of Portland cement ⁽⁶³⁾. There are two ways of reducing the porosity of hydrated cement (a) use a lower w/c ratio and (b) to compact the paste by using pressure in the disc preparation. As shown in 5.2.2.1 these two routes are in conflict regarding strength effects beyond a critical pressure and w/c ratio. Since very many samples were used in strength tests it was possible to determine the total porosity by water uptake after fracture of the discs and to examine porosity Vs. strength and porosity Vs hardness and Young's modulus relationships. The relationship is non-linear which in line with other investigators ⁽¹⁶⁵⁻¹⁶⁷⁾ who have noted that the relationship between strength and porosity is not a simple linear function.

It is interesting to note that in the region of 20-25.5% porosity, which is probably the range of many laboratory prepared pastes; the strength-porosity curve is fairly shallow covering values in agreement with all the data shown in Tables 5.1-5.5. Hence the variation in the results from batch to batch and within batches probably just reflects differences in porosity once failure mode is taken into account.

As Chapter two has indicated eqn. (2.15) shows an linear relationship between strength and porosity. Nevertheless, obtaining agreement is quite encouraging and gives confidence in both the sample preparation method and the chosen Brazil-test procedure.

Again this is a non-linear function and serves to emphasise that close control of the experimental preparation of our test discs was very important since strength and porosity are exponentially related. It was becoming clear that carefully controlling an initial starting w/c ratio, the disc pressing load and time, combined with careful observation of fracture mode before accepting a reading, was limiting the variation in the property measurements. This was quantified to some extent in 5.2.2.4.

5.2.2.3 The effect of time on measured strength

The initial setting time for the OPC used for this research was quoted by the Manufacturers as 145 minutes but the test details, such as w/c ratio, were not supplied. The initial setting time for the chosen w/c ratio of 0.25 was determined in the way described in chapter 3 and was consistently found to be 80 minutes. It will be seen in chapter 6 that additions of zirconia consistently reduce this time. Initial setting times depend on w/c ratio, increasing with extra water, which suggests that the manufacturers used a more common w/c ratio around 0.33.⁽¹⁷⁷⁾

The manufacturers supplied compressive strength results obtained for mortar prisms at three different times that reflect the effect of time on strength and

encouragingly provide independent confirmation of the tensile strength data changes with time already shown here. Compressive strength values at an w/c ratio of 0.25 are given in Table 5.6 that when divided by 10^{83} , the usual factor between compressive and tensile strengths for ceramic systems are very comparable to diametral tensile test values at different times obtained here and shown in Tables 5.4 and 5.5.

When some of the strength-time data are considered they suggest three different periods in the setting process. For OPC alone there seems to be one process in the 0-8 hour range when about 50% of the final strength is gained. A slower strengthening process from 8 hours to 4 days and finally a much slower strength gain from 4 days to 28 days follow this stage. Similar differential setting rates in three phases has been reported in other studies with OPC. To show this the data is presented as Log time in hours. ^(177, 178)

Differences are also noted in the compressive and tensile strengths of mortars and pastes based on the porosity of the starting material. A decrease in strength is observed with increase in porosity and since the porosity of mortars and pastes differ, they differ in the values for compressive and tensile strengths. Also, because of differences in composition of mortar and paste, the strength of the former is more than the latter. Furthermore, this also leads to less shrinkage in mortar versus paste.

5.2.2.4 Determination of the Weibull modulus of OPC

In this research it was possible on some occasions to amass enough test data for some compositions to make a Weibull analysis, as outlined in Chapter 2.

Enough strength data for hcp discs at a nominal w/c ratio 0.25 was generated to establish a Weibull modulus using a previously published method in the literature. ⁽¹⁷⁹⁾ There is though variation in these data from which the Weibull modulus of hcp, as prepared using the methods here, is obtained. The value at 6.8 is seen to be low but not out of order for ceramic and cementitious systems. ⁽¹⁸⁰⁾

5.3 Determination of Young's Modulus

Young's modulus of elasticity is the constant relating change of tensile stress with elastic strain. It is a measure of the stiffness or the resistance of the material to deformation. However, since OPC, mortars, and concrete, like most other structural materials are imperfectly elastic, the stress-strain diagram is in fact a curve and not linear and this fact leads to the definition of several moduli. For example the modulus of elasticity in flexure is defined from the way it is determined by the deflection of a loaded beam. For a beam simply supported at the ends and loaded at mid-span, an approximate modulus may be determined from eqn. (5.2)

$$E = P L^3 / 481 IY \text{ (5.2)}$$

Where E is young's modulus, P is the applied mid-span load, L is the distance between supports, I is the moment of inertia of the section and Y is the mid-span deflection due to load P. In order to test more samples on equipment more readily available a lesser-known method using a Knoop hardness diamond was tried on some of the fractured Brazil test samples. The results from these experiments are given in this section.

5.3.1. Results from the resonance frequency method.

The typical dimensions of OPC bars with w/c ratio of 0.23 are given in Table 5.7. The porosity was determined by immersion in water for these bars. As expected the porosity values were larger than the pressed discs. Eight samples were used. Figure 5.2 shows the relationship between Young's modulus and the porosity of these OPC bars. It is clear that this is not a linear relationship. These data follow equation (2.17) as the better representation of the relationship between porosity and modulus.

Table 5.7

Beam dimensions, porosity and Young's Modulus of OPC bars w/c of 0.23

Length mm	Resonant frequency Hz	E GPa	porosity %
21.8	84680	28.2	22.2
27.5	61123	24.2	25.3
22.7	74286	25.2	24.5
20.9	76125	19.6	28.8
30.6	51377	20.7	28.1
33.1	50199	20.6	27.6
22.8	64913	18.1	30.2
23.3	60128	17.2	31.2

The mean value of E from this method was 21.8 GPa. ⁽¹⁸¹⁾ This is within the range for the mean value of E reported in literature (10-30 GPa).

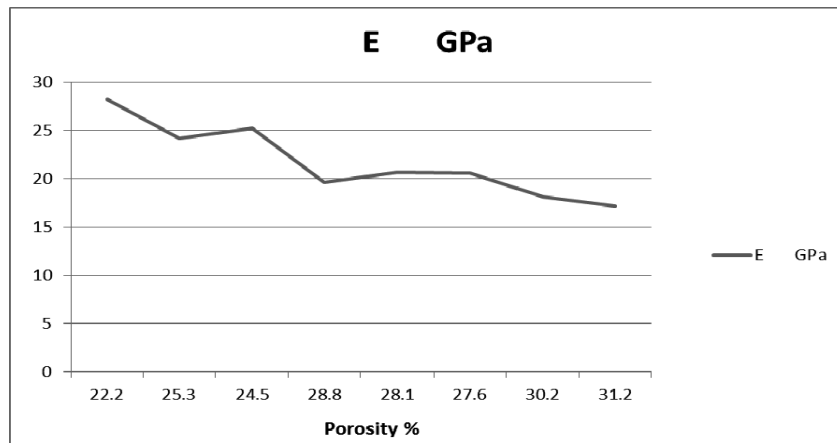


Figure 5.2: Relationship between Young's modulus and the porosity of these OPC bars

5.3.2 Results from Knoop indentation hardness tests

The polished surfaces of the pressed discs could be Knoop indented using loads in the range 0.49-4.9N if care was taken. It was not always easy to make the indent. Table 5.8 contains the dimensions of the indent and the calculated Young's modulus for each indent using eqn (3.8). The average value for E in Table 5.8 is 22.6 GPa which is in good agreement with the value derived from the resonance frequency method, especially considering the decreased porosity of the discs when made by uniaxial pressing.

Table 5.8

Knoop indentation hardness and values of Young's modulus calculated from them compared to porosity for OPC at w/c = 0.23 (triplicates).

Short axis b μm	Long axis a μm	H _k GPa	E GPa	Porosity %
16	131	0.82	20.1	22.5
15	121	0.92	26.3	18.2
17	140	0.72	17.0	25.5
17.5	138	0.74	24.4	19.1
16	125.5	0.91	31.5	13.1
16	129	0.85	23.2	20.4
14.5	122	0.95	19.8	23.0
16	133	0.80	17.8	24.3
15.5	127	0.88	21.3	21.6
17	134	0.79	25.8	18.3
16.5	132	0.81	23.5	19.9

(The short and long axis measurements are the average values of 20-30 indentations per sample which is standard procedure for microhardness methods of heterogeneous samples. The triplicate you mention was for three discs of the same batch.)

5.4 Micro hardness and large-load hardness

5.4.1 Microhardness

Micro hardness was measured by means of a Leitz miniload machine with Vickers and Knoop pyramid indenters and loads in the range 4.91-19.6 N. Polished discs were used to make the indents on the surfaces of fractured discs previously used in Brazil strength tests.

Vickers microhardness was calculated using eqn (5.3):

$$H_v = 18.19 P / d^2 \quad (5.3)$$

In eqn. (5.3), H_v is the Vickers hardness, GNm^{-2} , P is the load in Newtons, and d the indent diagonal in μm . The Knoop hardness was calculated by using eqn (5.4).

$$H_k = 2P/a^2 (\cot 172.5^\circ + \tan 130^\circ) \quad (5.4)$$

In eqn (5.4), H_k is the Knoop hardness, GN m^{-2} , P is the load in Newtons, and a is the long diagonal length in μm .

To identify trends in the change in hardness is complex because as well as the variables, such as w/c ratio, hydration time, and pressing load, the results depend on the test method used, the load used, the small area examined relative to the microstructural variations, and variable and unpredictable

cracking around the indents. The procedure adopted was to make very large numbers of indents on numerous specimens and to group the data within the identified variables. In particular cracked indentations were not considered alongside un-cracked examples and this showed that this variable produced the largest variation in the data. Using loads between 1.96 and 98.1N produced cracked indentations on an unpredictable basis with crack numbers increasing as the load increased but when the load exceeded 100N un-cracked indentations were rare.

Table 5.9 contains the summary of data obtained for a load of 4.9N when indentations were cracked at each corner. Each number in the Table is the mean of at least 5 measurements per sample. The Vickers hardness has a mean value of 0.33 GNm⁻². In comparison, at the same load of 4.9N, Table 5.10 shows that un-cracked indents lead to much higher hardness values with a mean of 1.76 GNm⁻². The data in the Table also shows the effect of hydration time on hardness, which increases as the free water is consumed and the products crystallise with time. Further consideration of the data in Table 5.11 shows that the hardening effect continues up to 6 months.

Table 5.9

Vickers Hardness and Fracture Toughness* for 28-day OPC at w/c = 0.23-0.25 using a 4.9N load.

Indent diagonal length μm	Crack length μm	Vickers Hardness GPa	Fracture Toughness K_{Ic} $\text{MPa m}^{1/2}$
152	76 + 120	0.39	0.28
171	86 + 108	0.31	0.32
159	80 + 129	0.36	0.24
167	84 + 111	0.33	0.31
148	74 + 123	0.41	0.53
184	92 + 121	0.27	0.29
175	88 + 139	0.30	0.26
149	75 + 123	0.41	0.28
151	76 + 122	0.40	0.28
160	80 + 132	0.35	0.43
157	78 + 118	0.37	0.27
164	82 + 125	0.34	0.28
228	114 + 133	0.18	0.27
169	85 + 130	0.32	0.27
177	89 + 132	0.29	0.26
154	77 + 128	0.38	0.26
162	81 + 134	0.35	0.26
169	85 + 127	0.32	0.27
181	91 + 133	0.28	0.27
Mean±Standard Deviation			
167.21±18.23	83.84±9.12 + 125.68±7.96	0.33±0.06	0.30±0.07

Table 5.10

Vickers Hardness of OPC with w/c = 0.25, load 4.9N. Data from uncracked indents

21 days hydration H_v GNm^{-2}	28 days hydration H_v GNm^{-2}
1.65	1.98
1.17	1.89
1.28	1.32
1.11	2.07
0.97	2.41
1.38	1.20
1.17	1.35
1.36	2.66
1.22	1.92
0.93	1.40
	1.19
Mean 1.21	Mean 1.76

Table 5.11

The effect of load and hydration time on the Vickers hardness of OPC w/c
=0.25

Hydration time days	21	28	91	183
Load N	H _v GNm ⁻²	H _v GNm ⁻²	H _v GNm ⁻²	H _v GNm ⁻²
0.49		1.19		
1.96		1.36		
4.91		1.76		
9.81	1.13	1.18		
19.6		1.12 1.04		
24.5	1.00			
49.1	0.97	1.02		0.92
98.1	0.92	0.95		0.77
196.2	0.30	0.33		0.88
294.3	0.17	0.17	0.72	0.87
490.4	0.12	0.13 cracks 0.47 uncracked	1.42	1.09
981	samples shattered	samples shattered	samples shattered	0.33

Table 5.8 shows the Knoop microhardness at the 4.9N load for un-cracked indents. The mean value for the Knoop hardness is 0.87 GPa. Knoop indentations are shallow compared to Vickers indents and to some extent measure a surface property as opposed to a bulk property so accounting for some of the difference in value. Furthermore the projected area is used to calculate the hardness and not the contact area, as is the case with Vickers measurements. The relationship between microhardness and porosity is also evident in Table 5.8.

5.4.2. High Load Hardness

Many tests were made in the load range 9.8 to 981N on a macrohardness machine fitted with a Vickers diamond. The effects ranged from complete sample fracture through to clear un-cracked indents. Once again data was considered in terms of the appearance around the indent and the summary is presented in Table 5.11. The data show the normal trend for samples

hydrated for 21 or 28 days, that is, the hardness decreased as the load was increased from 4.9N upward. Below a load 4.9N the microhardness varied across different parts of the sample. The maximum hardness is indicated at 4.9N as 1.76 GNm^{-2} .

When loads exceeded 98.1N it was difficult to find indents free from cracks whereby hardness values fell to values below those in Table 5.9. This confirms the dramatic effect of cracking on the measured hardness values.

Table 5.11 confirms that hydration time has a continuing effect on the measured hardness, particularly so since a few 3 and 6 month old samples were available and were successfully tested. The data for these old samples were more variable but do suggest a greater resistance to indentation cracking as they maintain a hardness of 1.06 GNm^{-2} at test loads of 490.5N, only dropping to expected levels when cracks appear for 981N loads. Only the 6-month sample could support the 981N load. Summarising so far it seems that the OPC pastes with w/c ratio of 0.23-0.25 have a maximum Vickers hardness of 1.78 GNm^{-2} and Knoop hardness of 0.8 GNm^{-2} under a 4.9N load as long as the indents are un-cracked. The Vickers value falls to 0.33 GNm^{-2} when the samples develop cracks at the indent corners. The resistance to cracking increases along with hardness as the hydration time extends to periods of months. These results have also been confirmed by other studies where it was found that decreased hydration time resulted in an increase in cracking and vice versa. ⁽¹⁸²⁾

5.5 Toughness and Hardness-Fracture Studies

5.5.1. Notched Beam Method

A few beams from the initial exploratory work were available to try the standard notched beam procedure and establish a check with the cracked indent technique. A measure of the toughness of the OPC samples comes from calculating K, the toughness parameter, using end-supported beams with standard dimensions and applying a load at the centre above an introduced sharp notch. In this situation K is related to the test specimen geometry by employing the compliance coefficient technique that leads to eqn.(5.5):

$$K = P/BW^{0.5} [1.93(a/W)^{0.5} - 3.07(a/W)^{1.5} + 14.53(a/W)^{2.5} - 25.11(a/W)^{3.5} + 25.8(a/W)^{4.5}] \quad (5.5)$$

In eqn.(5.5), P is the load at failure, W is the beam thickness and B is the width, a is the notch depth made with a diamond saw and finished with a sharp blade to a depth close to W/2 in an attempt to ensure cracking from the end of the notch.

The few samples that were satisfactorily tested to failure are summarised in Table 5.12.

Table 5.12

Toughness parameters for OPC beams with w/c = 0.23 (Age: 3 weeks to 6 months)

L mm	W mm	b mm	a mm	a/W	P N	Strength MNm ⁻²	K MNm ^{-1.5}
40	9.21	5.22	4.3	0.47	46.4	6.3	0.89
40	9.72	5.72	4.0	0.41	25.1	4.7	0.36
40	9.68	5.00	4.0	0.41	22.4	2.9	0.37
40	8.80	5.16	4.6	0.52	11.0	1.7	0.26
40**	9.76	5.68	4.0	0.41	22.2	2.5	0.32
40**	9.42	5.52	4.4	0.47	8.6	1.1	0.16

** sample contained zirconia 5-10 wt%

There was considerable difficulty in preparing these samples for examination and performing the tests with most samples failing to provide a result. With the exception of the $0.89 \text{ MNm}^{-1.5}$ there seems to be some consistency about $0.33 \text{ MNm}^{-1.5}$ for the OPC pastes. This is in line with the information presently in the literature for OPC pastes of unspecified w/c ratios. ⁽¹⁸³⁾

5.5.2 Cracked Indentation Method

As explained in 5.5.1, attempts to use the 3-point bend method on bar-shaped samples of the cement paste were very erratic, mainly due to the failure to produce consistent microstructures or indeed satisfactory geometrical samples. Hence it was decided to try to use indentation methods in the knowledge that samples were easy to prepare and available in the form of broken Brazil test samples. It was decided to use the Nihara equation:

$$K_c = 0.0667(E/H_v)^{0.4} H_v a^{1/2} (c/a)^{-3/2} \quad (5.6)$$

This equation was chosen because experimental values for the modulus of OPC were available and the a/c ratios found here are in the regime of this equation.

It has already been stressed in 5.4.1 and 5.4.2 the difficulty encountered with unpredictable cracking of the samples when pure OPC discs was used. From the extremely large number of samples examined it was possible to get a set of satisfactorily cracked samples for the 4.9N load and these data are shown in Table 5.9. For loads greater than 9.8N there was greater difficulty because

either samples shattered or the cracks coming from the indent corners were so long they extended to the edge of the sample. Another feature was that frequently cracks occurred at only one or two corners, or indeed none at all, which did not allow a crack length to be determined. Interestingly, these problems were less often encountered when the samples contained zirconia and allowed a fuller discussion in Chapter 6.

The experimental K values for OPC with $w/c = 0.23$ have a tolerable variation to give a mean value of $0.30 \text{ MNm}^{-1.5}$, which falls within the reported values for OPC paste found by more conventional methods showing that the method is usable for these systems and confirms the earlier attempt by Beaudoin⁽¹⁵⁸⁾ to use this technique. The greatest difficulty is measuring the crack length on the Leitz instrument and so some samples were indented and examined on the SEM in order to measure the crack length and the indent diagonal; for these the K value is $0.31 \text{ MNm}^{-1.5}$. This compares very well to the average value calculated from the measurements made on the Leitz machine.

Taking the values from the notched beam samples, 5.4.1, into consideration there is a satisfactory value of about $0.31 \text{ MNm}^{-1.5}$ for the OPC used at a w/c ratio of 0.23-0.25 and this can become with some confidence the comparison value when the zirconia doped samples are measured.

5.6 Thermal analysis and hydration

Two facts lead to some work in this area. First a very sensitive microbalance had been constructed that was built into a controlled temperature and humidity box and it might show features of the hydration process. Secondly, the combined TG-DTA equipment used for the zirconia gel studies was available from an accessibility standpoint compared to other similar equipment.

5.6.1 Hydration Microbalance Thermogravimetry

It was hoped that this could be developed as a technique to study the hydration mechanism and the effect that zirconia had on it. The balance was based on a C.I. Isothermal balance head housed in an insulated, temperature controlled cabinet fitted with a double glazed access door, a water reservoir, cubicle heater, sample heater and air circulator.

In use the balance was zeroed with an empty silica sample boat and then a 40-100mg sample was added. The temperature was raised to 70°C and the cubicle evacuated for at least 2 hours to dry the OPC sample. After cooling the sample temperature was set, the vacuum released and water vapour admitted. Mass gain against time was monitored from 0 to 1400 minutes.

Total mass gains were small over the chosen time period, being only 7-20 μg , but these were real because the empty container gained only 1 μg over 1400 minutes. All tests showed a repeatable pattern:

- (i) 0-75 mins. An initial linear mass gain of 1-3 μg .
- (ii) 100 mins. No mass gain.

- (iii) 200-600 mins. A linear gain of 3-6 μg .
- (iv) 100 mins. No mass gain.
- (v) 800-1100 mins. Linear gain 7-10 μg .
- (vi) 1100-1400 mins. No mass gain.

This step-like reactivity was analysed as an overall rate and as three linear rates for a few tests and the data are tabulated in Table 5.13 and comparable data for samples containing zirconia is shown in Chapter 6.

The reaction-pause sequence probably reflects surface absorption/saturation then water diffusion into the sample. Table 5.13 suggests a complex interplay between the effect of temperature and water vapour pressure increase giving minimum effect for the 35 °C combination.

Table 5.13
Rates of water absorption for OPC

Temperature °C	Vapour pressure mm Hg	Overall rate $\mu\text{g min}^{-1}$	First linear rate $\mu\text{g min}^{-1}$	Second linear rate $\mu\text{g min}^{-1}$	Third linear rate $\mu\text{g min}^{-1}$
25	2.8	0.008	0.04	0.010	0.007
35	42.2	0.004	0.006	0.013	0.006
45	71.9	0.008	0.01	0.013	0.022

5.6.2. DTA-TG of OPC paste w/c = 0.24 and 28 days set.

Before the set samples were tested the OPC powder as received and stored was run from 20-600°C. There were no DTA peaks observed in this temperature range but the TG registered an overall mass loss of 1.25%. This loss was due to surface dampness and organic contamination which indicated that the decomposition that results could be used to identify different species.

When small pieces of the 28-day set material were taken through the same temperature interval, a large, broad endothermic event, beginning at 40 °C and ending at 280 °C, occurred. This broad peak had a shoulder at 120 °C and a broad maximum at 165 °C during which time a mass loss of 4.9% was recorded. A second broad endotherm was observed as a shallow peak at 485 °C corresponding to a second mass loss of 0.5%. ⁽¹⁸⁴⁾This can be used to deduce the degree of hydration via comparison of pure OPC pastes with OPC-ZrO₂ composites. Similar such tiers of endothermic events during cement hydration have been reported in literature, however with different temperature peaks, beginning at 105 °C and ending at 500 °C.

After cooling the sample showed an overall mass loss of 7.4%. If all the water had been removed from the sample this was expected to be in the range 15-24 % depending on the “squeeze-out” when the discs were prepared. All this suggests that at least half the added water is transformed to stable structural water during the 28-day period. The effect that tetragonal zirconia and zirconia gel have on the hydration process might be monitored this way especially since the gel has such a strong exothermic event around the 485 °C temperature peak.

5.6.3 Time to initial set.

The progress of setting has, as shown in this chapter, strongly influences hardness and strength. The time to initial set was found by the conventional. For all samples with w/c 0.23-0.26 the test showed little variation around 80 minutes to initial set as shown in Table 5.14.

Table 5.14

Setting times for OPC at different w/c ratios

Time	w/c ratio			
	0.23	0.24	0.25	0.26
15	48	47.6	47.2	47
30	46	45.8	45.2	44.9
45	42	41.5	41	40.8
60	34	33.9	33.7	33.3
80	32.5	32	31.9	31.8

The data in this chapter are believed to be consistent and provide the means of comparing the effect that zirconia has as an additive to OPC. The experiments to achieve this are described in chapter 6.

* Calculated from Eqn (5.3), when cracks were observed emanating from the indent corners, using an average value of E, as found by the resonance frequency method and the Knoop method, of 22.3 GPa.

5.7 Summary results

Table 5.15 summarises some of the key properties of OPC at w/c of 0.25

Table 5.15

Summary of OPC properties at w/c ratio of 0.25

Compressive strength MNm⁻²	27.0, 46.0, 69.5 at setting times of 2, 7 and 28 days respectively
Tensile strength* MNm⁻²	2.7, 4.6, 7.0 at setting times of 2, 7 and 28 days respectively
Vickers Hardness H_vGNm⁻²	1.21 and 1.76 at 21 and 28 days of hydration respectively
Fracture Toughness K_{IC}MPa m^{1/2}	0.30±0.07
Flexural Strength MPa	6.38±0.13
% Porosity	26.62

CHAPTER SIX

PROPERTIES AND CHARACTERISATION OF OPC- TETRAGONAL ZIRCONIA COMPOSITES

6.1 Introduction

It was shown in Chapter two that there are studies that have introduced additives to cement in an attempt to improve the mechanical properties of pastes or mortars. In this study zirconia was of interest (as an additive to cement) as an extension to the research done on this advanced material's ability to bestow improved toughness to ceramic systems. Chapter 4 enlarged upon the different methods used to prepare zirconia in its tetragonal form. The method based on zirconium nitrate was chosen because, with this precursor, (rather than zirconium oxychloride or tetrachloride) the problem of leaving chloride ions in the powder was removed thus avoiding the issues highlighted by the work of Kayyali⁽¹⁷⁰⁾ who showed that the penetration of chloride ions into cement paste results in some loss in strength. The work in Chapter 4 showed that zirconium silicate would be a good precursor for tetragonal zirconia; but, since using $ZrSiO_4$ with OPC would increase the SiO_2 content in the OPC composition, this type of ZrO_2 precursor was not used for this work. Although, it would result in more C-S-H production, it would be rapid enough to cause release of excessive energy thus destabilizing the hardening process, which was another factor for not using $ZrSiO_4$.

The zirconia used was developed as described in section 3.2 and was the powder doped with 7 mol% SnO₂ because this produced a form of zirconia that was definitely tetragonal without being too stable (even though it provided the smallest particle size product) and might transform to the monoclinic form in modest stress fields. Section 3.4 described in detail how the discs were prepared and sections 3.5 and 3.6 how they were tested. Chapter 5 contains the data for the OPC against which any changes brought about by the additive could be assessed.

This chapter now explores different ways of introducing the zirconia to the system and measuring its effect on the properties.

6.2 Dry-mixing of OPC and tetragonal zirconia prior to hydration

Mechanical mixing of the dry powders was used to get composites with different percentages of tetragonal zirconia. After mixing dry, the w/c ratio was adjusted to the common range of 0.25–0.3 for which the OPC results had been obtained and discs were pressed according to the standard procedure. The presence of the zirconia was responsible for significant difficulty in achieving satisfactory discs from the die as more water appeared to be retained and the samples were quite soft. In some cases the discs were tested whilst setting but most were left for strength tests to be run at later stages of the setting process.

6.2.1. Observation on setting enthalpy, setting rate and porosity

(a) The effect on hydration enthalpy

The DTA/TG experiments were only sensitive for about 10 minutes and so the heat evolution curves (as usually shown⁽¹³⁾ which are determined over many hours) are not directly relevant. Curves of a consistent shape were obtained, which for OPC alone, was an instantaneous sharp evolution of heat producing a peak lasting 1 minute. This was followed by a smaller evolution lasting a further 1.5 minutes. A relatively long endothermic effect was then recorded lasting some 4 minutes. Thus there appears to be a very strong exotherm, a weaker exotherm lasting for a longer period and then an endotherm. These can be interpreted as the flash hydrolysis of the free lime, normal hydration exotherm and water evaporation endotherm caused by the increased sample temperature. ⁽¹⁸⁵⁾ Similarly increasing the level of alkalinity has been shown to affect the rate of hydration, which in turn affects the strength of OPC.

When 5wt% ZrO₂ was present (in a sample containing the standard mass of OPC) the effect was remarkable; the sharp exothermic event giving the spike-like peak was still present but the slower exothermic event was less evident and there was no endothermic dip. Thus after the flash hydrolysis of the free lime the hydration of the OPC appears to be more controlled and in particular the endothermic dip was missing. This seems to indicate that the presence of ZrO₂ inhibited water loss and overall the total positive, more controlled, heating effect was beneficial to hydration reactions.

When dried zirconia gel (not crystalline zirconia) was the additive a more obvious exothermic effect followed the initial flash hydrolysis and this gave a shoulder on the trace lasting for 3 minutes. Again the endotherm found in OPC was absent. The result when tetragonal ZrO_2 and the dried gel were tested as single materials in the same way reveals some hydration reactions with the ultrafine- ZrO_2 powders and that both the crystalline and amorphous materials behave, essentially, in the same way. Addition of the water causes an instantaneous exothermic spike but only about 20% as intense as that of the OPC and, as expected, the hydration reaction is greater for the anhydrous, crystalline product than for the gel. After 1.6 minutes a very broad exothermic peak arises from a slower reaction, lasting for some 5.5 minutes in both cases.

A possible explanation is a reaction between finely powdered CaO and ultra-fine ZrO_2 and water under the localised influence of the heat from the strong flash exothermic event.

To simulate the possibility (and obtain a sample suitable for X-ray analysis) an OPC + tetragonal zirconia mixture was heated to $90\text{ }^{\circ}\text{C}$ for 1.5 hours. X-ray lines (that were a good fit to a tetragonal unit cell with lattice parameters were found as per Table 6.1 below. This indirect evidence might support a solid state reaction between the CaO in the OPC and the ZrO_2 at the hydration stage. After this heat treatment the resultant powder mixture was not able to be re-hydrated into a paste that would set with any strength.

(b) The effect on initial setting time

In this work the initial setting time was the only one measured using the Vicat needle. Samples with a w/c ratio of 0.27 were used at room temperature of 18^o C. Clearly zirconia affects the initial setting time (which decreased from 80 minutes to 40 minutes) with increasing zirconia content. The overall increased temperature and reduced water loss (revealed by the DTA due to the presence of zirconia) is probably responsible for this effect. A similar effect can be observed in the presence of silica which causes rapid hydration of C3A. Furthermore finer particles will result in reduction of effective free water content due to higher specific surface area leading to cement particle aggregation and thereby reduction of setting time⁴³. Table 6.2 contain the data.

Table 6.1

X-ray crystallographic data for the product of OPC + tetragonal ZrO₂ heated to 90°C

Line	Relative Intensity %	Sin ² θ observed	Sin ² θ Calculated*	Hkl
1	80	0.0367	0.0369	100
2	80	0.0715	0.0717	102
3	100	0.0739	0.0739	110
4	80	0.0757	--	--
5	40	0.1022	--	--
6	100	0.1477	0.1477	200
7	60	0.1845	0.1846	210
8	80	0.2179	0.2173	005
9	60	0.2190	0.2194	212
10	60	0.2253	--	--
11	80	0.2959	0.2954	220

* Calculated for a tetragonal unit cell: a = 0.4009 nm, c = 0.8262 nm

Table 6.2

The effect of zirconia content on the initial setting time of OPC

Zirconia Content wt%	Initial setting time min
0	84
2	74
5	60
10	50
15	43

(c) The effect on total porosity.

As the setting time is decreased (and the early heat evolution controlled by the zirconia additions) a change in the overall water absorption porosity was noted. Whilst the setting time is progressively shortened (as the percentage zirconia increases) the total porosity decreases at about ≤ 1 hour. As later sections of the chapter show; this significantly affects the mechanical properties, in particular when the work was repeated at a lower w/c ratio and die pressure in order to have a more workable paste for disc manufacture. Table 6.3 shows that the effect of the zirconia content was not uniform. The lowest porosity was achieved at 5–7wt% tetragonal zirconia additions. It is not immediately obvious why the porosity should be affected in this way and, therefore, many fractured discs were examined in the SEM in order to view their porosities. Other studies have shown that porosity is also affected by the use of silica fumes that help to fill up the spaces thus enhancing the strength of the cement.

Table 6.3

The effect of zirconia on the total porosity of OPC

Zirconia content wt%	Porosity %
0	24
0.5	14
1	14
2	11
4	19
5	7
6	7
8	10
10	13
12	18

There was some visual evidence to suggest that macroscopic-sized pores may be associated with the areas containing zirconia agglomerates (as opposed to the area containing finely dispersed ZrO_2 crystallites). ZrO_2 having more electrons mean it is more reflective and appears as bright areas in the micrographs. It is very clear that large agglomerates of tetragonal zirconia are associated with a large-sized pore. Pore sizes elsewhere were smaller and more uniform. Thus when non-agglomerated and more evenly distributed, ZrO_2 may be an aid to the hydration and reduces the overall pore volume. In this case there is more than one aggregate associated with a macro-sized pore and there seems to be a good distribution of the whiskery microstructure characteristic of good hydration in the areas associated with the well-distributed zirconia.

In one sense the ZrO_2 beneficially partially fills the large pores but, in another, it seems to be that the aggregates generate the macro-sized pores; probably by absorbing more of the local water without producing the volume-filling calcium silicate hydrolysis products. Another possibility is that un-

hydrated OPC (near the zirconia hydrate) gradually removes water from the zirconia causing it to shrink and introduce porosity around it. The finer ZrO_2 aids good hydration, good microstructure and improved mechanical properties. These conflicting trends optimise in mechanical behaviour around 6wt% ZrO_2 and, when above this, the agglomerate-associated large pores are numerous enough to decrease the tensile strength as expected from Birchall's work⁽⁷¹⁾.

Many of the sample discs (containing 5% zirconia by weight) had uncharacteristic surface features as far as the presence and size of pores was concerned. Polished surfaces of discs of OPC alone and those containing high percentages of zirconia by contrast (most of the 5% zirconia samples by weight) were with only a 0.5-1.0% area and a much tighter size distribution. However about 10% of the 5% ZrO_2 by weight samples had more widely-dispersed pore sizes (overall % in the 3-6 range), which is below that for OPC alone. There is the likelihood that large crater-like pores were caused by water droplets being forced to the surface; a phenomenon not so common when zirconia was present (as it was when OPC alone was processed).

These simple observations and estimations are in line with the effect on total porosity measurements and imply that the zirconia at 5-6wt% has a significant effect on the hydration behaviour which in turn has a significant (*c*) effect on the microstructure.

(d) *The effect on water absorption rate*

The same experiments (as those done with OPC alone and introduced in 5.6.1) were conducted with samples containing 10wt% zirconia along with blank samples containing only ZrO₂. The same step-like behaviour was observed with some detectable changes compared to the dry OPC as Table 6.4 shows. The overall rate shows a growing increase as the water vapour pressure and temperature increases; which seems to be the result of the more rapid initial uptake of the water vapour. Overall, this is further evidence that zirconia improves the water retention of the system.

Table 6.4
Rates of water absorption for OPC and OPC + 10 wt% ZrO₂

Temperature °C	Vapour pressure mm Hg	Overall rate µg min ⁻¹	First linear rate µg min ⁻¹	Second linear rate µg min ⁻¹	Third linear rate µg min ⁻¹
25 OPC OPC + ZrO ₂	23.8	- 0.008 0.008	0.04 0.03	0.010 0.009	0.007 0.007
35 OPC OPC + ZrO ₂	42.2	0.004 0.007	0.006 0.007	0.013 0.008	0.006
45 OPC OPC + ZrO ₂	71.9	0.008 0.011	0.01 0.14	0.013 0.008	0.022

6.2.2 The effect of zirconia on strength and Young's modulus

Following all the development work with OPC alone (see chapter 5) only Brazil test measurements were made. Results from these tests are shown in Tables 6.5. The data in the Tables are (as for the OPC alone) the mean of, at least, 5 discs per composition batch and, where time-change results are shown, batches consisting of 5 discs, were kept for each time shown in

desiccators with hydrated salts to control the humidity. Care was taken to avoid triple-crack fracture data but interestingly this failure mode did not occur as frequently as in the OPC work. Most data was collected for crystalline zirconia additions; but some was available for gel additions.

The modulus measurements were made by both resonance frequency and the Knoop hardness method.

Table 6.5

Data showing the effect of time and w/c ratio on the strength of OPC and OPC-10wt% ZrO₂ composites

Time	OPC		OPC + 10wt% ZrO ₂	
	Strength MPa		Strength MPa	
	0.15 w/c	0.25 w/c	0.15 w/c	0.25 w/c
6hr	2.65	2.0	0.5	0.4
1 day	7.8	5.9	4.7	3.5
1 week	10.8	8.1	8.6	6.5
2 weeks	11.4	8.7	6.4	4.8
4 weeks	11.6	8.7	8.0	6.0

The first results (in Table 6.5) show that the effect of water-to-cement ratio is still quite marked and that, compared to OPC alone, there is a slower development of strength with curing time; even though the time to initial set was shortened by the presence of zirconia. There is a more variable look to the data for the 10% zirconia results that might reflect the sample preparation difficulties that were encountered with a w/c ratio of 0.25. However, there appears to be a continuing strength development over a longer time-span when samples are tested between 3 and 6 months (as the data in Table 6.6 show). The eventual strength surpasses that of OPC alone. Nevertheless, at the w/c ratios above 0.2 and for normal setting times the zirconia seems to weaken the composite.

Table 6.6

The effect of time and Zirconia content on strength for composites: w/c = 0.25

Time ZrO ₂ %	Strength MN m ⁻²									
	1 hr	7 hrs	1 day	3 days	7 days	14 days	21 days	28 days	3 months	6 months
5	-	2.6	4.8	4.9	5.4	6.2	6.9	9.9	12.6	13.3
10	5.0	5.7	5.7	5.8	5.9	6.0	6.9	10.2	10.3	10.6
2					6.6	6.5	6.5			
4					6.5	6.6	6.4			
6					5.9	5.9	5.8			
8					6.0	5.9	5.9			

The results distilled (Table 6.6) were disappointing and inconclusive in that it was hard to discern any strengthening effect for zirconia additions except if the samples were left for 3–6 months when both the 5% and 10% additions were eventually stronger than OPC alone after that time. This was not convenient and the uncertainties were increased when such long times elapsed after sample preparation. It was more confusing (in view of the total porosity results and surface microstructure changes) that different amounts of additive produced little variation and the generally inconsistent results. On investigation, the problem seemed to be the soft and flowing texture during the first 30 minutes of the disc manufacture stage which led to sample size variation and great variability in the data within some batches - see for example the information for a batch of 5 discs made consecutively with w/c=0.25 (Table 6.7).

Not only were the disc thicknesses more variable but also the diameter could be surprisingly, significantly wider than the die in which they were pressed. This was a factor of the plastic nature of the discs on removal from the die

when some flow occurred under their own weight. This was another indication that the w/c ratio was a more important variable in the presence of tetragonal zirconia nano particles than for OPC alone.

Table 6.7

A five sample batch of OPC + 5% ZrO₂ with w/c ratio of 0.25 after 21 days setting time

Sample	Diameter mm	Thickness mm	Load at Failure kN	Strength MN m ⁻²
A1B1	13.1	7.3	1.02	6.7
A1B2	15.2	7.2	1.12	6.4
A1B3	13.7	7.2	1.08	7.0
A1B4	13.1	5.3	0.46	4.2
A1B5	13.0	6.4	1.03	7.9

More tests were done with lower w/c ratios to obtain more stable discs in a physical sense and a ratio in the range 0.1–0.15 was found to be more satisfactory. Rather than repeat the work (with OPC alone at this ratio) it was felt that accepting the w/c ratio effect, a reduction factor of 0.66 could be applied to the composites for comparison purposes. When the data (for composites containing zirconia at different weight percentages and w/c of 0.15) became available it was much more revealing as to the beneficial effects of the zirconia. There was a significant improvement in strength which was non-linear and affects the extent of hydration - the increase matched the improved microstructure with a peak at 6% and an improved Weibull modulus. The strength data, adjusted for the lower w/c ratio is shown in Table 6.8 below. After making the adjustment for the lower w/c ratio the best composition (at 6% ZrO₂) is four times stronger than the OPC alone and even though the methods/samples are strictly not the same there is no doubt that the zirconia does provide a strengthening effect. The bell-shaped curve

(for strength v zirconia content) is a mirror image of the total porosity of the compositions, which suggests that this improvement is mainly a microstructural effect.

The zirconia improves the structure, binds hydrolysis products and decreases the porosity as already shown and this leads to the improved strength. Because of this effect it was possible to make a batch of samples containing 5 wt% ZrO₂ and to press them at the higher pressure of 39 MPa without significantly changing the w/c ratio. The effect of the increased load in disc preparation was to reduce water-porosity to 2% (from the 7% level shown in Table 6.3) for a 5 wt% ZrO₂ sample. The mean w/c-adjusted strength of these discs was 40 MPa, which is an increase of nearly 9 MPa for a pore reduction of 6%.

Table 6.8

The effect of different amounts of tetragonal zirconia on the strength of OPC discs at a w/c ratio of 0.15 at 28 days setting time.

Zirconia wt%	Tensile strength MN m ⁻²	Weibull modulus
0	7.8	6.8
0.5	22.6	9.5
1.0	22.8	9.4
2.0	24.6	9.1
4.0	29.6	8.9
5.0	31.2	9.0
6.0	34.2	11.0
8.0	32.0	6.9
10	30.4	8.7
12	28.6	8.8
15	26.2	9.0

(b) The effect on Young's modulus

The effect of the tetragonal zirconia (on the composite Young's modulus) was mostly determined by the Knoop microhardness method with a few confirmatory measurements made on specially prepared beams for the resonance frequency method. The combined data is presented in Table 6.9 and Figure 6.1. When the modulus is reduced to that expected for a w/c ratio of 0.23 there is a steady increase in the value for additions up to 6 wt% ZrO₂ and then a decline back to the OPC value by 15 wt%^{56, 60, 61, 62}. At about 5.5 wt% ZrO₂ the modulus is increased by approximately 40%; which is not as dramatic as the strength increase. Once again the property change with zirconia content is a mirror image of the effect that the zirconia has on the porosity.

Table 6.9

The effect of zirconia content on the Young's modulus of OPC for samples aged for 28 days and w/c = 0.15.

ZrO ₂ wt%	w/c	E measured GPa	E estimated for w/c = 0.23 GPa
0	0.23	22.6	22.6
0.5	0.15	23.0	15.2
1	0.15	34.9	23.0
2	0.15	37.8	25.0
4	0.15	44.2	29.2
5	0.15	50.1	33.1
6	0.15	46.1	27.7
8	0.15	40.6	26.8
10	0.15	36.6	24.2
12	0.15	33.5	22.1
15	0.15	32.7	21.6

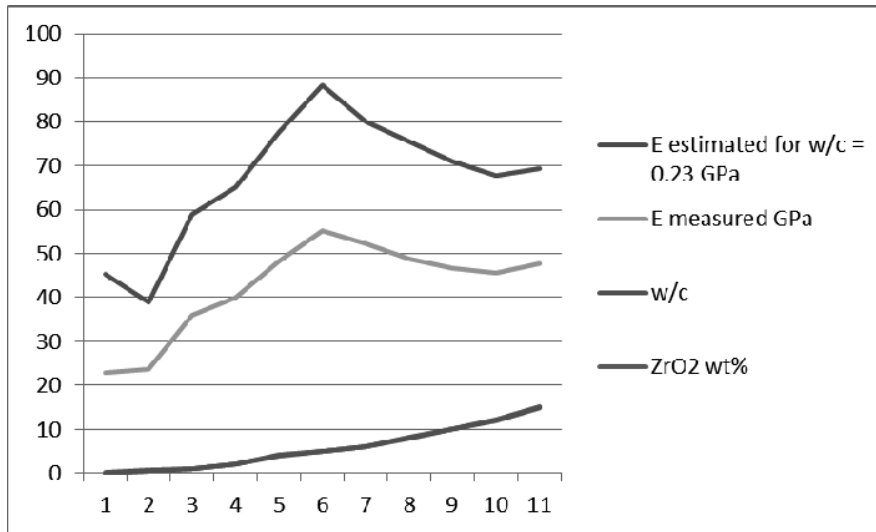


Figure 6.1. Correlation between measured and estimated E, w/c ratio and zirconia percent

6.2.3. The effect of zirconia on microhardness, low-load hardness and toughness

Knoop and Vickers microhardness were measured for the OPC-ZrO₂ composites containing different percentages of tetragonal ZrO₂ (Table 6.10). It is very clear that for w/c = 0.15 disks initially the microhardness increases with increasing zirconia content, reaching a maximum value of 1.27 GPa at 5 wt% ZrO₂ and then decreasing. For comparison purposes this corresponds to 0.84 GPa at the w/c ratio of 0.23. Data in chapter 5 for OPC at w/c=0.23 shows an average of 0.33 GPa for the cracked indents and 1.78 GPa when very low loads produce un-cracked indents.

Table 6.10.

Macrohardness and toughness of 5 and 10 wt% zirconia-OPC disks,
w/c=0.15, tested after 6-12 months hydration

Load N	491				981			
w/c	0.15		0.23		0.15		0.23	
ZrO ₂ wt%	H _v GNm ⁻²	K MNm ^{-3/2}	H _v GNm ⁻²	K MNm ^{-3/2}	H _v GNm ⁻²	K MNm ^{-3/2}	H _v GNm ⁻²	K MNm ^{-3/2}
5	1.2	0.84	0.79	0.55	0.95	0.84	0.63	0.55
	1.1	1.06	0.73	0.70		2.5		1.65
	1.2	0.20	0.79	0.13		0.65		0.43
		0.76		0.50		1.68		1.11
		1.06		0.70				
		0.76		0.50				
		1.74		1.15				
		0.78		0.51				
		1.27		0.83				
		0.88		0.58				
	Av	Av	Av	Av 0.62	Av	Av	Av	Av
	1.17	0.94	0.77		0.95	1.42	0.63	0.94
10	0.99	1.56	0.65	1.03				
	0.84	2.01	0.55	1.32				
		2.60		1.71				
	Av	Av	Av	Av				
	0.92	2.06	0.60	1.36				

The Knoop microhardness shows the trends more clearly reaching a maximum of 1.8 GPa at 5 wt% ZrO₂. This value corresponds to 1.22 GPa at a w/c of 0.23 which can be compared to the measured value of 0.8 GPa for w/c=0.23 OPC samples as given in Chapter 5.

The difference in the absolute values from both these methods is expected because of different depths of penetration, the different loads used to produce, whenever possible, cracked indents in the Vickers test and uncracked indents in the Knoop test, and the different area used to calculate the hardness values in the two methods.

Because of these factors the applied loads were 0.98-4.9N for the Knoop as opposed to 4.9–19.6N for the Vickers test. The reason for using two such different load ranges was that, in the case of the Vickers diamond, it was necessary to produce cracked indentations so that the fracture toughness could be measured, whilst un-cracked clear indents were needed with the Knoop diamond so that E could be calculated. Because large numbers of samples were tested, sufficient data was amassed to detect the influence of the zirconia content and Figure 6.2a shows the relationship between the zirconia content, microhardness and toughness values for the Vickers method for w/c=0.15 samples. Table 6.2 shows the setting times calculated from those samples that were cracked. As before (for comparison purposes) the data is adjusted for a higher w/c ratio of 0.23. In practice only about 6% of the indentations showed signs of cracking at 19.6N load.

SEM backscattering pictures were taken to examine both the distribution of the zirconia and the quality of the shape of the indent. However, this technique made it difficult to see, let alone measure the length of any cracks around the indentation. It is obvious that the indent on the lower zirconia percentage sample is smaller than the second one, and since they were made using the same load, means that the microhardness is larger.

The distribution of ZrO_2 is clear and the edges of the indents are very obvious. However, very fine cracks (that have popped-in at the corners of the indent) are extremely difficult to see. In contrast when ordinary conditions are used, corner cracks are clearly shown and can be measured.

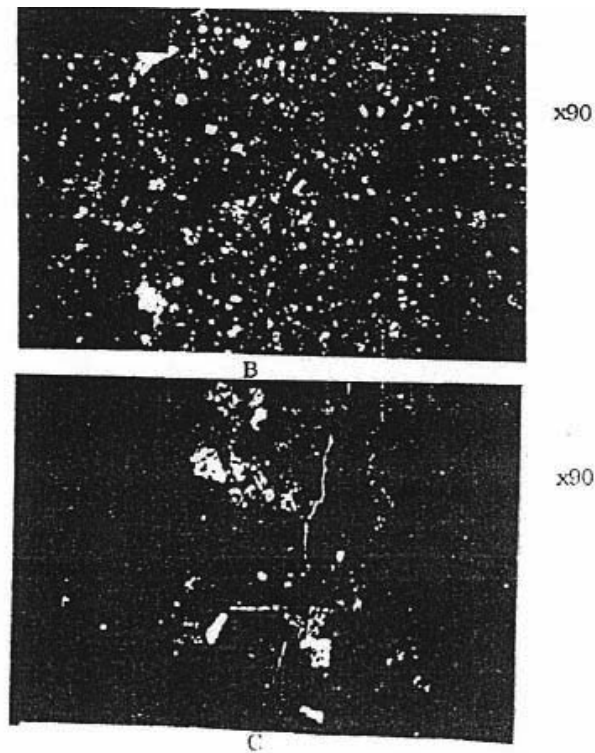


Figure 6.2: (a) BSE micrograph of OPC + 5 wt% tet.ZrO₂, (b) BSE micrograph of OPC + 10 wt% tet.ZrO₂, (c) SE micrograph of OPC + 10 wt% tet.ZrO₂.

The distribution of ZrO₂ is interesting as to the effect it appears to have on the appearance of the crack. The long crack running upwards bends away from the ZrO₂ agglomerate nearby; the two corners at which significantly larger amounts of ZrO₂ occur do not originate cracks but cracks begin from an edge a small distance from the ZrO₂-rich region. Two other clear pictures of cracks were observed deviating from ZrO₂ agglomerates and the crack running mostly through OPC hydrolysis product as opposed to un-hydrated grains.

6.2.4 Macrohardness and associated indentation crack study

Periodically, during the work, some samples were sent back for measurement and further investigation using equipment not available to the author the various places he worked. All the samples were polished until the traces of earlier indentations were removed. New indentations were first attempted at a load of 981N but it was soon obvious that this was too large because considerable damage was present around the indentations that suggested a too deep penetration. The load was reduced to 491N producing good indentations with variable amounts of cracking. The cracks were variable in appearance and caused a somewhat ad hoc analysis for toughness to be developed whereby measurements from each individual crack was used ,in equation 5.3, to obtain a series of values of toughness that were averaged for the sample.

Three or four indentations were made in the samples and micrographs taken for the analyses. Although each indent was separated as far as possible, sometimes cracks from different indents merged meaning that they had to be ignored while still using those that were not merged from the same indent in the toughness calculation. This was part of the ad hoc approach. Some of the samples were removed from the mounting resin, turned over, and remounted and polished then re-tested.

Cracks were often of variable length from opposite corners. Some cracks were of considerable length so a series of over-lapping micrographs were taken to study the progress of cracks through the microstructure. Examples

of this approach are discussed below and the numerical data is collected in Table 6.10.

It must be emphasised that the samples now to be discussed had a long hydration period, sometimes over a year, compared to the 3-week samples that were examined in the microhardness tester in the earlier work.

(a) Single Indent in sample A1M1 (5 wt% ZrO₂): load 491 N.

Different frames are discussed below but are not shown since data was lost over time.

Frame 1 shows cracks progressing through the microstructure. The one from the corner has a restricted length and width as it travels through a “good” region containing greater amounts of ZrO₂ and small, fairly isolated pores. It extends approximately 750µm to point D. using this length in the Evan’s equation gives a K₁ value of 0.84 MNm^{-3/2} which is about 4 times the average value for OPC alone and this indicates that this microstructure is tougher than any in OPC alone. The crack starting at point C on the indent edge has a shorter length of 598µm and it travels through the same type of microstructure ending at point E. In part the shorter length reflects the lower value of the propagating stress for an edge crack as opposed to a corner crack. In the ad hoc adopted way (using the same equation to get K₁) the value for this section of the sample is 1.06 MNm^{-3/2}.

From the opposite corner (to that so far discussed) at point B, the crack starts as a narrow one but through frames 3 and 4 gets wider and wider and continues across frame 5 to reach the edge of the sample and so this crack could not be used to measure K_1 . Nothing obvious explains this extended crack behaviour.

The fine crack pattern behaviour resumes from the indent corners at 90° to the system just discussed.

Frame 2 shows a clear indentation with sharp edges and fine cracks emerging from corners marked A and B. Also occurring in this system is a wider and more obvious crack emerging from the indent edge at the point marked C.

The indent diagonal length is $987.5\mu\text{m}$ giving a hardness value of 1.2GNm^{-2} , which is some 5 to 10 times harder than for OPC alone at this load when the sample was cracked and even harder than un-cracked OPC for 183 day hydrated samples that have a hardness of 1.09GNm^{-2} .

Frames 6, 7 and 8 show that there is less zirconia in these areas of the sample and the crack progresses until it emerges at the outside of the sample at F.

The minimum total length of $2717\mu\text{m}$ indicates a very low toughness that is less than $0.2\text{MNm}^{-3/2}$ and in the same value range for OPC alone.

From the opposite indent corner (to the one producing the exceptionally long crack) a much tougher behaviour is seen in Frames 9 and 10 where the crack has to pass through a “good” microstructure of well-distributed ZrO₂ and small, well-distributed pores. The crack ends at point G against a grain of ZrO₂. It has a length of 1196µm giving a K₁ value of 0.76 MNm^{-3/2}.

Analyses like these show that the results are quite variable and need careful consideration but, for a microstructure containing well-distributed pores and well-distributed ZrO₂, K₁ values in the range 0.76 to 1.06 MNm^{-3/2}, can be expected for a 5wt% Zirconia sample. Much lower values, reminiscent of OPC alone, are found for other parts of the microstructure.

(b) Three indents in a second sample of A1M1 (5 wt% ZrO₂): Load 491N. One sample of the same composition (5wt % ZrO₂) was examined and a series of micrographs showing 3 different indents made on the same sample were obtained from which some values of toughness could be measured.

Indent 1.

Frame 1 shows the corner of the indent lying in a “good” microstructure consisting of dark pores (about 55µm in diameter) with well-distributed ZrO₂ agglomerates with sizes up to 76µm. The indent corner has no cracks round it.

Frame 2 shows the vertically opposite corner lying in the same type of microstructure and again there is no sign of any cracks around the indent, which indicates a toughness value in excess of $1.06 \text{ MNm}^{-1.5}$.

Frame 5 shows almost the complete indent, confirming the good shape with sharp edges and reveals a crack coming from point A at the corner. The opposite corner has a crack that runs some $65\mu\text{m}$. The indent diagonal is $870\mu\text{m}$ in length which, from eqn. 5.3, indicates a hardness of 1.1 GNm^{-2} .

Frame 4 moving across into Frame 3 shows a narrow crack, starting at the indent corner with an approximate length of $1196\mu\text{m}$.

Frame 6 shows the crack from the opposite corner as it progresses across into Frame 7 with an approximate length almost the same as that on the opposite side. This gives a total crack length resulting in a toughness value of $0.76 \text{ MNm}^{-3/2}$.

Indent 2

Frame 4 shows a good clear indentation with a small crack from the corner that ends at a pore containing ZrO_2 . This shows the crack-stopping properties of these two features of the micro structure and, if this short crack-length, (of $174\mu\text{m}$) is used in the toughness equation a value of $1.74 \text{ MNm}^{-3/2}$ results. Another crack can be seen starting on the indent side at the point marked as A; it continues across from Frame 3 into Frame 2 where it is stopped in a ZrO_2 -richer region at point B. This crack has a length $1957\mu\text{m}$ giving an apparent toughness of $0.78 \text{ MNm}^{-3/2}$.

The indent diagonal in Frame 4 is 847.8 μm equating to a Vickers' hardness, H_v , of 1.2 GNm^{-2} , which is close to the value from the first indent.

Frame 5 shows a crack starting at the indent corner and going across into Frame 6 (where it continues at B and ends at point C) which is an isolated pore in a ZrO_2 -rich region. Again this powerful toughening combination is shown as a feature of the OPC-zirconia composites. An approximate length of the crack ending at C is 1359 μm . Hence the sides of the same penny-crack adds up to $(1957 + 1359 + 848) = 4164\mu\text{m}$ which is $2c'$ and half this can be used to get a mean toughness around this indent of 1.27 $\text{MNm}^{-3/2}$.

The other crack in **Frame 6** is coming from right to left from another unseen indent and ends at D, another isolated pore.

Frame 8 shows a vertical apex at 90° to the crack system just discussed. Good clean indent edges are obvious and a fine narrow crack is seen to run across Frame 8 into **Frame 7**, through a porous region of low ZrO_2 content and to the edge of the sample at E. Before leaving the sample, the crack length is 1408 μm . This figure can be used to set an upper value on toughness through this region of microstructure.

Frame 9 is the bottom vertical apex where a fine crack leaves the corner of the indent to terminate in a region of higher $\text{ZrO}_2\%$ and passes F. This crack has a length of 761 μm , which equates to a toughness of 0.88 $\text{MNm}^{-3/2}$ for this region.

(c) Double indents in A2M4 (10 wt% ZrO₂): Load 491 N

Two indents were made using a 50kg load. **Frames 3, 4, 5, 6 and 7** show the microstructure between the two indents and the cracks that are developed. This region is more difficult to interpret and more usable information is contained in **Frames 10, 11 and 12, 13, 14 and 15** where cracks from the two indents are running parallel in the vertical direction.

Frame 2 - the sharp-edged indent has no crack emerging from the sharp, well-defined corner but a crack starts from a sharp-angled grain of cement hydrate, A. The crack appears to be wide and runs through a series of pores and 'dark' material that is either cement hydrate or un-reacted cement powder to reach the outside in **Frame 1**. The region does not appear to be rich in ZrO₂. By the time the crack emerges it has an approximate length of 1110µm, but it is not possible to do much analytically with this system because the crack reaches the outside of the sample.

Frames 2 and 3 show the indent to have a diagonal of 955µm, which corresponds to a hardness value of 0.99 GN m⁻². This compares to a higher value of 1.2 GNm⁻² for 5wt% ZrO₂ sample A1M1. The decrease in hardness may reflect poorer hydration caused by the presence of extra ZrO₂.

Frame 3 - again no cracks emerge from the indent corner but once again from a sharply-angled hydrate crystal, B. This crack runs across Frames 3, 4, 5 and into 6 ending at C in Frame 6. In the process it appears to detour round a grain of ZrO₂ some 87µm in size, which is the very white angular

grain apparent in Frame 5. The length of this crack is approximately $3040\mu\text{m}$, which gives a toughness value of $1.56 \text{ MNm}^{-3/2}$ for this region.

Frame 7 shows the corner of the second indent from which a short crack proceeds to D, having travelled through a region of 'good' microstructure containing very obvious deposits of ZrO_2 . The relatively short length of $650\mu\text{m}$ results in a higher toughness for this region with a value of $2.01 \text{ MNm}^{-3/2}$.

Frame 8 picture contains almost the whole of the second indent from which the diagonal length is measured as $1100\mu\text{m}$. This length corresponds to a hardness of 0.84 GNm^{-2} .

A very thin, short crack emerges from the indent corner, terminating at E, in **Frame 9** the length of some $434\mu\text{m}$ corresponds to a toughness of $2.7 \text{ MNm}^{-3/2}$ confirming the general impression of increased toughness in this sample of increased zirconia content.

Frame 10 shows the top corner of the first indent which appears to be uncracked. The microstructure looks quite uniform with a cluster of ZrO_2 grains at F and the increased zirconia amounts appear to be locally increasing the toughness and preventing cracking.

Frames 12, 13 and 14 show the region above the vertical corner in indent 2 with no apparent crack generation. The horizontal corner appears in Frame

14 with a possible short crack emerging and ending at a ZrO₂ grain, G, of length 450µm. This gives a relatively high toughness value of 2.6 MNm^{-3/2}.

Frame 15 shows the region below the vertical corner of the second indent and appears to be crack free as the sample in this region is generally tougher.

This analysis shows a very variable situation with several tough zones whose average toughness is 2.06 MNm^{-3/2} with even tougher crack-free zones and easily broken regions.

Further pictorial evidence is limited because loads greater than 495N were needed to produce a significant number of cracked indentations and sudden fracture occurred breaking the sample into several pieces. Only a few examples of cracked indents in coherent samples could be obtained and these are discussed below. An example of the difficulty is that when crack-free indents were produced at a load of 981N, the next increment of 98N causes complete fracture.

(d) Another Sample of 5wt% ZrO₂ tested at 981N load

The series of micrographs show the same variable picture:

- (i) A clean edge to the indent with little evidence of fragmentation.
- (ii) A well-defined, sharp-pointed corner from which a crack emerges and travels through a series of 50-100µm-sized pores shown as (A).

- (iii) Another crack emerges from along the indent side at (B), where the indenter diamond encountered a pore approximately 380 μm long. This crack runs to connect a series of 76 μm pores until it stops on Frame 3 in an area containing two large zirconia aggregates approximately 90 μm in size that might be responsible for stopping the progress. The approximate length of this crack is 1300 μm , which equates to a toughness of 0.84 $\text{MNm}^{-3/2}$ but it must be remembered that the crack is not a corner crack and the analysis does not strictly apply.
- (iv) **Frame 2** contains an obvious crack that proceeds through pores and around dark OPC hydrate grains to reach the outside in **Frame 3**. This crack has an approximate length of 2720 μm which leads to a rough estimate (at this load) of 2.5 $\text{MNm}^{-3/2}$ for the toughness. There is evidence in these pictures that small grains of ZrO_2 have caused some large porosity around themselves as the un-hydrated OPC powder removes water from the zirconia and the grains shrink over the long setting times of these samples - see for example areas marked as (D) and (E). This has already been suggested as the reason for the maximum affect that zirconia has on the mechanical properties occurring between 5 and 7 wt% when all the low load results are considered in Fig 6.2 and Table 6.10.
- (v) The general impression is that more white ZrO_2 grains are near the outside of the sample, as **Frames 1 and 2** show.
- (vi). The opposite corner of the large indent diagonal is seen in **Frame 5** at F from where a crack is seen emerging from a pore near to the corner. This

crack runs through **Frame 6** and by **Frame 7** is narrowing quickly probably due to the fact that this area has a good distribution of ZrO₂ and it stops at G.

Frame 8 shows no sign of the crack and is clearly an area rich in ZrO₂ grains which suggests that, in the region covered by Frames 7 and 8, ZrO₂ transformations have compressed the crack and stopped its progress. The approximate total crack length on this side of the indent is 1520µm which, combined with an indent diagonal length of 1090µm, leads to an overall toughness of 0.65 MNm^{-3/2} for the material through which the crack has travelled.

Frame 9 shows no cracks which is in accord with the presence of large numbers of ZrO₂ grains that must be contributing to toughness in this area. This analysis is showing tough areas along with ordinary OPC areas making it difficult to obtain an overall sample toughness that might relate to ZrO₂ composition.

Frames 10 and 11 allow the diameter of the indent to be estimated as 1087µm, which equates to a hardness of 0.95 GNm⁻² and an estimated toughness on the side where the crack is contained in Frames 7 and 8, of 1.68 MN^{-3/2} using the Evan's formula.

Summary

It is not easy to be quantitative about this work (as the preceding discussion has shown) but, when the estimated numerical data is tabulated, the already

discerned trends (from the microhardness studies at 21 days of setting) are generally confirmed. The above data from the discussion of the macrohardness micrographs is collected in Table 6.10 and converted to a w/c ratio of 0.23 for comparison purposes.

In Table 6.10 the measured values were obtained at the w/c ratio of 0.15 for the reasons already explained and the w/c=0.23 values are estimated to allow comparisons with the OPC data without zirconia. The macrohardness values are, as expected, lower than the microhardness average values but are twice as large as the OPC with no zirconia discs even when left for the extra long time as can be seen by comparing the data in Table 6.11. The samples are also more than four times tougher than OPC alone.

Table 6.11

Improvement in mechanical property of versus OPC alone

Zirconia content wt%	Strength	E	H _v	K _c
	MPa	GPa	GPa	MPa m ^{1/2}
0	7.0	22.6	0.69	0.61
0.5	32.8	31.7	1.1	1.7
1	33.9	33.5	1.2	1.7
2	34	35.1	1.1	1.8
4	36.9	37.7	1.8	2.0
6	36.5	37.9	1.8	1.8
8	35.1	36.2	1.2	1.6
10	32.4	35.7	1.1	1.5

From all the detailed work presented so far it is clear that the incorporation of tetragonal zirconia powders in a brittle cement matrix clearly improves the fracture toughness parameter (Figure 6.3) as the tables and figures in this

chapter show.

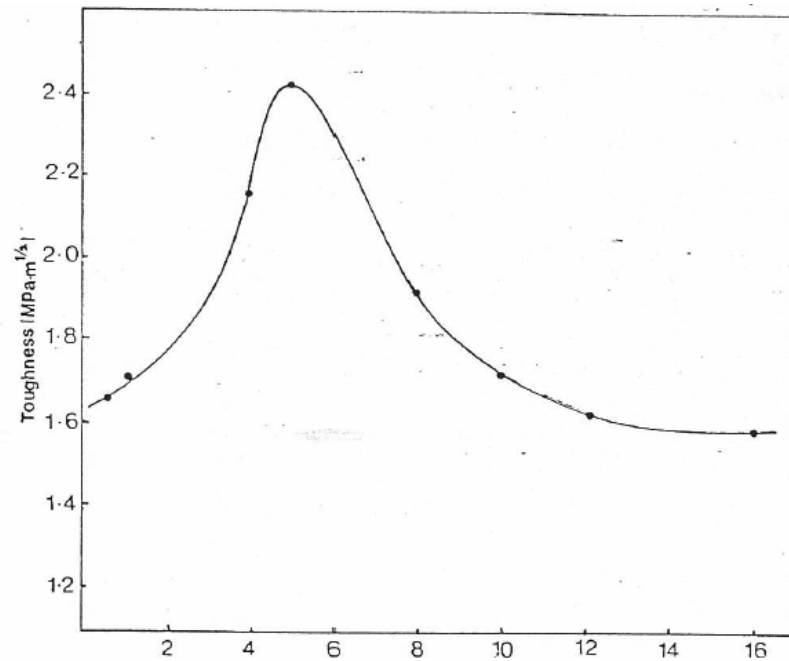
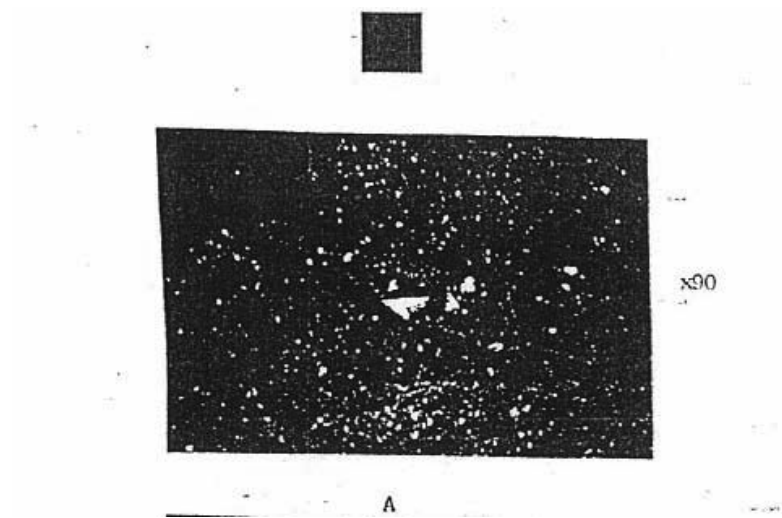


Figure 6.3 Plot showing fracture toughness versus [ZrO₂]

The best values of the K parameter represents a 4-fold improvement compared to OPC alone which is a strong indication that the high technology additive can operate as it does in more conventional ceramic systems. The

next set of experiments (somewhat limited in extent) were tried to see if the rather complicated step of thermal preparation of the tetragonal form of zirconia could be avoided while still retaining advantages. The idea was that over time the un-hydrated cement regions may extract moisture from a zirconia gel leaving behind volumes of nano-sized tetragonal Zirconia.

6.3 OPC-zirconia gel composites

Similar experiments to those done with the tetragonal zirconia additive were done, using different percentages of zirconia gel (amorphous hydrated ZrO_2) instead of tetragonal zirconia. In some cases the mixture was heated to $450^{\circ}C$ in order to produce tetragonal zirconia as the additive. An obvious effect of the heat treatment occurred in the initial setting-time experiment when a type of flash set occurred in this period. Only 1 minute elapsed for initial setting compared to 45 minutes for OPC- ZrO_2 dry mixed composites. A micrograph of a fracture surface of OPC + 10 wt% zirconia gel heated to $450^{\circ}C$ where it is very clear that many pores (in the range $0.1-0.4\mu m$ exist) and that a ZrO_2 has small particle size of $<10\mu m$ with no aggregates and is well-distributed. There is another micrograph of the gel-OPC composite after heat treatment and hydration. In this instance a good distribution of hydrate with angular un-hydrated OPC and ZrO_2 . An indent in this surface shows a well-formed diamond shape and there are corner cracks but also general fracture from the edges.

Table 6.12 shows an improvement in the mechanical properties compared to OPC alone but not as large an improvement when compared to the results in Table 6.12 for the OPC + tetragonal zirconia dry mixed samples.

Table 6.12

Mechanical properties of OPC-zirconia gel composites made by dry mixing and heating prior to hydration

Zirconia content wt%	Tensile strength MPa	E GPa	Vickers hardness GPa	Knoop hardness GPa	Toughness parameter MPa m ^{1/2}	Weibull modulus
0	7		0.69	-	0.61	6.8
0.5	34	22.6	1.17	1.39	1.65	9.5
1	34.9	34.9	1.18	1.46	1.71	9.4
2	37	37.8	1.20	1.63	1.88	9.1
4	41.3	44.2	1.24	1.78	2.16	8.9
5	46.9 59.2*	50.1	1.27	1.85	2.42	8.9
6	51.2	46.1	1.22	1.70	2.22	11
8	47.5	40.6	1.61	1.61	1.92	6.9
10	45.6	36	1.18	1.33	1.71	8.7
12	42.8	33.5	1.17	1.28	1.62	8.8
15	39.3	32.7	1.17	1.14	1.59	9.0

* This sample was pressed at 39 MPa

It was observed that the flash setting increased as a result of change in the content of zirconia from lower concentration to higher concentration. The improvement was not as obvious as that brought about by the tetragonal zirconia but was still good in comparison with the standard OPC discs alone. The improvements to the properties mirrors the first set of data by indicating a peak in the 4-6 wt% composites which is a little lower than the tetragonal ZrO₂ additive case.

It is likely that the heating stage, and its effect on hydration rate, was responsible for the poorer results and change in the position of maximum

effect even though the ZrO_2 was well distributed and non-aggregated. The flash setting observed would lead to some un-soundness in the discs.

6.4 Composite made by the vacuum infiltration method

This technique was chosen in order to give a good distribution of zirconia through the OPC discs by filling the connected porosity. Removal of large pores and inclusion of zirconia as a toughening agent were both potentially beneficial.

6.4.1 Dry OPC + ZrO_2 discs infiltrated by water

The object of the few experiments tried was to test the possibility of filling pores this way using the equipment available. Dry OPC- ZrO_2 mixtures were pressed at about 96 MPa to provide a friable disc. After each cycle (of evacuation and immersion in water) the change in mass was found which showed that, after four cycles, there was no further weight gain. The discs were immersed in water for 2 weeks. Typical weight gains by this process were equivalent to w/c ratios of only 0.06 which was well below the 0.1-0.27 range used for all earlier work. Two reasons were thought possible for this situation:

- (1)The porosity was too low, but attempts to make useable discs at lower dry pressing loads failed when they disintegrated in the water after evacuation.
- (2)The water was not “wetting” the material sufficiently.

The low w/c ratio was thought to lead to an increase in the strength and durability of the OPC discs. However prolonged immersion in water was

thought to increase the water content of the discs thus leading to a decrease in the strength over time. The micrograph in Figure 6.4 shows that the sample contains very small solid white areas that are zirconia and a coloured edge around the cement grains that corresponds to a hydration product. The distribution of the white-edged material was uneven as would be expected if only material around interconnected pores was hydrated.

Despite the poor overall hydration the strength (compared to normally produced OPC discs) was again improved and the average of 6 samples was 35.7MPa for the 5 wt% ZrO_2 and 37.1MPa for the 10% wt% ZrO_2 . These values are difficult to comment on given the small amount of work done by this method.

The last two small sections just add to the overall view that the summary at the end of section 6.2.3 is well founded and that the addition of zirconia in the 4–8 wt% range substantially improves the properties of OPC.

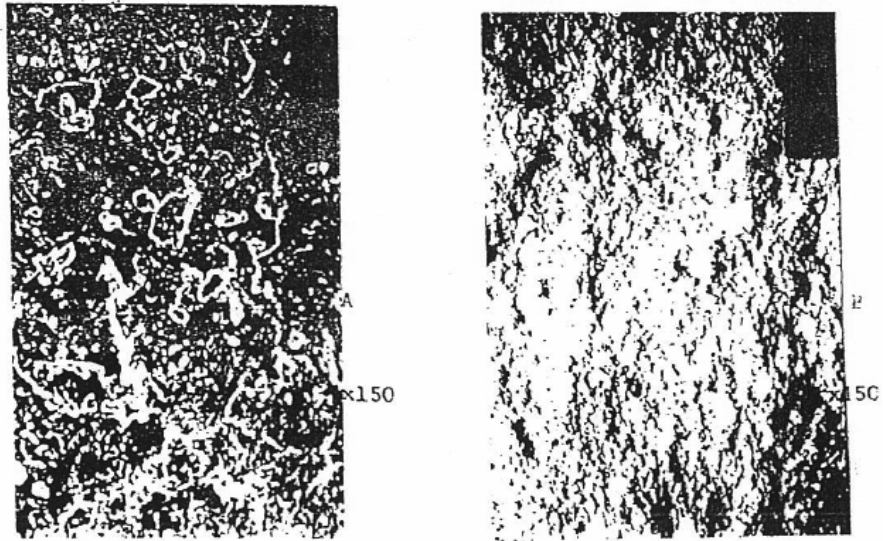


Figure 6.4: SEM micrographs of Dry OPC + 10% ZrO₂ vacuum-filled with H₂O

CHAPTER SEVEN

Conclusions and Future Work

7.1 General Discussion

This chapter summarises the aims of this research and brings together the milestones achieved. Firstly, major new work was produced relating to zirconia by concentrating efforts on thermal analysis and x-ray work to study the transformation from the amorphous preparation to crystalline phases. Secondly, significant improvements in the mechanical properties of hardened OPC paste were achieved by using zirconia developed in the first part of the practical work. Thirdly, a more concentrated effort in applying micro-hardness techniques to cement studies has resulted in more detailed modulus and toughness data that can be related to observed strengths.

Beginning with highlights from zirconia thermal analysis; there is general agreement between the data presented here and the work done by Crucean and Rand⁽¹²⁴⁾ who reported on the crystal structure of ZrO_2 following low temperature calcination of precipitates from $ZrOCl_2$ solutions made at different pH's. In both studies, as the pH at which the precipitate is made is raised, the amorphous-to-crystalline transition temperature is lowered. The decrease was some $25^\circ C$ (from $415^\circ C$ to $390^\circ C$) over the pH range 4–10 in Crucean work whilst here, as shown in Table 3.1, an $18^\circ C$ range (from $456^\circ C$ to $438^\circ C$) was found. The reason (for the difference of some $40^\circ C$ in the starting temperature of these ranges) does not lie in a crystallite size effect because crystallite diameters just after the exothermic peak temperatures in both studies are almost identical. Interestingly it lies in the different heating

rates used. This experimental observation became very important in this work when it was realised that it could be utilised to probe process-activation energies. This aspect will be reconsidered below.

Percentage mass losses were higher in this work (23-30%) compared to the 11–17% reported by Crucean with gels made from acid solutions. Crucean does not report a cubic zirconia phase in any preparation and agreement in this matter is not achieved until temperatures above 500°C are reached, as can be compared to data from Crucean's work in Table 7.1.

Table 7.1

Crucean and Rand's Data (117) for Gel Transformations

pH	Mass loss %		Phase Change Temperature °C (A → C T → M M → T)		
	At 1000 °C	At 120 °C			
4	6.7	17.4	415	940	1183
6	6.3	15.5	400	915	1172
8	4.4	13.5	395	913	1175
10	5.8	11.6	390	909	1179

Comparing the results in Table 4.1 to those in Table 7.1 shows where the results obtained in this work are significantly different. The crystallite sizes in both studies were in the range 9–13nm for material calcined at 400–500°C, with acid powders having the larger-sized crystallites in this range. Therefore the factor of crystallite size cannot be responsible for the disagreement. Some note must be taken of the significant differences in the total weight losses in the two studies. Here the higher losses must have resulted in much higher concentrations of water vapour around the powder during the transition. Water vapour is often a factor given for increasing surface

diffusion coefficients in oxide materials and so can enhance crystallite growth. It is also assumed to decrease surface energy values.

It appears from a comparison of this work with the data given in Crucean's paper that the tetragonal modification of ZrO_2 may be more stable in high partial pressures of water vapour. Crucean's observation was that from 400–600°C there was less tetragonal ZrO_2 than was found in this work where the higher percentage weight losses (as reported in Chapter 4) mean higher water vapour partial pressures in the atmosphere. Furthermore, in this research alkaline gels (which show only small weight losses during the crystallisation compared to acid gels) yield the cubic modification, further suggesting that tetragonal is the stable form in higher concentrations of water vapour, and that a metastable cubic form precedes the monoclinic form. Thus it appears (from these results) that the zirconia polymorph produced is influenced more by the water content of the gels and the effect this has on the transformation atmosphere than by the crystallite sizes. On the other hand, the temperature at which the exothermic crystallization process occurs is affected by crystallite size, and by the heating rate, as Figure 4.3 shows.

The very significant results obtained when alkaline gels were washed with dilute acids need to be noted here. With one exception, that of involving a sulphuric acid wash, the crystallisation temperatures were not affected but only tetragonal ZrO_2 crystallites were produced. The presence of H^+ ions from the acid washes at the gel surface combined with a surface nucleated crystallisation mechanism (which we have shown in the detailed analysis of

the DTA results to be the most probable mechanism) can account for the occurrence of the tetragonal modification. Thus low surface pH values control the crystal type and not necessarily the solution pH from which the gel was produced; although the former usually follows from the latter.

The enthalpy of transformation data for the oxychloride and nitrate derived ZrO_2 is quite revealing. First, the results lie in the range $20\text{--}34 \text{ kJ mol}^{-1}$ which is only about half the values reported for other hydroxide gels like Cr_2O_3 ⁽¹¹⁵⁾ and Fe_2O_3 ⁽¹⁷⁰⁾ which are usually in the range $64\text{--}75 \text{ kJmol}^{-1}$. Despite the smaller enthalpy the zirconia glow phenomenon has been frequently remarked upon, probably because it is a phenomenon that is so sharp, occurring over a few degrees of temperature range when compared to other such transitions that occur over hundreds of degrees. That is, once nucleated, it proceeds so rapidly to give a very sharp thermal spike, whereas other amorphous gel-to-crystalline transitions occur steadily over a large temperature interval. Results from this work (presented in Table 3.6) contain an enthalpy value for the $\text{Fe}(\text{OH})_3$ amorphous to Fe_2O_3 transition obtained here that put it at 63.5 kJ mol^{-1} which is in line with general gel-to-crystal transitions rather than the value in the early report⁽¹²²⁾. Certainly, if the Blesa model⁽¹²⁷⁾ for the crystallisation (outlined in Chapter 3.1) is accepted, then a coincident endothermic decomposition of the ionic tetramers at the point of crystallisation would decrease the exothermicity of the ZrO_2 transition relative to other gel systems.

The enthalpy data is re-expressed in order to highlight aspects of the process. Firstly, the $r^{1/2}$ versus ΔH relationship, where $r^{1/2}$ is the square root of the crystallite size; the graph is what might be expected if surface area was playing an important role in the crystallisation process. We have used crystallites sizes (as obtained in this study) but crystallite aggregation would override this because a particle size investigation using the laser scattering method did show that aggregates had diameters around 42–109 μm and so consisted of a large number of crystallites. Nevertheless the effect seems to be constant because a good linear relationship is shown.

Secondly, the graphical presentation clearly shows that the acid precipitates are smaller than alkali-derived solids from both oxychloride and nitrate solution precursors.

For a given precursor solution the enthalpy-crystallite size relationship may be a useful practical way to estimate zirconia particle sizes from the equations:

$$\text{acid pH nitrate gels } \Delta H = 156 - 31.8r \quad (7.1)$$

$$\text{alk pH nitrate gels } \Delta H = 153 - 30r^{1/2} \quad (7.2)$$

$$\text{alk pH oxychloride gels } \Delta H = 74 - 12.2r^{1/2} \quad (7.3)$$

From this research, however, it seems that the relationship between peak maximum position for the 0.167 $^{\circ}\text{K sec}^{-1}$ heating rate, which is experimentally easier to find, can be used to estimate crystallite sizes. The linear relationship for nitrate-derived powders, for example, gives:

$$T_{\text{max}} = 355 + 6.67r \quad (7.4)$$

Although, in general, crystallites in different size ranges are produced from oxychloride or nitrate precursor solutions, there was one pair of powders of comparable size, namely the pH 5.8 nitrate solution and the pH 3.7 oxychloride solution. The nitrate solution produced 13.4nm crystallites of tetragonal ZrO_2 with evolution of 30.9kJ mol^{-1} on crystallisation, whilst the pH 3.7 oxychloride solutions gave 13.0nm crystallites of tetragonal ZrO_2 and an enthalpy evolution of only 19.7kJ mol^{-1} on crystallisation.

This substantial difference in enthalpy correlates with the larger mass loss, due to greater decomposition on transition, from the oxychloride materials and may mean that the nitrate solution does not follow the tetrameric ion decomposition route.

A lower exothermic peak maximum (at 443°C for the nitrate material than the 456°C of the oxychloride derived powder in the case where the crystallite sizes were nearly the same) also suggests that less decomposition occurs resulting in a smoother nucleation process.

A colloidal sol of $ZrSiO_4$ coagulated with ammonia, filtered and dried produced a delay crystallisation of the ZrO_2 to 633°C when a rather small broad peak occurred; in this case cubic ZrO_2 resulted. X-ray methods were necessary to demonstrate that the results from these sols fitted into the established pattern from the oxychloride and nitrate solutions. Alkaline conditions gave cubic ZrO_2 and acid hydrolysis led to tetragonal ZrO_2 which

is as expected. The tetragonal acid-formed powder had a crystallite size in the usual range of 12.9nm and accordingly a DTA peak maximum temperature at 440⁰C which was not in contradiction with the data for nitrate-derived powder as shown in Figure 3.2. The totally unexpected result was the small crystallite size of 9.3nm for the alkaline-formed powder associated with the abnormally high transformation temperature of 633⁰C and the abnormally low enthalpy of crystallisation associated with such small crystallites.

A careful x-ray examination of samples (heated to different temperatures up to 1160 ⁰C combined with SEM-EDX analysis) revealed the presence of SiO₂ in these powders. Acid thermal hydrolysis of the ZrSiO₄ sol produced ZrO₂ powders whilst holding in solution most of the silica content. From this it was concluded that co-precipitated gel (as is the case when ammonia is added) produces a difficult-to-crystallise zirconia-gel leading to a cubic modification and finally, a tetragonal form of ZrO₂, of unusual thermal stability. These observations, above all others, suggested that dilution and surface chemistry of the ZrO₂ gel was of some importance. When the ΔH value is adjusted for the ZrO₂ + SiO₂ mixture that was present; a value of 30.5 kJ mol⁻¹ is in accord with all the data presented in Chapter 4. It is equal to the enthalpies obtained from nitrate precursor and almost double the values found for oxychloride precursor gel when comparable crystallite size powders are considered.

The delay in crystallisation (to 633⁰C in the presence of amorphous SiO₂ for such a small crystallite size as 9.3nm) was considered, in the light of all the work with pure zirconia gels, to be indicative of either a solid solution effect or some form of dilution effect. Both these possibilities were considered in subsequent work with Sn⁴⁺ and Fe³⁺ additions whilst making co-gels and by looking more closely at work on Al³⁺ additions presented by Inwang ⁽¹¹⁸⁾. For Al³⁺ additions Inwang noted that at pH 10.4 co-precipitated ZrO₂ always had the cubic form on crystallising and the manner in which the lattice volume decreases which is what would be expected if the smaller Al³⁺ ions were in solid solution.

However the continued large increase in crystallisation peak maximum temperature for samples containing more than 10-15 mol% Al₂O₃ cannot be explained on an increasing solid solution formation. Beyond 15 mol% Al₂O₃ the crystallisation maximum continues to be affected by a dilution phenomenon. Occluded cations and surface gel coatings on the ZrO₂ particles inhibit transformation once again in a way suggesting that the phenomenon is surface nucleated. A volume dilution factor on the delayed crystallisation is visibly indicated by the linear relationship between peak maximum temperature and cube root of the diluent atomic volume. As the Al₂O₃ concentration is increased the temperature to which the exothermic burst is delayed becomes similar to the 900⁰C peak attributed by Low ⁽¹⁷¹⁾ for zirconia crystallisation in gels obtained from solutions containing both Al³⁺ and Si⁴⁺ ions. Thus Low's conclusion about the source of the DTA peak in

his work is probably correct and lends support to the view that crystallisation and resultant crystal symmetry of ZrO_2 is a function of surface contaminants. Varying the pH of co-precipitation at any fixed percentage of diluent gel has only a small effect on the peak maximum crystallisation temperature and is in the range expected from the pure zirconia results. However, the zirconia symmetry is affected; for example in the presence of Al^{3+} the ZrO_2 immediately following crystallisation is cubic at all pH's ⁽¹¹⁸⁾ whereas dilution with SnO_2 , that is with Sn^{4+} ions, always leads to tetragonal ZrO_2 on crystallisation. This suggests that the presence of oxide vacancies that occur when Al^{3+} is substituted for Zr^{4+} may be dominant in determining the existence of the cubic modification.

There was never any x-ray evidence for preparation of ternary phases in the $Fe(OH)_3$, $Sn(OH)_4$ and $Al(OH)_3$ doped $Zr(OH)_4$ samples when heated to a maximum of $600^\circ C$ but above $1500^\circ C$, $ZrSiO_4$ resulted from ZrO_2 - SiO_2 gels. Some solid solution formation was obvious from x-ray parameter changes, and induced electrical conductivity in the Fe_2O_3 case in particular. Comparative cation sizes Zr^{4+} (0.08 nm), Al^{3+} (0.05nm), Fe^{3+} (0.064nm), Sn^{2+} (0.11 nm) and Sn^{4+} (0.071 nm) may explain the longer solid solution range with Sn^{4+} .

In the case of Fe^{3+} solid solubility is restricted (as the results in Table 4.6 shows) to around 5 mol % because above this γ - Fe_2O_3 is always observed

in X-ray films. A simple estimation procedure lends some support to this upper limit of Fe³⁺ substitution. Taking Zr⁴⁺ and Fe³⁺ as 0.08 and 0.064nm respectively then each ion has a respective volume, $(4/3\pi r^3)$, of 0.00214(nm)³ and 0.0011(nm)³. Thus if all Zr⁴⁺ was replaced by Fe³⁺ and, neglecting the effect oxygen vacancies would have, there would be a 50% cell volume decrease. For pure ZrO₂ the unit cell volume of the monoclinic form is 0.134 (nm)³. From Figure 4.7 the cell volume decrease levels out at 0.1305(nm)³ which is a 3.5(nm)³ decrease, which in turn is a 2.6% volume decrease, corresponding then to 5.2 %Fe in the cell at saturation, that is Zr_{1.95}Fe_{0.05}O_{1.997}.

A close examination (of Fig 4.7 for the Fe³⁺ case) suggests a change in mechanism might be occurring around 5–7 mol% where something of a plateau occurs. This is further evidence for the limited solubility. The 5–7% figure is further supported in Table 4.6 where the detection of γ -Fe₂O₃ was not definitely confirmed when the calcining temperature was kept down to 920⁰C until the 30 mol % sample and never definitely confirmed in specimens only heated to 900⁰C. Thus, those workers who never calcined above 920⁰C would not see any γ -Fe₂O₃ which probably accounts for the very large solid solubility of Fe³⁺ in ZrO₂ that they reported. In the way that ZrO₂ crystallisation is inhibited by co-gel precipitates, then Fe(OH)₃ will be affected in the same way, and so the re-crystallisation of Fe_{1-x}Zr_x(O)_y gel will be delayed to higher temperatures and the product will be amorphous as

far as x-ray's are concerned. Hence it seems unlikely that the large degree of solid solution reported by these earlier workers is correct.

Ferric hydroxide, $\text{Fe}(\text{OH})_3$, has by far the smallest solubility product in the systems studied with a value of 10^{-36} and so $\text{Fe}(\text{OH})_3$ precipitation would be immediate, followed by precipitation of $\text{Zr}(\text{OH})_4$ in localised 'acid' condition onto the $\text{Fe}(\text{OH})_3$. Thus the outer surface of the zirconia would be "pure".

On the ion size criterion Al^{3+} would form a solid solution with greater difficulty than Fe^{3+} and so the greater effect on the re-crystallisation of ZrO_2 probably arises from the slightly closer solubility product values of $\text{Zr}(\text{OH})_4$ (2.7×10^{-12}) and $\text{Al}(\text{OH})_3$ (1×10^{-15}) so that a more intimately mixed product arises at local precipitation sites producing $\text{Zr}(\text{OH})_4$ surfaces coated with $\text{Al}(\text{OH})_3$. Interestingly, gels from all ranges of pH produce cubic ZrO_2 after the re-crystallisation in the presence of Al_2O_3 but this was not the case for the $\text{Fe}(\text{OH})_3$ - $\text{Zr}(\text{OH})_4$ mixture where the tetragonal modification was evident from acidic conditions as expected from what occurs with pure ZrO_2 .

On the other hand, all products from Sn^{2+} containing solutions were tetragonal whatever the precipitation pH. Solubility figures for $\text{Sn}(\text{OH})_2$ suggest that this is less easily precipitated than $\text{Zr}(\text{OH})_4$ and here we may be seeing the effect of a tin hydroxide coating on $\text{Zr}(\text{OH})_4$ prior to decomposition and re-crystallisation. This latter combination appears to have the least effect on the re-crystallisation temperature of ZrO_2 as Fig 6.4 shows. Whilst Sn^{2+} is

as unlikely as Al^{3+} to lead to solid solution formation, oxidation on calcining to Sn^{4+} leads to ions close enough in size to form solid solutions without simultaneously requiring oxide vacancy creation.

The order of precipitation (as indicated by the solubility products in a co-gel) may be significant if we look at the mean crystallite size of the resultant zirconia. Crystallites from pure zirconium oxychloride solution are in the 10-15 nm range. Those formed in the presence of $\text{Fe}(\text{OH})_3$ are also in this range with values of 10–20nm as shown in Table 4.8. Ferric hydroxide ($\text{Fe}(\text{OH})_3$) is very insoluble and therefore instant precipitation leaves $\text{Zr}(\text{OH})_4$ to come down from a pure solution to give the similar crystallite sizes - some of the $\text{Zr}(\text{OH})_4$ will coat the $\text{Fe}(\text{OH})_3$. In the tin oxide and silica cases the solubilities are such that $\text{Zr}(\text{OH})_4$ comes out of solution first but is quickly followed by $\text{Sn}(\text{OH})_2$ which coats the $\text{Zr}(\text{OH})_4$ and leads to smaller crystallites in the 7-8 nm range as shown in Table 4.9. Crystallite sizes, reported by Inwang¹¹¹ were 9.5-10.5 nm suggesting that co-precipitation was a probability and this produces the largest delay in ZrO_2 re-crystallisation.

Much of the evidence so far reviewed points towards surface additives having a significant effect on the re-crystallisation temperature of ZrO_2 gel, possibly through interference with a surface nucleated process.

In the context of the later work (where tetragonal ZrO_2 was desirable after low temperature calcinations) doping with SnO_2 was a useful strategy

because the product ZrO_2 was more sensitive to stress transformation than tetragonal ZrO_2 stabilised more conventionally with oxides such as Y_2O_3 .

In the process of establishing this data a sensitivity of the re-crystallisation temperature to heating rate was discovered. Since this type of behaviour is associated with activated processes it was felt that activation energies might be found that could possibly throw more quantitative light on the mechanism of crystallisation. Experimentally this was achieved (as described in Chapter 4) by making plots of the linear heating rates used against the peak maximum temperature of the crystallisation process. It is clear (in Table 4.12) that there is a significant difference in the value of activation energy of crystallisation between the alkaline and acid-prepared powders. This is due to fact that different crystal symmetries are being nucleated; for the acid powder it was tetragonal ZrO_2 but cubic ZrO_2 from the alkaline-derived powder. The process is sharply divided in these results for example, ZrO_2 pH 9.3 powder had a value for activation energy from the Kissinger equation, assuming surface nucleation i.e. $n = 1$, $m = 1$, of $172.5 \text{ kJ mol}^{-1}$.

This was the same effectively of the value of $176.3 \text{ kJ mol}^{-1}$ for the neutral powder, pH 7.3. However, once acid conditions are achieved, the activation energy jumps to values around 215 kJ mol^{-1} . Significantly the acid-derived powders are associated with the measurable weight losses at the transformation compared to alkaline powders, as Table 4.2 shows. The fact that these have the highest activation energy values lead more strongly to the idea that dissociation is involved with nucleation, as the Blesa model

implies. No experiments in this series were undertaken that, in retrospect, might have shown differences associated with the presence of tetrameric ions, because all the data in Table 4.2 were obtained from nitrate-derived powders. The reason for this is that a decision to keep Cl^- ion out of the cement preparation had been taken and this focused the work somewhat. It would be worthwhile doing more experiments using oxychloride-derived powders at various pHs.

It has been shown that adding Sn^{2+} ions to the solutions and co-precipitating gives only tetragonal ZrO_2 . Thus the examination of the ZrO_2 - SnO_2 samples removes the cubic-to-tetragonal change. The sample containing least SnO_2 i.e. 3 mol%, has a significantly reduced activation energy value of $163.4 \text{ kJ mol}^{-1}$ and it can be seen that increasing the tin oxide content in the zirconia powder (from 3 to 10 mol%) increased the activation energy from 163.4 to $199.5 \text{ kJ mol}^{-1}$. Examination of the results in Table 3.10, offer one immediate explanation for this increase in activation energy because the ZrO_2 crystallites increase in size as the tin content increases. There is linear relationship between the activation energy and the tin oxide content. As the surface area (and therefore surface energy) increases, the activation energy decreases, which appears to implicate a surface mechanism becoming hindered as the tin concentration increases until a value similar to the acid pH powders is reached.

The systems containing the highly insoluble $\text{Fe}(\text{OH})_3$ give the most variable results. From solubility data the $\text{Fe}(\text{OH})_3$ gel is precipitated first on to which $\text{Zr}(\text{OH})_4$ is deposited and so the activation energy values for the ZrO_2 crystallisation might be expected to be like those from pure ZrO_2 samples. However, the pH effect is reversed; acid precipitated 7 mol % $\text{Fe}(\text{OH})_3$ which gave a tetragonal ZrO_2 had a lower activation energy than the cubic-forming alkaline powder. A significantly increased E value at 268 kJ mol^{-1} for the 4 mol% Fe^{3+} sample correlates with the suggested solid solubility effect. The colour changes and the electrical conductivity of the calcined solid strongly suggest that there is some solid solubility which implies induced higher concentrations of anion vacancies or incorporated H^+ ions, and this is another possible explanation for the results found here.

In this work the activation energies have been calculated using firstly, the earliest equation proposed by Kissinger⁽¹²¹⁾, which was evolved from a thermogravimetric and DTA analysis of the decomposition of CaCO_3 and $\text{Mg}(\text{OH})_2$. The isothermal thermogravimetric analysis allowed a reaction order of 0.69 to be measured and used in the calculation of activation energy. The analysis was extended to athermal systems so that a reaction order value could be estimated from a shape analysis of the athermal DTA curves.

The parameters a and b can be measured although, it must be emphasised, that most of the crystallisation peaks were so sharp in this work that it was

not realistic to do this. However, for a few samples, when the recorder chart speed could be adjusted to sample size and heating rate, satisfactory peaks for analysis were obtained. The results for these experiments are given in Table 7.2. The n values were found from eqn (7.5):

$$n = 1.26 S^{1/2} \quad (7.5)$$

Where $S=a/b$.

Table 7.2

Calculated critical flaw size present in OPC-ZrO₂ composites

Strength MPa	K _{1c} MPa m ^{1/2}	Flaw size* mm x 10 ⁻⁴
34.0	1.6	5.9
34.0	1.7	6.0
37.0	1.8	6.4
41.3	2.1	6.8
46.9	2.4	6.6
51.2	2.2	4.7
47.5	1.9	4.1
42.8	1.7	4.0
39.6	1.6	4.2
38.3	1.6	4.3

* Calculated using equation (7.6)

The values of n are all close to one and nearer to first order than any data given in Kissinger work. Values lower than one (i.e. around 0.6-0.7) were rationalised by Kissinger as re-adsorption effects as CO₂ gas was evolved from the decomposition and reacted with the product.

Some degree of asymmetry is detectable in our data, which appears to be pH related. The information in Table 7.2 justifies the use of n=1 (eqn. 4.9).

Hydroxide decomposition activation energies from the Kissinger work were about 132 kJ mol⁻¹; which compares to values obtained in isothermal experiments¹²⁸ of 114 kJ mol⁻¹. Thus reactions of the type solid → solid +

gas involving hydroxides have activation energies around 110–130 kJ mol⁻¹ which might be a diagnostic range since the Blesa model of the amorphous gel → crystalline transition involves such decompositions at the beginning of crystallisation.

All the data obtained in this study have activation energy values above this range. However, Murray and White⁽¹²⁹⁾ have reported that activation energies for the thermal decomposition of hydroxide-silicate clays appear to depend on the degree of crystalline order displayed by the sample, thus implying an interaction between crystallisation and decomposition reactions.

The most recent paper of some relevance to this work was the paper by Hayward *et al*⁽¹³⁰⁾ that dealt exclusively with re-crystallisation reactions in DTA experiment because glass-ceramic compositions were studied that concentrated on nucleation and crystallisation kinetics in both bulk and powdered glasses. Analysis of the theory has been given in Chapter 4 which shows that in order to decide on the most likely nucleation mechanism the linearity of various heating rate functions against $1/T_{\max}$ need to be considered. Such plots have been made for some of the tin and iron-doped powders. It is not realistic to conclude, from these plots alone, which combination of nucleation and crystal growth (as stated in Table 4.14) is the most satisfactory. Secondary evidence is forthcoming by considering the plots in Hayward's paper in more detail.

Although Hayward has drawn lines through all the data points, the results from powdered samples are best fitted to curves for both the Kissinger and modified Ozawa equations. In particular, the slow heating rate points are well off the lines drawn. Hayward attributes this to a surface phenomenon with an argument that says the high numbers of surface flaws inherent in powders act as nucleation sites and these nuclei grow at temperatures where the rate of crystallisation becomes significant.

However, at slow heating rates, the elapsed time to reach the crystallisation temperature is long and the surface flaws are thermally annealed during that time which then leads to a significant decrease in the number of nucleation sites at the crystallisation temperature. It is noteworthy that all the data gathered show the same effect at slow heating rates, and so Hayward's argument can be applied here. Furthermore, the best agreement between the two analyses used and the data presented is obtained for surface nucleated crystallisation. From the purely crystallisation work in Hayward's paper, activation energies from 460–490 kJ mol⁻¹ are found. Thus the data found here (and reported in Table 4.12) are in a reasonable range when considered in the light of the thermal decomposition and the crystallisation data of the paper quoted. On balance, considering the general agreement between Kissinger and Ozawa values when $n = 1$, $m = 1$, and the way that the activation energy values are raised when co-precipitates are present, particularly as deposits on the ZrO₂ surface, e.g. Fe(OH)₃-Zr(OH)₄ powders, then the mechanism of crystallisation is most likely one nucleated at the powder surface and involving some decomposition of residual OH groups.

This would allow acceptance of the Blesa complex ion structural unit in the gels and the inhibited crystallisation of ZrO_2 in the presence of diluent solid is also anticipated.

The second stated aim of this research is concerned with using the zirconia and tin-doped zirconia materials to change the properties of cement paste systems, and in particular improve their toughness. Since it is possible that flaws smaller than 100–150 μm (not associated with porosity) may be the strength-controlling feature in cement pastes, then it is only through improving K_{1c} that any significant increase in cement body strengths may be achieved as one would expect from equation 6.6:

$$\sigma = K_1 / 2a_c^{1/2} \quad (7.6)$$

Equation (7.6) is a hypothesis predicting a linear relationship between fracture stress and the reciprocal of the root of the length, a_c , the critical fracture inducing flaw.

The results presented in Chapter 6 showed that some success was achieved in improving K_{1c} values. However it is not easy to ascribe any progress with certainty when so many variables can have an effect. These have already been reviewed in Chapter two. For example, w/c ratio is clearly quite critical in influencing cement paste strengths; but in one of the ways chosen here to introduce the zirconia material, namely the vacuum infiltration route, this is not readily controllable. The best that can be achieved is to try and keep as many variables as possible constant, which was what this work attempted to

do and to attempt detailed analysis of crack patterns in samples presented to the SEM for examination.

Whichever method was used to introduce the zirconia produced one constant feature in that improvement to strength the toughness reached a maximum value at quite low zirconia additions. Young's modulus changes and, less obviously, microhardness values, also followed this behaviour.

A simple view of pore filling by the zirconia (taking the ZrO_2 as being both tougher and stronger than hydrated cement paste) does not fit easily with this observation. A more complex view must be taken which probably involves the effect that zirconia has on the hydration reactions. The results in Table 6.2 show that increasing the zirconia content has a marked effect on the initial setting time of the pastes. Furthermore, when dry tetragonal zirconia powder was mixed with dry OPC powder before adding the water to make the paste, there was evidence that porosity was associated with the nearby presence of the zirconia aggregates. On this basis the inclusion of ZrO_2 caused the larger sized porosity fraction to increase, and since porosity would have the opposite effect to the ZrO_2 itself on the mechanical properties, then a maximum improvement might be expected. A general decrease in the Weibull modulus values (listed in Table 6.8) can be taken to support this hypothesis; the 6 wt% ZrO_2 composite being an exception to the trend.

When the ZrO_2 was introduced via solution or suspension the results might be expected to be different because now the paste had already been hydrated and set in the absence of ZrO_2 . Such a difference in method can

involve a changed mechanism. The w/c ratio chosen for this work was 0.2 so that good pellet-pressing conditions can be attained and gives a more consistent microstructure. This relatively low ratio and some moisture squeezing out inevitably produces discs containing significant amounts of anhydrous cement grains embedded in C-S-H material. The presence of the water when the zirconia is infiltrated into the pores can alter the ratio of anhydrous cement to C-S-H and can even reverse their relative amounts, such that predictions from a new starting point must be made. Beaudion and Feldmann ⁽⁶⁶⁾ have given a more quantitative basis for a change in the situation such as the above by using a specific form of the law of mixtures to relate microhardness of a composite, H_c , to the volume fraction of a second phase:

$$H_c = H_1 [1 + \alpha V_2 / (1 + \gamma V_2)] \quad (7.7)$$

Where:

$$\alpha = \beta [(G_1 / G_2) - 1]$$

$$\gamma = (\alpha - E_2/E_1 + 1) / (E_2/E_1 - 1)$$

v_2 = volume fraction of the second phase

E = modulus of elasticity

G = shear modulus

β = Stress concentration factor related to the ratio of Young's modulus of the component and the shape of the second phase.

Since hardness can be related to strength and toughness this equation might describe the results found for the systems studied here. Significant change can occur if, at small w/c ratios, the main matrix phase is taken to be

anhydrous cement grains and the second phase is C-S-H plus ZrO_2 . Then in the presence of extra water, such as in infiltration addition of zirconia, the C-S-H phase becomes dominant and is the matrix with the unhydrated cement grains and ZrO_2 become the second phase. Clearly differences in shape alone, through β , can then produce significant changes in strength and fracture toughness. The results for infiltrated materials may not be directly comparable to the dry powder method of composite manufacture.

Values for strength and fracture toughness peaking at low additions of a second phase to OPC paste, in a way similar to the result reported here, can be found in the recent work of Coutts⁽¹⁷¹⁾. Coutts offers no explanation for the peak values but instead concentrates on the differences observed for soft-wood fibre additions as opposed to hard-wood fibres. The method involved the use of dried wood fibres which in the course of composite hydration could absorb H_2O , and so influence the setting and nearby porosity in the way that we have observed for dry ZrO_2 powders. Thus the peak values may be arising in the same way as explained here for the OPC- ZrO_2 composites.

The two detailed pieces of work (presented in 1975 and 1977 by Feldman and Beaudion already referred to above) make interesting and relevant parallels with what has been attempted here. In the first paper, these authors made composites of OPC and SiO_2 as dry mixes and then hydrated them at w/c ratio the range 0.26–0.45 before measuring compressive strengths, Young's modulus and microhardness. The second paper used an infiltration

technique to fill the available porosity with liquid sulphur before cooling to make a sulphur-OPC composite and then measuring the same properties.

Bell-shaped curves relating strength, hardness and Young's modulus to silica content were reported that peaked around 20–30% of added silica. X-ray diffraction results showed that most of the added silica had reacted with the OPC-hydrates during calcining of the mixture. Thus the ratios of crystalline and amorphous silicates in the matrix phases were changing throughout these experiments. This was not the case with the experiments done here and reported in this thesis since no calcining was involved.

Feldman and Beaudion ^(66, 160) showed that a family of lines existed when the log of the relevant mechanical property was plotted against porosity for varying silica contents. The inverse of the slope of these lines when plotted as function of silica content produced the bell-shaped curve. In this complex way these authors were studying the effect of silica content on the porosity of the materials. The complex behaviour was seen as the additive changing both the total and type of porosity, and in defining which components becomes the matrix phase, which is important when using equation 7.7.

It is not possible to use Feldman and Beaudion's graphical representation of the hardness data but using their equation:

$$H = H_0 \exp(-bp) \quad (7.8)$$

Where, H_0 is the hardness at zero porosity, b is a constant, and p is porosity. With $H_0 = 30270 \text{ kg cm}^{-2}$ and $b = 0.0667$ as given for a 5 mol% SiO_2 addition, and putting in the porosity of our sample at 10 wt%, a hardness value of 1.52 GPa is predicted which compares reasonably with one observed value of 1.22 GPa for non-autoclaved material containing ZrO_2 and not SiO_2 .

Chan *et al* ⁽¹³⁹⁾ have found that the maximum strength for cement compacts with $w/c = 0.075$ and pressed to 120 Mpa, such that the porosity was reduced to 0.15, was 27.9MPa compared to more normal values of 5.15MPa. Comparing this result to our results (especially for OPC- ZrO_2 composite pressed only to about 1/10 of the pressure used by Chan then the strength looks to be twice the values they reported. These improvements can be attributed to the presence of the tetragonal ZrO_2 which also clearly improves the K_{1C} value from 0.7 to 2.42 MPa $\text{m}^{1/2}$. Some microscopic evidence for ZrO_2 crack interaction has been presented in Figs 6.4 and 6.9, which might be responsible for this improvement.

The K_{1C} values have been measured in this work by the cracked micro-indentation technique on samples recovered from the Brazil strength test procedures. This required a significant effort to improve the technique and to apply this method to such composite materials as OPC paste. The effort is worthwhile because good micrographical evidence for differences between samples can be obtained.

Many values for any one disc can be obtained to achieve a good mean so that the variation shown in Table 6.5 is significant. In order to use eqn (5.23). Values for Young's modulus were needed and, as described, these were obtained by using another hardness technique that gave values (that we have shown by comparison with a standard procedure) are quite comparable. This again represents a useful contribution to practical work in this field of research. Joydeb *et al* ⁽¹⁷¹⁾ have used this method to find the Young's modulus of glass ceramics as the nitrogen content of the glass was increased. The two methods we used to find the Young's modulus show good agreement in values, but using the indentation method seems better than the resonance frequency method because of simpler preparation of the sample and, since many indents can be made on each sample, good statistics are possible. The highest value of Young's modulus of around 50 GPa is in reasonable agreement with the value of the MDF pastes given by Birchall *et al* ⁽⁷⁴⁾.

A fundamental assumption (in the Griffith equation for ceramic strength, equation 5.3) is that the flaws are atomically sharp i.e. the shape of the flaw is fixed. Some scientists have considered the pores themselves as an integral part of flaws i.e. the length of the flaw is considered to be the pore diameter plus one grain diameter on either side of the pore. This is based on the concept that cracks will propagate along grain boundaries until the next layer of grains is encountered.

Effect in variation of the pore shape that alters the stress field in the vicinity of the pore is not always considered. However Wittman and Zaitsev⁽⁷³⁾ have modelled the system as a paste containing a cylindrical hole with two edge cracks emanating from points of maximum tensile stress. Thus disagreement is common in deciding how large and what the critical flaws in cement pastes are.

Having been able to measure disc rupture strengths, K_{1C} and Young's modulus all independently, it is possible to assess the critical flaw in the various compositions examined here. In order to do this an appropriate flaw shape factor is introduced into eqn (7.6). For spherical flaws the factor is approximately 0.5 and then, using this, the critical flaw sizes were calculated. As can be seen the critical flaws are around 0.5 mm that is they are large macrosized pores because grain sizes of unhydrated material are much smaller. Examination of Fig 6.3, showing fracture toughness, shows that there are pores greater than 1mm present. The agreement, where it is shown, is reasonably good. Thus the decrease in the Weibull modulus is sensible and the hypothesis that dried tetragonal ZrO_2 powdered can introduce damaging large-sized pores might be reasonable.

The exceptionally high strengths found in the presence of such large critical flaws is unexpected and using the measured Young's modulus values leads to fracture surface energy around 40 Jm^{-2} which is twice the value reported by Birchall *et al*⁽⁷⁴⁾ for ordinary cement paste and 25% higher than the 30 Jm^{-2} reported for the MDF cement. These improvements lie in the fact that the

fracture toughness parameter for these materials has been substantially improved by the inclusion of metastable tetragonal zirconia.

7.2 Conclusions

By way of conclusion it is pertinent to return to each of the aims set out in Chapter one.

(1) The first aim of the work was to develop a method of producing metastable tetragonal powders to use in OPC-ZrO₂ composite disc manufacture. Clearly this has been achieved by using acid pH conditions to prepare a mixed ZrO₂-7 mol % SnO₂ gel which crystallised at 495⁰C to a tetragonal form of ZrO₂ with a mean crystallite size of 9.5nm. In the process of developing this powder the relative importance of crystallite size, solution pH, solid surface pH, and the presence of co-precipitates, on the crystal symmetry of ZrO₂, and on the crystallisation temperature of amorphous ZrO₂, has been established. By concentrating on the DTA peaks obtained at the amorphous to crystal transition, new data has been established, and results already in the literature have been rationalised.

(2) The second aim was to establish any effect that OPC phases may have on the in-situ preparation of tetragonal ZrO₂. This was only partially achieved and then in an indirect way. Efforts were concentrated on the effect that excess SnO₂ and Fe₂O₃ gave on the type and characteristics of ZrO₂ precipitation. An important volume dilution effect was found which changed dramatically the crystallisation temperature of amorphous ZrO₂ and in some cases the crystal symmetry after crystallisation. Thus higher temperature would be required to convert ZrO₂ to a crystalline form when diluted in the pores of an OPC body. New methods and data were applied here to strongly suggest that the transformation of ZrO₂ is a surface-controlled phenomenon.

(3) The third aim has been widely achieved in that much data has been gathered on the strength, Young's modulus, hardness and toughness of OPC and OPC-ZrO₂ composites. In general, greatly improved OPC material has been produced with strength values up to 51 MPa and K_{1C} to 2.42 MPa m^{1/2}. This aim was achieved by showing that less well-researched techniques can be successfully applied in this type of work. Small disc methods using the Brazil test were successful. A relatively new Young's modulus method, involving a Knoop indenter, has been successfully proven and the cracked indent toughness test has been extended to these materials.

A peak in the improvement of all mechanical properties was found for 5–6 wt % ZrO₂ - OPC samples and this has been related and rationalised in terms of a hydration change and pore generation phenomena. Nevertheless relatively high strength, relatively tough OPC bodies can be made successfully.

(4) The fourth aim has had considerable effort given to it, again with partial success. Alkaline sols of ZrO₂ powders can be infiltrated throughout the porosity, but mainly concentrated in the nearer surface layers. This leads to improved mechanical properties: strength=25.6 MPa and fracture toughness=1.83MPa m^{1/2}. Solution infiltration was partially successful but involved closer control of solution-OPC chemistry, and subsequent thermal treatment. When achieved this gives maximum strength improvement to 37.3MPa.

7.3 Suggestions for Future Work

A comprehensive analysis of the properties for OPC was done in the current study. However, additional studies are recommended for future work as below:

- a) All the evaluations conducted for the different types of zirconia in the current study could be extended to other modified Portland cement types such as Portland-Pozzolan cements, slag cements, super sulphated cements and ASTM types of cements (Type I to Type V).
- b) A comparative tiered analysis consisting of fineness (Blaine air permeability and Wagner turbidimeter tests), consistency, time of setting (initial and final), specific gravity, early stiffening (false and flash sets), loss of ignition, unsoundness (Autoclave expansion and Le Chatelier's tests), heat of hydration and chemical composition can be performed on the different types of OPCs in order to understand the physical and chemical properties that make them unique and suitable for different applications.
- c) A comparative testing can also be initiated for additional mortar testing such as mortar flow, air content of mortar and sulphate expansion.
- d) Additional testing from a hazard analysis standpoint can be initiated with respect to human exposure to dust as well as high temperatures, contact with allergenic materials, exposure to noise and burns from hot surface during manufacture of all Portland cement types.

All these analyses are expected to provide adequate information on the different Portland cement and are expected to complement the current in-depth study on the different properties of zirconias.

References

1. Love, M., New Cement Based Material for Engineering Construction Special Report, Ricadro Consulting Engineers, Shoreham, Sussex, U. 1987
2. Papo A, Piani L, and Ricceri R, "Optimization of Portland cement pastes," *Silicates Industrials*, **70**, no. 9-10, pp. 149–152, 2005.
3. David Hargreaves, the Global Cement Report – Sixth Edition, Tradeship Publications Limited, p.320, 2005.
4. Prinya Chindapasirt and Sumrerng Rukzon. Pore Structure Changes of Blended Cement Pastes Containing Fly Ash, Rice Husk Ash, and Palm Oil Fuel Ash Caused by Carbonation. *Journal of Materials in Civil Engineering*, 2009.
5. F.H. Hubbard, R.K. Dhir and M.S Ellis, Pulverized - Fuel for Concrete, *Cement and Concrete Research*, 15 (1), 185- 198, 1985.
6. I. J McColm, *Ceramic Science for Material Technology*, Leonard Hill, p 47, 1983.
7. I. Maki and S. Chromy. Microscopic Study on the Polymorphism of Ca_3SiO_5 , *Cement and Concrete Research*, 8 (4), 407- 410, 1978.
8. J.W. Jeffery. The Crystal Structure of Tricalcium Silicate. *Acta. Cryst.*, 5 (26), 26-35, 1952.
9. M. Hoke, Garrett *et al.* *Manufacture of Cement in Rotary Kilns*. Kaiser Industries Corp., Oakland, 1, 1977
10. R.H. Bouge and W. Lerch. Hydration of Portland Cement Compounds. *Ind. Eng. Chem.*, 26 (8), 837 - 847, 1934.

11. I. Maki and K. Kato. Phase Identification of Alite in Portland cement Clinker, *Cement and Concrete Research*, 12 (1), 93-160, 1982.
12. C. Remy, B. Reynard, M. Madon. Raman Spectroscopic Investigations of Dicalcium Silicate: Polymorphs and High-Temperature Phase Transformations, *Journal of the American Ceramic Society*, 80(2), 413-423, 1997
13. Hoke M. Garrett *et al*, *Manufacture of Cement in Rotary Kilns*, Kaiser Industries Corp., Oakland, 1, 1977.
14. J. Bensted, Y- Dicalcium Silicate and its Hydraulicity, *Cement and Concrete Research*, 8 (1), 73-76, 1978.
15. M. Regourd, In *Cement Production and Use*; ed. J. Skally, Engineering Foundation, N.Y., 41, 1979.
16. P. Mondal and J.W.Jeffery, The Crystal Structure of Tricalcium Aluminate, *Acta. Cryst. B31*, 689-697, 1975.
17. R.M.H. Banda and F.P. Glasser. Crystallization of the Molten Phase in Portland Cement Clinker, *Cement and Concrete Research*, 8 (5), 665-670, 1978.
18. G.Y. Shin and F.P.Glasser. Interdependence of Na and K Substitution in C3A, *Cement and Concrete Research*, **13** (1), 135-140, 1983.
19. Marco Pauri, Giorgio Ferrari and Mario Collepardi. Combined effect of lignosulfonate and carbonate on pure Portland clinker compounds hydration. IV. Hydration of tricalcium aluminate-sodium oxide solid solution, *Mag. Concrete Research*, **13** (1), 61-68, 1983.
20. A.J. Majumder. The Ferrite Phase in Cements, *Trans. of British Ceramic. Society*, **64**, 105-110, 1965.

21. A.A. Colville, The Crystal Structure of $\text{Ca}_2\text{Fe}_2\text{O}_5$ and its Relation to the Nuclear Electric Field Gradient at the Iron Site, *Acta. Cryst.*; **B26**, 1469-1473, 1970.
22. Akin Altun, Effect of CaF_2 and MgO on sintering of cement clinker, *Mag. Cement and Concrete Research*, **29**(11), 1847-1850, 1999
23. S.S. Rehsi, MgO in Portland Cement. In *Advacnce in Cement Technology* ed. by S.N.Ghosh. Pergammon, 467-481, 1981.
24. Nmai CK (chair) (2001) Cementitious materials for concrete, ACI Education Bulletin E3-01, ACI commite E-701
25. Struble, L., Livesey, P., Strother, P. del. Bye, G.C., 2011. *Portland Cement, 3rd edition: Composition, Production and Properties (Structures and Buildings)*, 3rd ed. ICE Publishing.
26. A.J. Mujumdar and S.S.Rehsi, The Mechanism of Stabilisation of High-Magnesia Portland Cements by Reactive Silica under Autoclave Condition, *Mag. of Concrete Research*, **21** (68), 141-150, 1969.
27. V.Kasselouris, C. Fikos and G.Parissakis, On Hydration up to 8 Years, *Cement and Concrete Research*, **15** (5), 758-764, 1985.
28. A.K. Chatterjee, Role of Volatiles in Cement Manufacture. In *Advances in Cement Technology* ed; by S.N.Ghosh, Pergamon Press, 203-263, 1983.
29. Hewlett, P., 2004. *Lea's Chemistry of Cement and Concrete*, Fourth Edition. Butterworth-Heinemann.
30. Potgieter, J., Horne, K., Potgieter, S., Wirth, W., 2002. An evaluation of the incorporation of a titanium dioxide producer's waste material in Portland cement clinker. *Materials Letters* 57, 157–163.

31. I.Jawed, J. Skalny and J.F. Young, Hydration of Portland Cement, In Structure and Performance of Cement, Ed by P.Barnes. Applied Science Publishers, 298-299, 1983.
32. J. Bensted, Hydration of Portland Cement. In Advances in Cement Technology ed. by S.N. Ghosh, Pergamon Press, 307-343,1981.
33. Hammlin M. Jennings, A model for the microstructure of calcium silicate hydrate in cement paste, Cement and Concrete Research, **30**(1), 101-116, 2000
34. Satish Chandra, Per Flodin. Interactions of polymers and organic admixtures on Portland cement hydration, Cement and Concrete Research, **17**(6), 875-890, 1987
35. J. Anderen, A.Kumar, D.M.Roy and D.Wolfe-Confer. The Effect of Calcium Sulphate Concentration on the Adsorption of a Superplasticizer on a Cement. Cement and Concrete Research, **16** (2), 255-259, 1986.
36. V.Lack. The Effect of Temperature on Cement Paste Hydration. Proc. Symp. Hydraulic Cement Paste. Their Structure and Properties, University of Sheffield, 82-84, 1976.
37. P. J Lesueur, D.D Double and G.W.Groves. Chemical and Morphological Studies of the Hydration of C3S. In Brit. Ceram. Proc. Ed. F.P. Glasser, No. 35, 177-193, 1984.
38. H.M. Jennings, B;J.Dalgleish and P.L.Pratt, Morphological Development of Hydrating C3S as Examined by Electron Microscopy Technique, J.Amer. Ceram. Soc., **64** (10), 567-572, 1981.

39. N.B. Singh and S.Prabha Singh. Lattice Defects and the Effect of Melment on the Hydration of Alite. *J. Mater. Sci.*, **22**, 2751-2758, 1987.
40. V. Lorprayoon and D.R. Rossington, Early Hydration of Cement Constituents with Organic Admixture, *Cement and Concrete Research*, **11** (2), 267-277.
41. F.M. Lea. *The Chemistry of Portland Cement and Concrete*, 2nd ed. Edward Arnold, London, p.180, 1970.
42. D, Menetrier, D.K. McNamara, I. Jawed and J, Skanly. Surface Morphology, *Cement and Concrete Research*, **10** (1), 107, 1980.
43. K. Fujii and W.Kondo. Rate and Mechanism of Hydration-dicalcium Silicate. *Journal of American Ceramic Society* **62** (3-4), 161-167, 1979.
44. F.M. Lea. *The Chemistry of Portland Cement and Concrete*, 2nd Ed. Edward Arnold, London, 177-349, 1970.
45. J. Goodbrake, J.F. Young and R.L.Bergerm. Reaction of Hydraulic Calcium Silicate with CO₂ and Water. *J. Amer.Ceram. Soc.*, **62**, 488,1979.
46. G.A. Spierings, and H.N. Stein. The Influence of Na₂O on the Hydration of C3A. *Cement and Concrete Research*, **6** (2), 265-272, 1976.
47. C.L.M. Holton and H.N. Stien, Influence of Quartz on the Reaction of C3A+ CaSO₄.2H₂O +water, *Cement and Concrete Research*, **7** (3), 291-296, 1977.
48. Ghosh, S.N. (Ed.), 2003. *Advances in Cement Technology: Chemistry, Manufacture and Testing*, 2nd Revised edition. ed. Taylor & Francis.

49. Deb, S.K., Manghnani, M.H., Ross, K., Livingston, R.A., Monteiro, P.J.M., 2003. Raman scattering and X-ray diffraction study of the thermal decomposition of an ettringite-group crystal. *Phys. Chem. Minerals* 30, 31–38.
50. I Jawad, J. Skalny and J.F.Young. Hydration of Portland Cement. In *Structure and Performance of Cement* ed. by P.Barnes, 237-317, 1983.
51. S.A. Mironov. In 6th Int Symp. on The Chemistry of Cement. Vol.II (1),182,1976.
52. H.F.W. Talyor. In 7th Int. Symp. on The Chemistry of Cement Vol.I, (II)-2/1, 1980.
53. V.Satave and O.Veprek, Thermal Decomposition of Ettringite under Hydrothermal Conditions. *J. Amer. Ceram. Soc.*, **58**, 357-359,1975.
54. D.D. Double, New Development in Understanding The Chemistry of Cement Hydration. *Phil. Trans. R. Soc. London*, **A 310**, 53-66, 1983.
55. J.D. Birchall and N.L. Thomas. The Mechanism of Retardation of Setting by Sugar. In *Brit. Ceram. Procs.* Ed. F.P. Glasser. **35**, (Sept.), 305-315, 1984.
56. S.Diamond and Carlos Gomez-Tolecle Consistency, Setting and Strength Gain Characteristics of a Low Porosity Cement. *Cement and Concrete Research*, **8**(5), 613-622, 1978.
57. N.B. Singh, S.Prabha Singh and A.K.Singh, Effect of Lactic Acid on Hydration of Portland Cement. *Cement and Concrete Research*,**16**, 545-553, 1986.

58. G.Idron. 5th Int. Symp.; on The Chemistry of Cement. Tokyo, Vol. **(III)**,411,1969.
59. S.Sprung. 7th International Symposium on the Chemistry of Cement, Paris, Vol. **I** ,21,1980.
60. F.P. Glasser, H. Bolio-Arceo, 2000. Zinc oxide in Portland cement. Part **II**: hydration, strength gain and hydrate mineralogy. Advances in Cement Research 12, 173–179.
61. J.Jambor. Influence of w/c Ratio on the Structure and Strength of hcp. Proc.Symp. Hydraulic Cement Paste: Their Structure and Properties, University of Sheffield, 175-188, 1976.
62. K.L.Watson. A Simple Relationship between the Compressive Strength and the Porosity of Hydrated Paste, Cement and Concrete Research, **11**(3), 473-476, 1981.
63. P.J. Sereda, R.F. Feldman and V.S.Ramachandran. 7th Int. Symp. on The Chemistry of Cement. Paris, **I-VI**, 1, 1980.
64. K. K. Schiller. In Mechanical Properties of Non-Metallic Materials. Ed. H. Walton, Butterworth, London, 34, 1958.
65. D.M. Roy and G.R.Gouda. Porosity- Strength Relation in Cementitious Materials with Very High Strengths. J. Amer. Ceram. Soc., **56** (10), 549-550, 1973.
66. R.F. Feldman and J.J.Beaudoin, Microstructure and Strength of Hydrated Cement, Cement and Concrete Research, **6** (3), 389-400, 1976.
67. A.Bajza. On the Factors Influencing the Strength of Cement Compacts, Cement and Concrete Research, **2**(1), 67-78,1972.

68. J.J. Beaudoin. Properties of Portland Cement. Cement and Concrete Research, **13**(1), 153-160, 1983.
69. C.S. Poon and G.W.Groves. The Effect of Latex on Macro-defCement, J.Mat.Sci., **22**, 2148-2152, 1987.
70. J.D. Birchall, A.J. Howard and K.Kendall. Strength-Porosity Relationship for Macrodefect Free cement. Nature, **289**, 388-390; **292**, 89-90, 1981a.
71. J.D.Birchall, A.J. Howard and K.Kendall. Strong Hydraulic Cement. Proc. Brit. Ceram. Soc., **32**, 25-32, 1982a..
72. S. Mindess. Relation between the Compressive Strength and Porosity of Autoclaved Calcium Silicate Hydrates A.J. Howard and K.Kendall, Strong Hydraulic Cement. Proc. Brit. Ceram. Soc., **32**, 25-32, 1982a.66. Y.Zaitsev. 7th Int. Symp. on The Chemistry of Cement. Paris, Vol. **(III)**, VI- 176, 1980.
73. Y.Zaitsev, The Seventh International Symposium on the Chemistry of Cement (ICCC), Paris, Vol. **(III)**, VI- 176, 1980.
74. J.B, Birchall, A.J. Howard, and K.Kendall, Cement in the Context of New Materials for an Energy- Expensive Future, Phil. Trans.R. Soc. Lond. **A310**, 31042, 1983.
75. K. Kendall, A.J. Howard and J.D.Birchall. The Relation between Porosity, Microstructure and Strength and the Approach to Advanced Cement -Based Materials. Phil. Trans. R. Soc. London. **A(310)**, 139-153, 1983.
76. A. A. Griffith. The Phenomenon of Rupture and Flow in Solids. Phil. Trans. R. Soc. London, **A (221)**, 163-198,1920.

77. R. A. Helmuth and D.A.Truk. Elastic Moduli of Hardened Portland Cement and C3S Paste, Symp. on Structure of Portland Cement Paste and Concrete, Highway Research Board (Washington D.C), Special Report **No.90**, 135, 1966.
78. H.Diab, L. Ben Dor and C. Heitner-Wirguin, The Porosity and Strength of Polymer-Cement. Cement and Concrete Research, **15(6)**, 1061-1067, 1985.
79. G.J. Verbeck and R.A Helmuth, Structure and Physical Properties of Cement Paste. Proc. 5th Int. Symp. on The Chemistry of Cement. Tokyo, **Part III**, p1-32, 1968.
80. P. Klieger, Effect of Mixing and Curing Temperature on Concrete Strength, J. Amer. Concrete Inst., **54**, 1063-1081, 1958.
81. C.J. Dodson and K.S. Rajagoplan. Field Test Verify Temperature Effects on Concrete Strength, Concrete Int, **1(12)**, 26-30, 1979.
82. Y.M. Butt, V.M. Kolbasov and V.V. Imashev. High Temperature Curing of Concrete Under Atmospheric Pressure. Proc. 5th Symp. on The Chemistry of Concrete, Tokyo, **III**, 437-476, 1968.
83. A.F. Abbasi and A.J. AL- Tayyib., Effect of Hot Weather on Modulus of Rupture and Splitting Tensile Strength of Concrete, Cement and Concrete, **15(2)**, 233-244, 1985.
84. W.M. Kriven. Possible Alternative Transformation Toughness of Zirconia: Crystallographic Aspects. J. Amer. Ceram. Soc., **17(12)**, 1021-1030, 1988.
85. J. Wang and R. Stevens. Toughening Mechanisms in Duplex Alumina-Zirconia Ceramics. J. Mater. Sci., **23**, 804-808, 1988.

86. G. Teufer. Crystal Structure of Tetragonal ZrO₂. Acta. Cryst., **15**(11), 1187-1188, 1962.
87. D.K. Smith and H.W. Newkirk, The Crystal Structure of Baddeleyite and its Relation to the Polymorphism of ZrO₂. Acta. Cryst., **118**(6), 983-991, 1965.
88. R.C. Garvie and P.S. Stabilized Zirconia in the system CaO-ZrO₂. J. Amer. Ceram. Soc., **55** (3), 152, 1972.
89. J.C Ray, R.K. Pati, P. Pramanik. 2000. Chemical synthesis and structural characterization of nanocrystalline powders of pure zirconia and yttria stabilized zirconia (YSZ). Journal of the European Ceramic Society 20, 1289–1295.
90. C. Minnis. 2001. Zirconia, 1st ed. Fence Books.
91. M. Trunec, Z. Chlup. 2009. Higher fracture toughness of tetragonal zirconia ceramics through nanocrystalline structure. Scripta Materialia **61**, 56–59
92. R.W. Davidge, Strength and Toughness in Ceramic Systems. Phil. Trans. R. Soc. London, **A (310)**, 113, 1983.
93. R.P. Ingel and D.Lewis III. Lattic Parameter and Density for Y₂O₃ Stabilized ZrO₂. J. Amer. Ceram. Soc., **69**(4), 325-33.
94. R.R. Hughan and K.H.J. Hannink, Precipitation During Controlled Cooling of Magnesia- Partially Stabilized ZrO₂. J. Amer. Ceram. Soc., **69**(7), 556, 1986.
95. R.L.K. Matsumot, Evaluation of K_{1C} Determination Methods as Applied to Ceria-Stabilized Tetragonal ZrO₂ Polycrystals. J. Amer. Ceram. Soc., **70**(17), 366, 1987.

96. G.K. Bunsal and A.H. Heuer. On the Martensitic Phase Transformation in ZrO_2 : Metallographic Evidence. *Acta. Met.* **20**(11), 1281, 1972.
97. R.C. Garvie. The Occurance of Metastable Tetragonal ZrO_2 as a Crystallite Size Effect. *J. Phys. Chem.*, **69**(4), 1238, 1965.
98. A.G. Evans, D.B.Marshall and N.H.Burlingame. Transformation Toughening in Ceramics. IV, Science and Technology in Zirconia. Ed. A.H. Heuer and L.W. Hobbs, 202, 1983.
99. N. Claussen. Fracture Toughness of Al_2O_3 with an Unstablized ZrO_2 Dispersed Phase. *J. Amer. Ceram. Soc.*, **59** (1), 49, 1976.
100. F.F. Lange. Transformation Toughening Parts (I-V). *J. Mater. Sci.*,**17**, 225, 1982.
101. R.C. Garvie. Microstructure and Performance of a Alumina Zirconia. Tool Bit. *J. Mater. Sci. Letts.* **3**, 315, 1984.
102. A.H. Heuer, N. Claussen, W.M. Kirven and M. Ruhle. Stability of Tetragonal Tool Bit. *J. Mater. Sci. Letts.* **3**, 315, 1984.
103. J.D. Eshelby. In *Progress in Solid Mechanics*, Vol.2, edited by I.N. Sneddon and R.Hill, Willey - Interscience, 89- 140, 1961.
104. H. Ruf and A.G. Evans, Toughening by Monolclinic ZrO_2 *J. Amer. Ceram. Soc.*, **60**, 328, 1983.
105. R.M. McMeeking and A.G. Evans. Mechanics of Transformation Toughening in Brittle Materials. *J. Amer. Ceram. Soc.* **65**, 242, 1982.
106. R.G. Garvie, R.H. Hannink and R.J. Pascoe. Ceramic Steel, *Nature*, **258**, 703-704, 1975.
107. N. Claussen, R.L.Cox and J.S. Wallace. Slow Growth of Microcracks: Evidence for one Type . *J. Amer. Ceram. Soc.* **65**, 242, 1982.

108. N. Claussen, Stress -Induced Transformation of Tetragonal ZrO₂ Particles in Ceramic Materials. *Acta. Met.*, **6**, 85, 1978.
109. R.W. Davidge and D.J.Green, Strength of Two-Phase Ceramic/ Glass Materials. *J. Mater. Sci.*, 3 (6), 629, 1968.
110. D.G. Green, Critical Microstructure for Microcracking in Al₂O₃-ZrO₂ Composite. *J. Amer. Ceram. Soc.*, **65**, 610, 1982.
111. B. Tirgenson and M.E Stranmains. *Colloid Chemistry*. MacMillan Corp. New York, 1962.
112. S.R. Witek and E.P.Butler, Zirconia Particle Coarsening and the Effect of Zirconia Additions on Mechanical Properties of Certain Commercial Aluminas. *Amer. Ceram. Soc.* **69**, 523, 1986.
113. T. Kosamic, R. Wagner and N.Claussen. X-ray Determination of Transformation Depths in Ceramics Containing Tetragonal ZrO₂. *J. Amer. Ceram. Soc.*, **64**, 72, 1981.
114. N. Claussen and J. Jahn. Mechanical Properties of Sintered and Hot-Pressed Si₃N₄-ZrO₂ Composites. *J.Amer.Ceram. Soc.*, 61 (1-2), 94-95, 1978.
115. E. Driupo. M.R. Ansean and R.J.Brook. Reaction Sintering : Correlation Between Densification and Reaction. *J. Mater. Sci.*, **14**, 2924, 1979.
116. N.Claussen and J. Janhm . Mechanical Properties of Sintered, In Situ - Reacted Mullite- Zirconia Composites. *J. Amer. Ceram. Soc.*, **63**, 228, 1980.
117. J.Glass and D.J.Green. Surface Modification of Ceramics by Partial Infiltration. *Advanced Ceramic Materials*, **2**(2), 129, 1987.

118. I.B. Inwang. Preparation, Characterisation and Mechanical Properties of Beta - Alumina- Zirconia Systems. Ph.D Thesis, Bradford University, U.K., 1988.
119. H.K. Schmid. Quantitative Analysis of Polymorphic Mixes of Zirconia by X-ray Diffraction. *J. Amer. Ceram. Soc.*, **367**, 2005.
120. H.P. Klug and L.E. Alexander. X-Ray Diffraction Procedure for Polycrystalline and Amorphous Materials. J. Willey and Sons Inc., New York, 1974.
121. W. Martienssen, H. Warlimont. Handbook of Condensed Matter and Materials. Springer, New York, 550, 2005.
122. M.Natavajana, G.V. Chandrasheker and C.N.R. Rao. Heats of Crystallisation of Some Amorphous Oxides. *J. Chem. Eng. Data*, **31(2)**, 235, 1968.
123. G.Gimblett, A.A. Rahaman and K.S.W. Sing. Thermal and Related Studies of Some Zirconia gels. *J. Chem. Biotechnology*, **30**, 51, 1980.
124. E. Crucean and B. Rand. Calcination of Zirconia Gel. *Trans. Brit. Ceram. Soc.*, **78**, 58,,1979.
125. Y . Murase and E.Kato. Role of Water Vapor in Crystallite Growth and the Tetragonal- Phase Transformation of ZrO_2 . *J. Amer. Ceram. Soc.*, **66**, 196, 1983.
126. J.E. Bailey, D.Lewis, Z.M.Librant and L.J.Parker. Phase Transformation in Milled Zirconia. *Trans. Brit. Ceram. Soc.*, **71**, 25-30, 1972.
127. M.A. Blesa, A.J.G. Maroto, S.I. Passagio, N.E.Figliolia and Rigotti. Hydrous Zirconium Dioxide: Interfacial Properties, the Formation of

- Monodisperse Spherical Particles and its Crystallisation at High Temperatures. *J.Mater.Sci.*, 20, 4601, 1985.
128. H.K. Kissinger. Reaction Kinetics in Differential Thermal Analysis. *Anal. Chem.*, **29** (11), 1702-1706, 1957.
 129. P.Murray and J.White. Kinetics of Thermal Dehydration of Glass, *Trans. British Ceramic Society*, **54**, 204-237, 1955.
 130. P.J.Hayward, E.R. Vance., and D.C.Doern. DTA/SEM Study of Crystallisation in Sphene Glass-Ceramics, *Am.Ceram.Soc.*, **66**(11), 1620-26, 1987.
 131. K. Matuskita and S.Sakka. Kinetic Study of Non-Isothermal Crystallisation of Glass by Thermal Analysis, *Bull.Inst.Chem. Res., Kyoto University* **59** (3), 159-171, 1981.
 132. T. Ozawa. A Modified Method for Kinetic Analysis of Thermoanalysis Data, *J. Thermal Anal.*, **9**(3), 369-373, 1976.
 133. F.M.Kplan. Crack Propagation and the Fracture of Concrete. *Journal Amer.Concr. Inst.*, 58, 591-610, 1961.
 134. R.L. Berger, F.V.Lawrence, Jr. and J.F. Young. Studies on the Hydration of C3S Pastes: Strength Development and Fracture Characteristics, *Cement and Concrete Research*, **3**(5), 497, 1973.
 135. S.P. Shah and S. Chandra. *J. Amer. Conc. Inst.*, **67**, 816, 1970.
 136. S. Midness. In *Fracture Mechanics of Concrete*. Ed. F.H. Wittmann, Elsevier, Amsterdam, 1-25, 1983.
 137. A.M. Neville. *Civ. Eng. (London)*, **54**, 1153-1156, 1308-1310, 1435-1439, 1959.

138. J. Glucklich. Fracture of Plain Concrete, J. Eng. Mech. Div. Am. Soc. Civ. Eng. **89**, 127, 1963.
139. N. McN. Alford, G.W. Groves and D.D. Double. Physical Properties of High Strength Cement Paste, Cement and Concrete Research, **12** (3), 349, 1982.
140. J.F. Knott. Fundamentals of Fracture Mechanics. Butterworths, London, 106, 1973.
141. P.E. Peterson. Fracture Energy of Concrete: Method of Determination, Cement and Concrete Research, **10**(1), 79, 1980.
142. B. Hillemier and H.K. Hilsdorf. Fracture Mechanics Studies on Concrete Compound. Cement and Concrete Research, **7**(5), 523, 1977.
143. J.H.Brown and C.D. Pomeroy. Fracture Toughness of Cement Paste and Mortar, Cement and Concrete Research, **3**(4), 975, 1973.
144. D.D. Higgins and J.E. Bailey. Fracture Measurements on Cement Paste. J. Mater. Sci., **11**, 1995, 1976.
145. H. Kitagawa, S. Kim and M. Suyama. Determination of Fracture Toughness of Cement Concrete Materials by Diametral Compression Test. Proc. 9th Congress on Material Research: Non-Metallic Materials. Japan, 160, 1976.
146. F. Moavenzadeh and R. Kuquel. J.Mater.Sci., 20, 4601, 1985.
147. D.J. Naus and J.L. Lott. Fracture Toughness of Portland Cement Concrete, J. Amer. Conc. Inst., **66**, 481, 1969.
148. J. S. Nadeau, S.Mindess and J.M. Hag, Slow Crack Growth in Cement Paste. J. Amer. Ceram. Soc., **57**(1), 51, 1974.

149. S. Mindess, F.V. Lawrence and C. Kesler. The J. Integral as a Fracture Criterion for Fibre Reinforced Concrete. Cement and Concrete Research, **7**(6), 731, 1977.
150. O.E. Gjrov, S.I. Sorenson and A. Arneson, Notch Sensitivity and Fracture Toughness of Concretes, Cement and Concrete Research, **7** (3), 333 - 344, 1977.
151. J.Tweed, S.C. Das and D.P.Rooke Int. J. Eng. Sci., **10**, 323, 1972.
152. M. Isida. Proc. US. Japan Seminar, 2, 8, 1974.
153. B. Lawn and R. Wilshaw. Indentation Fracture: Principles and Application. J. Mater. Sci., **10**, 1049, 1975.
154. A.G.Evans and E.A. Charles. Fracture Toughness Determination by Indentation. J. Amer. Ceram. Soc., **59**(7-8), 371, 1976.
155. B.R. Lawn, A.G. Evan and D.B.Marshall. Elastic/ Plastic Indentation Damage: Ceramic : the Median / Radial Crack System. J. Amer. Ceram. Soc., **63** (9-10), 574, 1980.
156. A.G.Evans. The Fracture Mechanics of Brittle Materials. ASTM STP 678. Ed. S.W. Freeman, 112-135, 1979.
157. G.R. Antis, P. Chantikulis, B.R. Lawn and D.B. Marshall. A Critical Evaluation of Indentation Techniques for Measuring Fracture Toughness. J. Amer. Ceram. Soc., **64** (9), 522, 1986.
158. K. Nirahara, R. Morena and D.P.H. Hasslema. Evaluation of K_{1c} of Brittle Solids by the Indentation Method with Low Crack to Crack Indent Ratios. J. Mater. Sci. Letts, **1**, 13, 1982.
159. B.G.Bhat, Comment on Elastic / Plastic Indentation. J. Amer. Ceram. Soc., **64**, 165, 1981.

160. J.J. Beaudion, Microhardness - Fracture Studies: High Alumina Cement System, *Cement and Concrete Research*, **12 (3)**, 289, 1982.
161. F.L.B. Carneio and A. Barcellos, Union of Testing and Research Laboratories for Materials and Structure, **9**, 372, 1973.
162. F.P.L. Oh, O Varder and I Finnie. Failure of Brittle Solids under Biaxial Stresses. *J. Int. Fracture*, **9**, 372, 1973.
163. G. Hondros. *Aust. J. App. Sci.*, **10**, 267, 1959.
164. O. Vardar and I. Finnie. An Analysis of the Brazilian Disc Fracture Test Using the Weibull Distribution Treatment of Brittle Strength. *Int. J. Fracture*. **11(3)**, 495 , 1975.
165. R.S. Mikhail, A.K. Mousa, S.A. Abo-El-Enein, M.S. Marie. Compressive strength versus residual porosity in polymer impregnated cement pastes, *Cement and Concrete Research*, **14(1)**, 25, 1984.
166. Leslie J. Struble, Paul E. Stutzman, Edwin R. Fuller Jr. Microstructural Aspects of the Fracture of Hardened Cement Paste. . *J. Amer. Ceram. Soc.*,**72(12)**, 2295, 1989.
167. V. S. Ramachandran, J. J. Beaudoin. *Handbook of Analytical Techniques in Concrete Science and Technology: Principles, Techniques, and Applications*. William Andrew, 2001.
168. R.W. Davidge. *Mechanical Behaviour of Ceramics*, Cambridge Solid State Science Series, Cambridge University Press, 134, 1980.
169. W. Weibull, A Statistical Distribution Function of Wide Applicability. *J. App. Mech.*, **18**, 293, 1951.

170. O.A. Kayyali. Strength and Porosity of Portland Cement Paste Subjected to Chloride Penetration. *J. Maters. in Civil Eng.*, **1**(1), 10 -18, 1989.
171. *Advances in Ceramics Characterization, Raw Materials, Processing, Properties, Degradation and Healing*, 2011, Ed. Sikalidis, C.
172. I. J. McColm, *Ceramic Hardness*, 1990. Springer, New York, 1990.
173. Nieh, T.G., Wadsworth, J., 1990. Superplastic. *Ceramics. Annual Review of Materials Science* **20**, 117–140.
174. Liang, Y.M., Zhao, J.H., 1999. Effect of zirconia particle size distribution on the toughness of zirconia-containing ceramics. *Journal of Materials Science* **34**, 2175–2181.
175. Daniels, T., 1970. A sensitive thermobalance for the study of polymer degradation. *European Polymer Journal* **6**, 773–784.
176. Bish, D.L., and J.E. Post (1989) *Modern Powder Diffraction*. *Reviews in Mineralogy* 20, 370 pp.
177. Johnston, N.W., Joesten, B.L., 1972. Kinetics of cyclization of vinyl chloride–methyl methacrylate copolymers. *Journal of Polymer Science Part A-1: Polymer Chemistry* **10**, 1271–1273.
178. Haach, V.G., Vasconcelos, G., Lourenço, P.B., 2011. Influence of aggregates grading and water/cement ratio in workability and hardened properties of mortars. *Construction and Building Materials* **25**, 2980–2987
179. Targan, Ş., Olgun, A., Erdogan, Y., Sevinc, V., 2002. Effects of supplementary cementing materials on the properties of cement and concrete. *Cement and Concrete Research* **32**, 1551–1558.

180. Mohamed. TAM., 2012. Composition and phase mineral variation of Portland cement in Mass Factory Sulaimani – Kurdistan Region NE-Iraq. International Journal of Basic & Applied Sciences IJBAS / IJENS, **12**, 109-118.
181. Afferrante, L., Ciavarella, M., Valenza, E., 2006. Is Weibull's modulus really a material constant? Example case with interacting collinear cracks. International Journal of Solids and Structures **43**, 5147–5157.
182. Yang, H., Xian, S., Liao, Y., Xue, Y., Chai, F., 2000. [Properties and infiltration arts of machinable infiltration ceramic(MIC)]. Hua Xi Kou Qiang Yi Xue Za Zhi **18**, 143–146.
183. Yoshitake, I., Rajabipour, F., Mimura, Y., and Scanlon, A. (2012) 'A Prediction Method of Tensile Young's Modulus of Concrete at Early Age'. Journal of Advances in Civil Engineering, Article ID 391214.
184. Song, H.-W., Cho, H.-J., Park, S.-S., Byun, K.-J., and Maekawa, K. "Early-Age, Cracking Resistance Evaluation of Concrete Structure," Concrete Science Engineering, Vol. 3, 2001, pp. 62~72.
185. A.B. Abell and D.A. Lange, "The Role of Crack Deflection in Toughening of Cement-Based Materials," International Symposium Proceedings, Brittle Matrix Composites 5, eds. A.M. Brandt, V.C. Li, L.H. Marshall, pp. 241-250
186. Rostami, V., 2012. Microstructure of cement paste subject to early carbonation curing. Cement and Concrete Research **42**, 186–193.
187. Juenger, M.C.G. and H.M. Jennings, "Effects of high alkalinity on cement pastes," ACI Materials Journal, **98 [3]**, 251-255, March 2001.

188. Stokes, A.R., 1948. A Numerical Fourier-analysis Method for the Correction of Widths and Shapes of Lines on X-ray Powder Photographs. Proc. Phys. Soc. 61, 382.
189. Van Tittelboom, K., De Belie, N., Van Loo, D., Jacobs, P., 2011. Self-healing efficiency of cementitious materials containing tubular capsules filled with healing agent. Cement and Concrete Composites 33, 497–505